UNIVERSITÀ DEGLI STUDI DI TRIESTE

XXXIII CICLO DEL DOTTORATO DI RICERCA IN FISICA

MULTIMODE HETERODYNE DETECTION FOR ULTRAFAST INVESTIGATION OF QUANTUM MATERIALS

Settore scientifico-disciplinare: FIS/03

DOTTORANDO:
FILIPPO GLEREAN

COORDINATORE:
PROF. FRANCESCO LONGO

SUPERVISORE DI TESI:
PROF. DANIELE FAUSTI

ANNO ACCADEMICO 2019/2020

Abstract

Ultrafast spectroscopy techniques, which employ ultrashort laser pulses, are a formidable tool to investigate the fundamental mechanisms in complex materials at their typical femtosecond timescale. Improving these methodologies is crucial to extract more information from the experiments and reveal new and deeper insights about the examined samples. In this doctoral thesis, we develop a novel experimental methodology to perform ultrafast optical pump&probe studies of samples out of equilibrium. We design and commission Time-resolved Multimode Heterodyne Detection and we employ it to investigate light-matter interactions in transparent quartz and complex materials such as the transition metal antiferromagnet TiOCl and the cuprate superconductor YBCO. We focus, in particular, in the study of coherent vibrational excitations.

The pump&probe approach consists in driving the sample under examination out of equilibrium with an intense pulse, the pump, and measure at a controlled delay the scattered light of a second pulse, the probe. The goal of the developed heterodyne technique is to maximize the amount of information which can be extracted from the experiment. Indeed, while the standard approach consists in measuring the average intensity of the probe pulse, the presented method allows for the full reconstruction of the quantum state of ultrashort pulses and in turn explores new multimode photon observables which are usually neglected in time-domain experiments. Precisely, thanks to heterodyne interferential amplification and single-pulse detection, we gain sensitivity to amplitude, phase and to the statistical distribution of the quadrature of each spectral component of the multimode probe field.

We report that we are able to discriminate the quantum limited multimode statistics of the probe pulse and disentangle the amplitude and phase responses in the ultrafast dynamics of the examined samples. We show that amplitude and phase dynamics are in general different and carry distinct information about the interaction processes.

Contents

Chapter 1

Introduction

In our daily life, we rely on our senses to have experience and understanding of the objects around us. While investigating materials we do more or less the same, even though we rely on sophisticated experimental techniques which enhance our senses. Following the analogy, spectroscopy is the science which uses the 'sight' in order to look into matter. Indeed, at the fundamental level they both consists in collecting and reading the information carried by the photons scattered by the light-matter interactions. Hence, the better we can read these photons, the deeper is the knowledge we get about the observed object.
In the Q4Q (*quantum spectroscopies for quantum materials*) laboratory, run by University of Trieste and Elettra Sincrotrone, we perform ultrafast spectroscopy experiments using ultrashort laser pulses, which allow us to look at materials with an extremely high temporal resolution on the femtosecond scale. We exploit this to study the vibrational and electronic dynamics in complex materials, as for instance transition metal oxides.
In this thesis, our goal is to further enhance the capabilities of ultrafast spectroscopy, revealing information about the samples which is hidden in the most intimate degrees of freedom of the photons employed.

Ultrafast spectroscopy

Ultrashort light pulses are electromagnetic pulses with a duration shorter than picoseconds, down to the attosecond regime, used to study ultrafast phenomena in atoms, molecules and solids [1]. The most common approach adopted in ultrafast experiments is the pump&probe one. It consists in using a first intense pump pulse to excite the system under analysis and trigger a non-equilibrium dynamics. The ultrafast response is then monitored measuring the light from a subsequent, not perturbative, probe pulse impinging the sample at a tunable delay with respect to the pump.
The pump&probe approach is widely and importantly applied in the context of quantum materials to reveal their governing mechanisms and potentialities [2]. These systems are ruled by a complex interplay between electronic, vibrational, spin and charge degrees of freedom. The analysis of the ultrafast dynamics is useful to study the interaction between the fundamental characters at play, disentangling their typical relaxation times. Moreover, the impulsive excitation is able to create photoinduced states and phases of the material away from the ones accessible in the thermodynamic limit, which can be used to achieve new functionalities.
From the technical point of view, standard optical pump&probe experiments rely on measuring the intensity of the probe pulse averaged over many repeated acquisitions. However, we highlight that this detection method is only partially sensitive to the information written in the collected probe photons. Therefore, in this thesis

we discuss how to improve the capability of measuring the probe. In detail, we aim to reconstruct its full multimode quantum state.

Exploring the full quantum state of light

The probe light is ultimately characterized by the dual wave-particle nature which is not completely revealed while measuring the mean intensity of the electromagnetic field. The probe pulse is a field with a peculiar phase structure, but at the same time it is an ensemble of quantized particles, the photons, which behave according to the quantum statistics. We are interested in revealing the information contained in these additional degrees of freedom in the ultrafast experiments. In particular, we plan to monitor the modulations due to the non-equilibrium dynamics of the perturbed material.
Interferometric techniques which mix the probe with a reference field are suitable to access the spectral phase degree of freedom and reconstruct the relative temporal dynamics [3, 4, 5]. Nevertheless, in order to get a description comprehensive of the statistical behavior we need to consider the more fundamental quantum formalism. In a quantum framework, the best knowledge of the system under consideration is represented by the quantum state. In the case of the optical probe, we can obtain the measurement of its state performing quantum state tomography [6]. The procedure is based on the heterodyne detection of the light state. It consists in mixing in an interferometer the, in general weak, probe field with an intense Local Oscillator which acts both as amplifier and phase reference. The heterodyne output is acquired pulse by pulse for a set of equally prepared repetitions. In this way, the statistical distribution is recorded. The measurement of the heterodyne trace statistics for the different interference phases forms an ensemble of observables, also defined *quorum*, which completely characterizes the quantum state.
In order to implement the time-resolved analysis of the full optical state in the ultrafast setting, we develop the pump&probe heterodyne detection scheme [7, 8, 9], which consists in performing the quantum state measurement of the femtosecond probe pulse as a function of the pump delay.
We complete the discussion highlighting that, due to their short temporal duration, the femtosecond pulses employed have a broad spectral bandwidth. Therefore, the optical state is a multimode system formed by the superposition of different frequency components [10]. Remarkably, every quantum mode can be considered as an individual quantum degree of freedom, which can carry specific information. The separated characterization of the modes can reveal peculiar attributes which vanish in the integrated analysis. Furthermore, the various components can be coupled to each other, for example as a consequence of non-linear interactions. In particular, it is possible to retrieve this link between modes at the statistical level studying their correlation.

In summary, we propose Time-resolved Multimode Heterodyne Detection [9] to explore the degrees of freedom accessible in the multimode quantum state of the ultrashort probe.
In this work, we employ this methodology to study the ultrafast response in crystalline solids. We set a peculiar focus in investigating coherent vibrational excitations, which we model and characterize in a benchmark material as quartz.
In the end, we challenge the capabilities of the technique in the analysis of complex

transition metal oxides.
The thesis is structured in the following way.

- In the first part of the dissertation, we introduce the multimode formalism suitable for ultrafast quantum optical state reconstruction and we report the experimental implementation. We analyze the probe pulse attributes, with peculiar focus on the characterization of the optical noise of the employed radiation.

- After the setup commissioning, the central part of the thesis is dedicated to the study of non-linear light-phonon interactions in transparent quartz. In detail, we investigate the coherent phonon response induced by Impulsive Stimulated Raman Scattering processes. Thanks to phase sensitivity, we show that in general the amplitude and phase non-equilibrium dynamics are different and representative of two distinct interactions. Indeed, the phase response is dependent on the modulation of the refractive properties mediated by the atomic position, while the amplitude response is relative to probe-sample energy exchanges mediated by the atomic momentum.

- The last part of the research extends the application of Time-resolved Multimode Heterodyne in the exploration of complex materials. At first, we examine the ultrafast orbital response in the quantum magnet TiOCl. We study the non-equilibrium dynamics dependent on selective resonant absorption of *d*-band orbital transitions. We observe qualitatively distinct responses for amplitude and phase and reveal orbital-phonon coupling features.
  In the end, we perform Time-resolved Heterodyne measurements in the high-temperature superconductor YBCO. We address the coherent phonon response and also in this case we obtain disentangled and sample specific amplitude and phase dynamics.

- In conclusion, we resume the main results obtained in this work with the proposed Time-resolved Multimode Heterodyne Detection. We highlight the information revealed in the novel degrees of freedom considered and discuss the further perspectives for the study of complex materials.

References

[1] M. Maiuri, M. Garavelli, and G. Cerullo. "Ultrafast Spectroscopy: State of the Art and Open Challenges". *Journal of the American Chemical Society* 142.1 (2020). PMID: 31800225.

[2] J. Orenstein. "Ultrafast spectroscopy of quantum materials". *Physics Today* 65 (2012).

[3] T. Fuji, T. Yoda, T. Hattori, and H. Nakatsuka. "Phase Sensitive Pump-Probe Spectroscopy Using a Michelson-Type Interferometer". *Japanese Journal of Applied Physics* 39.Part 1, No. 4A (2000).

[4] E. Tokunaga, A. Terasaki, and T. Kobayashi. "Femtosecond phase spectroscopy by use of frequency-domain interference". *J. Opt. Soc. Am. B* 12.5 (1995).

[5] E. Tokunaga, A. Terasaki, and T. Kobayashi. "Femtosecond continuum interferometer for transient phase and transmission spectroscopy". *J. Opt. Soc. Am. B* 13.3 (1996).

[6] A. I. Lvovsky and M. G. Raymer. "Continuous-variable optical quantum-state tomography". *Rev. Mod. Phys.* 81 (2009).

[7] M. Esposito. "A new spectroscopic approach to collective excitations in solids: pump-probe quantum state tomography". PhD thesis. University of Trieste, 2016.

[8] N. B. Grosse, N. Owschimikow, R. Aust, B. Lingnau, A. Koltchanov, M. Kolarczik, K. Lüdge, and U. Woggon. "Pump-probe quantum state tomography in a semiconductor optical amplifier". *Opt. Express* 22.26 (2014).

[9] F. Glerean, G. Jarc, A. Marciniak, F. Giusti, G. Sparapassi, A. Montanaro, E. M. Rigoni, J. O. Tollerud, and D. Fausti. "Time-resolved multimode heterodyne detection for dissecting coherent states of matter". *Opt. Lett.* 45.13 (2020).

[10] C. Fabre and N. Treps. "Modes and states in quantum optics". *Rev. Mod. Phys.* 92 (2020).

Part I

Time-resolved Multimode Heterodyne Detection

We present and characterize the Time-resolved Multimode Heterodyne Detection developed in this thesis work. The proposed technique aims to improve the information extracted from ultrafast optical pump&probe experiments.
This goal is pursued analyzing the probe light-pulse with methodologies proper of quantum optics. The probe radiation is indeed a quantum system described by photons and its full state can be reconstructed exploiting the optical state tomography. This approach allows us to access further degrees of freedom in addition to the probe intensity measured with standard detection. In particular, we are able to study the phase structure of the probe electric field and the photon statistical distribution.

We introduce in Chapter 2 the elements of quantum optics which are at the basis of the proposed scheme. We adopt the quantization of the electromagnetic field and report the state reconstruction method.
Chapter 3 describes the experimental implementation and in Chapter 4 we perform its characterization with the coherent states produced by the laser source.
In Chapter 5 we test the statistical sensitivity analyzing the non-gaussian distribution which arises from phase randomized superposition of coherent states.

Chapter 2

Measuring quantum states of light

The quantum mechanical description of light is the formal synthesis between the wave and particle nature of the electromagnetic radiation. The effects resulting from interference and photon discretization are both taken into account.
From the classical point of view, an optical mode is an electromagnetic plane wave which can be associated to an harmonic oscillator with a certain frequency ω. Its evolution is conveniently described as a function of its conjugated position q and momentum p in the phase-space, as illustrated in Fig. 2.1. The classical oscillator system is displayed as a point in the phase-space, which explores the different evolution phases ϕ along a circular trajectory centered around the origin (Fig. 2.1a), the radius of which indicates the oscillation amplitude. When generalizing this representation to the quantum setting (Fig. 2.1b) the conjugated variable of position and momentum are non-commuting operators. Therefore, the point-like model has to be replaced with an uncertainty region satisfying the Heisenberg indetermination principle ($\sigma_p \sigma_q \geq \hbar/2$).

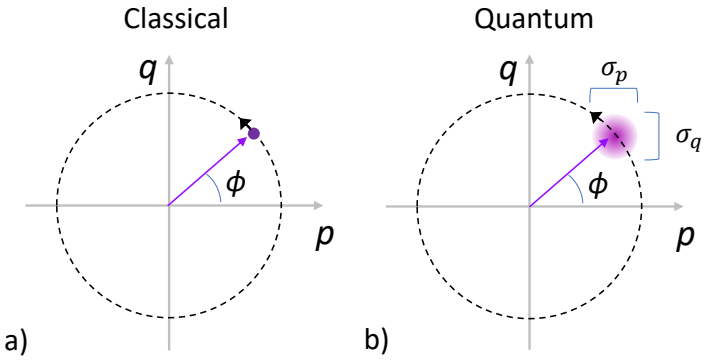

FIGURE 2.1: Phase-space evolution of the harmonic oscillator. a) Point-like classical state. b) Quantum state with intrinsic statistical uncertainty.

Indeed, quantum theory tells us that the knowledge achievable about a quantum system has at best a statistical character. While the outcome of a single measurement performed on the system cannot in general be determined, the statistical distribution of a set of equally prepared experiments can be defined.
The concept of measuring a quantum state should be distinguished from performing measurements on a quantum state. While the performance of a measurement is defined solely at a statistical level, we say we measure the quantum state when we have enough information to predict the statistical distribution of the measurements of the expectation value of any operator on this state [1, 2].
In detail, collecting the amount of information required to measure the state relies in measuring the statistical distribution of a minimal ensemble of observables, which is

defined *quorum*. The measurement of the quantum state consists then in measuring the statistics of the *quorum* observables and use them to calculate the state and the expectation value of any operator.

In this chapter, we report on the quantum state measurement method we adopt to characterize the probe light-pulses. In detail, we discuss Optical Tomography reconstruction [2, 3, 4, 5] of the Wigner function, which relies on the experimental implementation of a heterodyne[1] detection scheme.
We start by introducing the quantization of the electromagnetic field and we specify the quantum harmonic oscillator formalism in terms of field quadrature operators. We then focus on the quantum state, which we reference adopting the density matrix formalism. In particular, basing on the density approach, it is insightful to characterize the system defining the Wigner quasi-probability distribution. The Wigner function is defined in a phase-space which is built with respect to the field quadrature operators. Precisely, we show that the marginals of the Wigner function are equivalent to the statistical distributions of the quadrature operators. Hence, the quadratures obtained for the different phases of the evolution can be used to calculate the Wigner function and are therefore a suitable *quorum* to measure the full state. In order to experimentally record the field quadratures, we present the balanced heterodyne detection scheme. In the end, we extend the heterodyne state reconstruction to multimode light pulses.

2.1 Quantization of the electromagnetic field

In quantum mechanics observables are described in terms of hermitian operators. In the quantum theory of light, fundamental observables are the electric (**E**) and magnetic (**B**) field operators. Their expression for a monochromatic plane wave of frequency ω and polarization λ reads

$$\hat{E}_{\lambda,\omega}(\vec{x},t) = i\sqrt{\frac{\omega}{2V\epsilon_0}}\left(\vec{e}_\lambda \hat{a} e^{-i(\omega t-\vec{k}\cdot\vec{x})} - \vec{e}^*_\lambda \hat{a}^\dagger e^{i(\omega t-\vec{k}\cdot\vec{x})}\right), \tag{2.1}$$

$$\hat{B}_{\lambda,\omega}(\vec{x},t) = i\sqrt{\frac{1}{2V\omega\epsilon_0}}\vec{k}\times\left(\vec{e}_\lambda \hat{a} e^{-i(\omega t-\vec{k}\cdot\vec{x})} - \vec{e}^*_\lambda \hat{a}^\dagger e^{i(\omega t-\vec{k}\cdot\vec{x})}\right) \tag{2.2}$$

where $\vec{k}$ is the wavevector, $\vec{e}_\lambda$ the polarization vector and V the quantization volume. The operator character is defined by the photon ladder operators $\hat{a}$ and $\hat{a}^\dagger$, which follow the commutation relation $[\hat{a}\,,\,\hat{a}^\dagger] = 1$.
The energy stored in the electromagnetic field mode is calculated as

$$U = \frac{\epsilon_0}{2}\int_V d\vec{x}(|\mathbf{E}|^2 + |\mathbf{B}|^2) \tag{2.3}$$

which, translating it in the quantum formalism, corresponds to the hamiltonian of the optical system. If we insert the field operators in the previous this results

$$\hat{H} = \hbar\omega(\hat{a}^\dagger\hat{a} + \frac{1}{2}) \tag{2.4}$$

[1] In the literature, quantum state tomography is usually discussed in terms of *homodyne* detection. Hereby we adopt the more general *heterodyne* definition. We discuss the details in sec. 2.4.

which is indeed the hamiltonian of a quantum harmonic oscillator. In this setting, it is insightful to define the conjugate variables

$$\hat{X} = \frac{\hat{a} + \hat{a}^\dagger}{\sqrt{2}} \quad \text{and} \quad \hat{Y} = \frac{\hat{a} - \hat{a}^\dagger}{\sqrt{2}i} \tag{2.5}$$

also called quadrature fields, which represent the optical analogous of position and momentum of the harmonic oscillator. It will also be convenient to explore the full phase-space defining the generalized quadrature

$$\hat{X}_\phi = \frac{1}{\sqrt{2}}(\hat{a}e^{-i\phi} + \hat{a}^\dagger e^{i\phi}). \tag{2.6}$$

In this section, we presented the operators relevant in the discussion. In the following, we focus on the state on which these operators act.

2.2 The quantum state

The quantum state of a system is the object which includes the knowledge regarding the statistical expectation of a general observable.
In case an experiment exists, at least in principle, whose outcome is unique and predictable with certainty when performed on a system prepared in a specific state, such state is defined a *pure state* [1].
Pure states are the fundamental elements of the general quantum state description. They are formally represented as normalized vectors $|\Psi\rangle$ in the Hilbert space of the system. The general expectation value of an observable $\hat{O}$ can be calculated on a pure state as

$$\langle \hat{O} \rangle = \langle \Psi | \hat{O} | \Psi \rangle = \mathrm{Tr}[\hat{O} | \Psi \rangle \langle \Psi |], \tag{2.7}$$

where the formulation in terms of the trace operator suggests that the state can be identified by the projector $|\Psi\rangle \langle \Psi|$.
However, systems occur for which no experiment gives a unique outcome predictable with certainty and the pure state formalism is not sufficient. The more general description accounts for the statistical mixtures of different states, which can not be associated to a single vector in the Hilbert space. In order to characterize them, we introduce the *density matrix*. It is an hermitian, non-negative operator of unit trace

$$\hat{\rho} = \sum_n c_n |\Psi_n\rangle \langle \Psi_n| \tag{2.8}$$

which accounts for the statistical superposition of different pure states $|\Psi_n\rangle$.
The sub-states are normalized $\langle \Psi_n | \Psi_n \rangle = 1$ and the coefficients c_n are such that

$$\sum_n c_n = 1, \quad c_n > 0. \tag{2.9}$$

If we have that only one c_n is different from zero and equal to one we retrieve the case in which the system is in a pure state, otherwise the state is *mixed*. We also note that the same density matrix can have different representations and the choice of the set $|\Psi_n\rangle$ is not unique.
Remarkably, with the general density formalism the expectation value of an observable reads

$$\langle \hat{O} \rangle = \sum_n c_n \langle \Psi_n | \hat{O} | \Psi_n \rangle = \mathrm{Tr}[\hat{\rho}\hat{O}] \tag{2.10}$$

which states that the knowledge about the quantum state is conveniently included in the density operator.

2.2.1 The Wigner function

Considering the analogy with the quantum harmonic oscillator found in eq. (2.4), a phase-space representation is useful to describe the electromagnetic radiation. The quantum state has an insightful phase-space representation by means of the Wigner-Weyl transform of the density operator

$$W_\rho(q,p) = \frac{1}{2\pi\hbar}\int_{\mathbb{R}} dy \, \langle q + \frac{y}{2}| \, \hat{\rho} \, |q - \frac{y}{2}\rangle \, e^{-iyp/\hbar}, \tag{2.11}$$

which is dubbed the Wigner function and is dependent on the conjugate phase-space variables p and q.
The expectation values of the system observables are calculated as

$$\langle \hat{O} \rangle = 2\pi\hbar \int_{\mathbb{R}^2} dqdp W_\rho(q,p) W_O(q,p), \tag{2.12}$$

where W_O is the Wigner transform of the operator $\hat{O}$, which describes the operator values as a function of the phase-space variables. From the latter expression, we note that the Wigner function weights the possible outcomes of the observable while calculating the average over the phase-space. However, the Wigner function is not a proper probability distribution because it is not positive definite. As a consequence of this, it is considered a quasi-probability distribution.
The presence of negative values assumed by regions in the Wigner is a result which cannot be obtained in a classical setting and thus an indication of a purely quantum mechanical state. Nevertheless, even when dealing with negativities the statistical predictions are well-defined. In detail, the marginal distributions of the Wigner function are positive defined. Calculating the marginals we can for example obtain the statistical distribution of the q and p probability distributions as

$$\begin{aligned} w(q) &= \langle q| \, \hat{\rho} \, |q\rangle = \int_{\mathbb{R}} dp W_\rho(q,p), \\ w(p) &= \langle p| \, \hat{\rho} \, |p\rangle = \int_{\mathbb{R}} dq W_\rho(q,p). \end{aligned} \tag{2.13}$$

Moreover, the marginal distribution can be defined along an arbitrary orientation of the phase space as

$$w(q,\phi) = \langle q_\phi| \, \hat{\rho} \, |q_\phi\rangle = \int_{\mathbb{R}} dp W_\rho(q\cos\phi - p\sin\phi, q\sin\phi + p\cos\phi). \tag{2.14}$$

We will see in a while that the previously defined marginals are fundamental objects in order to perform the state reconstruction, but before moving to the measurement method, we introduce some of the typical states which are proper of quantum optical systems.

Coherent states

The formal quantum description of classical electromagnetic waves, as for instance the radiation produced by a laser source, is expressed by coherent states. The

classical point in the phase-space is generalized in the quantum setting with a gaussian distribution satisfying the minimal uncertainty provided by the Heisenberg indetermination principle.

$$\sigma_q^2 \sigma_p^2 \geq \frac{1}{4} \tag{2.15}$$

The vacuum state is the particular case in which the distribution has null expectation value and is centered around the origin (Fig. 2.2a). The optical wave oscillating

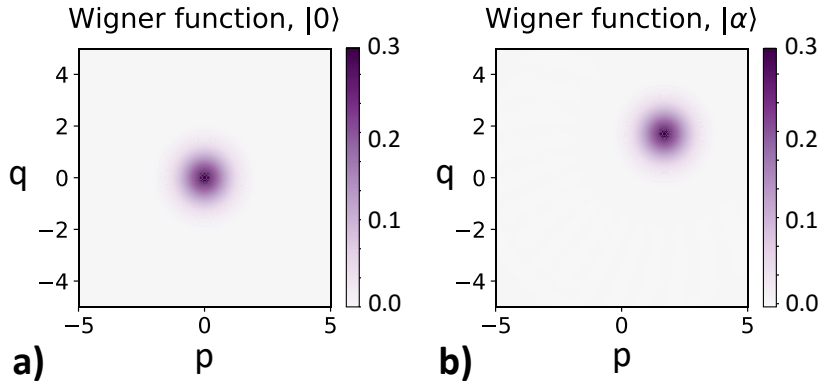

FIGURE 2.2: Wigner function of coherent states [6]. a) Vacuum state. b) Displaced coherent state with ∼2 photons.

with a non-zero amplitude is instead obtained as a displacement from the origin (Fig. 2.2b). A coherent state $|\alpha\rangle$ is built as an eigenstate of the ladder operators

$$\hat{a}\,|\alpha\rangle = \alpha\,|\alpha\rangle\,. \tag{2.16}$$

It can be obtained acting on the vacuum $|0\rangle$ with the displacement operator

$$|\alpha\rangle = e^{\alpha\hat{a}^\dagger - \alpha^*\hat{a}}\,|0\rangle\,. \tag{2.17}$$

The complex eigenvalue $\alpha = |\alpha|e^{i\varphi}$ is representative of the amplitude and phase of the electromagnetic wave. Its squared modulus accounts for the mean number of photons in the examined optical mode (i.e. the field intensity)

$$\langle\hat{N}\rangle = \langle\hat{a}^\dagger\hat{a}\rangle = |\alpha|^2. \tag{2.18}$$

Moreover, the coherent states are characterized by a poissonian photon number distribution. Hence the number variance reads

$$\sigma_N^2 = \langle\hat{N}^2\rangle - \langle\hat{N}\rangle^2 = \langle\hat{N}\rangle\,. \tag{2.19}$$

In Chapter 4 we will refer to these elements in order to test the coherent nature of the laser radiation employed in our experiments.

Quantum states

Beyond coherent states, in quantum optics other typologies of light states are widely studied and exploited for their non-classical properties. A convenient representation of quantum states of the optical radiation is provided by their Wigner function. We present in Fig. 2.3 some relevant examples of Wigner distributions [6]. The first example is relative to the squeezed states [7]. These are coherent states in

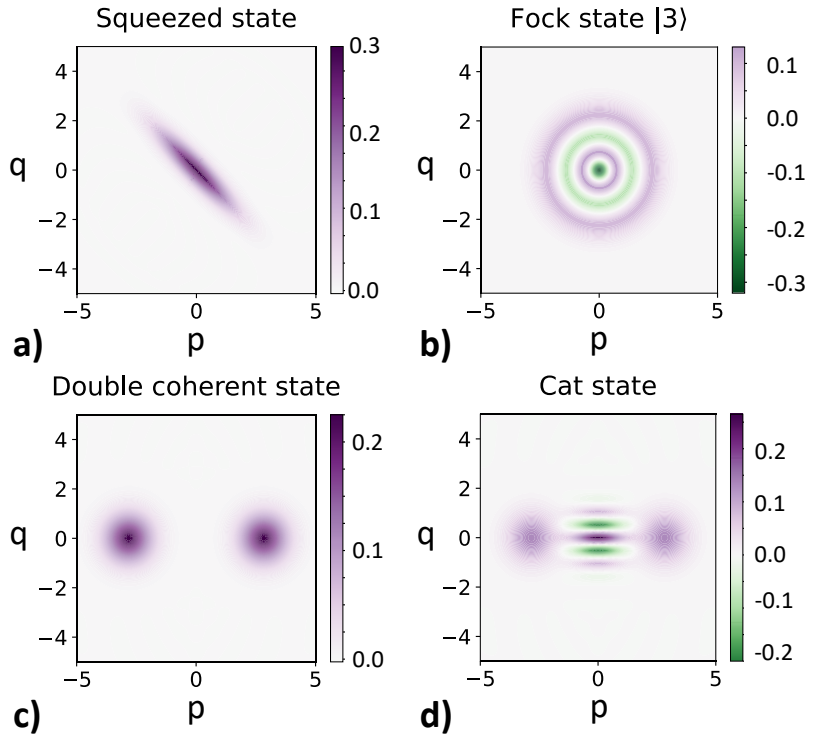

FIGURE 2.3: Wigner function of quantum states [6] a) Squeezed state. b) Photon number Fock state with 3 photons. c) Incoherent superposition of coherent state with opposite phase. d) Schrödinger-Cat state.

which the Heisenberg indetermination region is no longer isotropic (Fig. 2.3a). Remarkably, the width of the distribution on a phase-space marginal projection can be reduced below the vacuum level at the expense of increased uncertainty in the conjugated variable. This capability to control the statistics is of great importance, in particular exploiting the noise reduction below the vacuum level is of paramount importance in metrology [8].

Another striking example of non-classical statistics is the one of photon number states. These describe systems where in every repeated measurement a constant number of photons is detected. On the other hand the phase of the field is completely randomized. Formally these objects are described as elements of the Fock basis. In Fig. 2.3b we show for instance the Fock state $|3\rangle$ with 3 photons in the field. The strictly quantum character of the considered state is signaled by the negative values in the Wigner distribution.

In the end, we discuss the interference effects between states. We compare a classical incoherent superposition of coherent states with opposite phase (Fig. 2.3c) and their coherent quantum superposition (Fig. 2.3d), which is also known as Schrödinger cat state. We appreciate that while the classical case is the sum of the two initial distributions, in the quantum superposition the interference effect is represented by the presence of fringes in the Wigner function [9].

2.3 Optical Tomography

In this section we present the methodology employed to measure the quantum state. It consists in a tomographic procedure, which calculates the full Wigner function 2-D map basing on an ensemble of 1-D projections. The employed projections are the marginal phase-space distributions of the Wigner function, which can be measured acquiring the statistics of the phase-space variables in repeated experiments.
Adapting the expression in eq. (2.14) specifying the general q, p phase-space variables as the X, Y field quadratures of the light harmonic oscillator, we get the expression for the marginal projections for the quadrature along the ϕ direction.

$$w(X,\phi) = \langle X_\phi | \hat{\rho} | X_\phi \rangle = \int_{\mathbb{R}} dY W_\rho(X\cos\phi - Y\sin\phi, X\sin\phi + Y\cos\phi). \qquad (2.20)$$

We visualize in Fig. 2.4 the calculation of marginal distribution in the case of a gaussian coherent state.

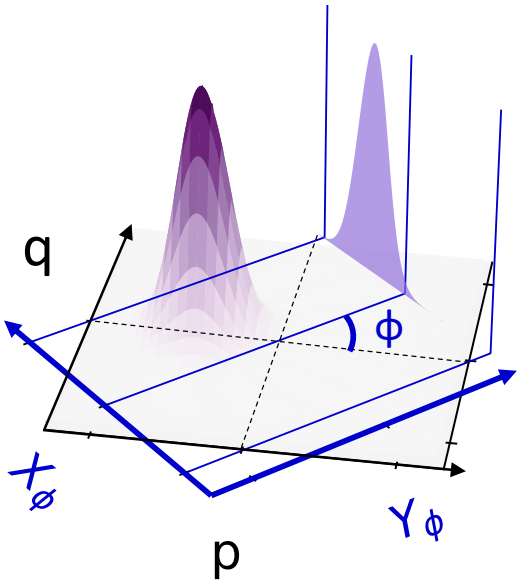

FIGURE 2.4: Representation of the marginal Wigner distribution calculation for the generalized quadrature X_ϕ. The full state is characterized collecting the different projections around the phase-space. In the example we show a displaced coherent state.

We now discuss the strategies to retrieve the full quantum state information starting from the ensemble of quadrature projections. Firstly, we report the algorithm to reconstruct the state Wigner function from the input distributions. Then, we describe the pattern tomography approach, which aims at obtaining the expectation values of a general observable without performing the explicit calculation of the Wigner function.

2.3.1 Wigner function reconstruction

From the mathematical perspective, the calculation in eq. (2.20) represents a Radon transform of the Wigner function. In order to reconstruct it we invert such relation and apply an Inverse-Radon transform algorithm [4]. Defining the polar

coordinates (r, ϕ) in the phase-space, the Wigner distribution is obtained as

$$W_\rho(q,p) = \frac{1}{4\pi^2}\int_0^\pi d\phi \int_{\mathbb{R}} dX \int_{\mathbb{R}} dr|r| e^{ir(q\cos\phi + p\sin\phi - X)} w(X,\phi). \tag{2.21}$$

From the practical point of view, the measured quantities are the amplitude and phase of the quadrature experimental realizations $[X_i, \phi_i]$, where i labels the M acquired repetitions. Therefore, the Wigner function can be approximated by an estimator acting on the dataset as

$$W_\rho \simeq {W_\rho}^{(M)} = \frac{1}{M}\sum_{i=1}^{M} \mathcal{K}_{X_i,\phi_i}(q,p) \tag{2.22}$$

which is an average on the outcomes of the kernel function $\mathcal{K}$. The explicit expression of the employed kernel [10] is given by

$$\mathcal{K}^{\eta,h}_{X_i,\phi_i}(q,p) = \int_{-\frac{1}{h}}^{+\frac{1}{h}} dr \frac{|r|}{4\pi} e^{-ir(q\cos\phi_i + p\sin\phi_i - \frac{X_i}{\sqrt{\eta}}) + r^2\frac{1-\eta}{4\eta}}. \tag{2.23}$$

which also takes into account a truncation parameter h to approximate the full integration and the detection efficiency η to include the effect of losses [11].

2.3.2 Pattern tomography

The Wigner function reconstruction with the inverse-Radon algorithm is useful to obtain a complete description of the full state, but the quantitative calculation of the system observables is affected by the presence of some artifacts linked to the sampling of the phase-space points and the truncated integration. For many applications it is possible to avoid the explicit calculation of the Wigner function and perform a direct calculation of the observable of interest adopting pattern tomography [5, 12]. The expectation value of a general observable can be calculated as a function of the quadrature distributions $w(X, \phi)$ with

$$\langle \hat{O} \rangle = \frac{1}{\pi}\int_0^\pi d\phi \int_{\mathbb{R}} dX\, w(X,\phi)\mathcal{R}[\hat{O}](X,\phi) \tag{2.24}$$

where the kernel function $\mathcal{R}$ is formally defined as

$$\mathcal{R}[\hat{O}](X,\phi) = \int_{\mathbb{R}} dr|r| \mathrm{Tr}[\hat{O} e^{ir(\hat{X}_\phi - X)}]. \tag{2.25}$$

For a general combination of ladder operators the latter can be expressed as

$$\mathcal{R}[(\hat{a}^\dagger)^n \hat{a}^m](X;\phi) = \frac{e^{i(m-n)\phi} H_{m+n}(X)}{\sqrt{2^{m+n}\binom{n+m}{m}}} \tag{2.26}$$

where $H_n(X)$ are Hermite polynomials.
If we include also the quantum efficiency η contribution to the measurement, eq. (2.26) becomes

$$\mathcal{R}_\eta[(\hat{a}^\dagger)^n \hat{a}^m](X;\phi) = \frac{e^{i(m-n)\phi} H_{m+n}(\sqrt{\eta}X)}{\sqrt{(2\eta)^{m+n}\binom{n+m}{m}}} \tag{2.27}$$

The explicit expression obtained from eq. (2.27) for some common observable is reported in Tab. 2.1. In particular, in our experiments we will focus on mean value

$\hat{O}$	$\mathcal{R}_\eta[\hat{O}](X,\phi)$
$\hat{a}$	$\sqrt{2}e^{i\phi}X$
$\hat{a}^2$	$e^{2i\phi}\left(2X^2-\frac{1}{\eta}\right)$
$\hat{X}_\theta$	$2X\cos(\phi-\theta)$
$\hat{X}_\theta^2$	$\frac{1}{2}\left\{1+\left(2X^2-\frac{1}{\eta}\right)[4\cos^2(\phi-\theta)-1]\right\}$
$\hat{a}^\dagger\hat{a}$	$X^2-\frac{1}{2\eta}$
$(\hat{a}^\dagger\hat{a})^2$	$\frac{2}{3}X^4-X^2\left(\frac{2-\eta}{\eta}\right)+\frac{1-\eta}{2\eta^2}$

TABLE 2.1: Patter tomography estimators of some useful operators.

and variance of the photon number, which are calculated as $\langle\hat{N}\rangle=\langle\hat{a}^\dagger\hat{a}\rangle$ and $\sigma_N^2=\langle\hat{N}^2\rangle-\langle\hat{N}\rangle^2$ exploiting the kernels $\mathcal{R}[\hat{N}]=\mathcal{R}[\hat{a}^\dagger\hat{a}]$ and $\mathcal{R}[\hat{N}^2]=\mathcal{R}[(\hat{a}^\dagger\hat{a})^2]$.

In summary, in this section we discussed how to obtain the information contained in the quantum state starting from the measurement of the distribution of phase-space quadratures. In the following, we discuss how to experimentally measure the quadrature of the optical field by means of heterodyne detection.

2.4 Balanced homodyne detection

The fundamental objects to perform the quantum state tomography are the phase-space projections representing the probability distribution of the field quadratures, $w(X,\phi)$. In order to calculate these we need a detection system able to measure the statistics of the quadrature operator $\hat{X}_\phi$. The suitable configuration to do so is the balanced homodyne detection [3, 13]. It is an interferential technique which consists in mixing the weak quantum probe field under examination with an intense reference field dubbed Local Oscillator (LO). The LO acts both as amplifier and phase reference for the probe field.
The term *homodyne* refers precisely to a setting in which probe and LO have the same spectral content. In our complete discussion, we adopt the more general *heterodyne* definition. We do it in order to better describe the multimode structure of the ultrashort pulses and also to reduce confusion between discordant definitions. Indeed, as noted by S. Mukamel [14, 15], in quantum optics the homodyne/heterodyne signal is interferometric detection with a local oscillator with the same/different frequency than the signal, otherwise in spectroscopy the term homodyne/heterodyne implies detection without/with a local oscillator. Therefore, the heterodyne definition allows us to satisfy both the two languages. We require a multi-frequency setting since in our experiments with multimode spectrum pulses we are in principle sensitive to light emitted, scattered or frequency-converted from the sample. Moreover, from the spectroscopy point of view, we clarify the use of the LO.

In this paragraph, we introduce the methodology starting from the simpler single-mode framework, where the quantum optical homodyne setting is appropriate. In Fig. 2.5 we display the structure of the homodyne detection scheme. We consider the probe under investigation described by the field operator $\hat{a}$. The LO is expressed with $\hat{z}$ and we can control its phase with the shift factor $e^{i\phi}$ (for example changing the

LO path). Probe and LO are then mixed together in a four-port 50:50 beam-splitter. The two outputs $\hat{d}_1, \hat{d}_2$ of the beam-splitter will be a mixture of the input fields. The

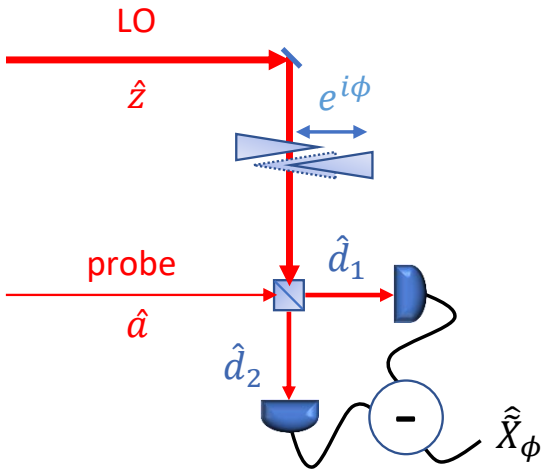

FIGURE 2.5: Balanced homodyne detection scheme. The probe under examination is mixed at a 50:50 beam splitter with an intense Local Oscillator reference. The phase of the LO can be controlled with a tunable delay. The outputs of the beam splitter, with opposite interference condition are collected by two diodes and subtracted to obtain the homodyne trace.

beam-splitter action is calculated with the matrix operation

$$\begin{pmatrix} \hat{d}_1 \\ \hat{d}_2 \end{pmatrix} = \frac{1}{\sqrt{2}} \begin{pmatrix} 1 & -1 \\ 1 & 1 \end{pmatrix} \begin{pmatrix} \hat{a} \\ \hat{z}e^{i\phi} \end{pmatrix} \tag{2.28}$$

which results in

$$\begin{cases} \hat{d}_1 = \frac{1}{\sqrt{2}}(\hat{a} + \hat{z}e^{i\phi}) \\ \hat{d}_2 = \frac{1}{\sqrt{2}}(\hat{a} - \hat{z}e^{i\phi}). \end{cases} \tag{2.29}$$

The two outputs present opposite interferential condition and are detected by two photodiodes which measure their intensity $\hat{d}^\dagger\hat{d}$. Finally, the homodyne trace $\hat{\hat{X}}$ is obtained subtracting the signals from the two diodes

$$\hat{\hat{X}} = \gamma(\hat{d}_1^\dagger\hat{d}_1 - \hat{d}_2^\dagger\hat{d}_2) \tag{2.30}$$

where γ is the proportionality factor which accounts for the adopted measurement units. We highlight that this measurement is acquired repeatedly on equally prepared states in order to collect the full statistics. The balanced differential scheme is crucial in order to cancel classical instabilities and retain only the intrinsic quantum fluctuations.
From the previous equation we make explicit

$$\hat{\hat{X}}(\phi) = \gamma(\hat{a}\hat{z}^\dagger e^{-i\phi} + \hat{a}^\dagger\hat{z}e^{i\phi}). \tag{2.31}$$

If we assume that the LO is a coherent state $\hat{z}\,|\zeta\rangle = \zeta\,|\zeta\rangle$ we can collect its amplitude when calculating the homodyne expectation value

$$\langle\hat{\hat{X}}(\phi)\rangle = \gamma\sqrt{2}|\zeta|\,\langle\hat{X}(\phi)\rangle\,, \tag{2.32}$$

which proves that the homodyne trace is proportional to the field quadrature. However, in order to completely demonstrate that the homodyne output allows us to measure the entire statistical distribution of the quadrature operator, we need to verify the proportionality at every order. This is a good approximation if the following hold

$$\begin{cases} \langle \hat{z}^\dagger \hat{z} \rangle \gg 1 \\ \langle \hat{z}^\dagger \hat{z} \rangle \gg \langle \hat{a}^\dagger \hat{a} \rangle \end{cases} \tag{2.33}$$

The first condition grants that the homodyne output has a continuous spectrum of values, the second that the corrections to

$$\langle \hat{\tilde{X}}^n(\phi) \rangle = (\gamma\sqrt{2}|\zeta|)^n \langle \hat{X}^n(\phi) \rangle + o\left(\frac{\langle \hat{a}^\dagger \hat{a} \rangle}{\langle \hat{z}^\dagger \hat{z} \rangle} \right) \tag{2.34}$$

are negligible.
In summary, the balanced homodyne detection scheme is a suitable configuration to measure the statistical distribution of the quadrature operators. Scanning the quadrature phase we can acquire the marginal projections around the entire phase-space and reconstruct the single-mode quantum state with a tomographic algorithm. The measured quantity is proportional to the amplitude of the intense LO oscillator, which means that the homodyne process amplifies the features of the quantum probe. For instance we highlight that vacuum state fluctuations of the probe field [16] are mapped through the LO statistics

$$\sigma^{2\,|0\rangle}_{\tilde{X}} = 2\gamma^2|\zeta|^2 \sigma^{2\,|0\rangle}_{X} = \gamma^2|\zeta|^2 \tag{2.35}$$

where we used the Heisenberg limit $\sigma^{2\,|0\rangle}_{X} = 1/2$.
Importantly, the measurement of the vacuum noise level is a key reference to derive the absolute calibration of the probe quadrature units.

2.5 Multimode heterodyne for ultrashort pulses

In the homodyne formalism developed so far, we discussed the study of a single mode of the radiation with polarization λ and frequency ω. Nevertheless, the complete analysis of the optical field requires to consider the sum over all the possible modes

$$\hat{\mathbf{E}}(\vec{x}, t) = i \sum_{\lambda} \sum_{\omega} \sqrt{\frac{\omega}{2V\epsilon_0}} \left(\vec{\mathrm{e}}_\lambda \hat{a}_{\lambda\omega} e^{-i(\omega t - \vec{k}_\omega \cdot \vec{x})} - \vec{\mathrm{e}}^*_\lambda \hat{a}^\dagger_{\lambda\omega} e^{i(\omega t - \vec{k}_\omega \cdot \vec{x})} \right) \tag{2.36}$$

with a more general heterodyne approach. Taking care of the multimode character is particularly relevant when dealing with short duration pulses, because owing to the time-energy formulation of the Heisemberg principle they present a broad frequency bandwidth. We will observe this in detail employing femtosecond laser pulses in ultrafast experiments.
The extension to a multimode setting enlarges the degrees of freedom available and the information processable in the system. In quantum optics this approach generates many applications in quantum computation and communication [17]. Remarkably, intriguing features arise as a consequence of the entanglement between different modes [18, 19].

From our spectroscopic point of view, the capabilities of the frequency-resolved formalism open the possibility to reveal spectral effects and intraband interactions due to light-matter interaction processes.

In this section, we discuss the polarization and frequency degrees of freedom of the radiation modes. We extend the previous description to a multimode heterodyne scheme and discuss the approach to reveal correlations between modes.
In detail, we approach the analysis describing the laser light in terms of multimode coherent states. These are built with independent coherent modes as

$$|\alpha\rangle = \otimes_{\lambda,j} |\alpha_{\lambda,j}\rangle = \exp\Big(\sum_{\lambda,j} \alpha_{\lambda,j}\hat{a}^\dagger_{\lambda,j} - \alpha^*_{\lambda,j}\hat{a}_{\lambda,j}\Big)|0\rangle\,. \tag{2.37}$$

The annihilation and creation operators $\hat{a}_{\lambda j}$ and $\hat{a}^\dagger_{\lambda j}$ are such that $[\hat{a}_{\lambda j}\,,\,\hat{a}^\dagger_{\lambda' j'}] = \delta_{jj'}\delta_{\lambda\lambda'}$, where λ, j are the polarization and frequency indices, respectively. In particular, we consider a set of modes with frequency spacing δ and offset ω_0 ($\leq \delta$), such that $\omega_j = j\delta + \omega_0$, with $j \in \mathbb{N}$. The available polarization modes are the two transverse $\lambda = x, y$.
Considering the analogy with classical waves, from the field operator expectation value

$$\langle \hat{a}_{\lambda,j}\rangle = |\alpha_{\lambda,j}|e^{i\varphi_{\lambda,j}} \tag{2.38}$$

we can identify the spectral amplitude $|\alpha_{\lambda,j}|$ and phase $\varphi_{\lambda,j}$.
We define as well the quantities relative to the LO field.

$$\langle \hat{z}_{\lambda,j}\rangle = |\zeta_{\lambda,j}|e^{i\varphi'_{\lambda,j}}. \tag{2.39}$$

We note that in general the LO spectral phase can be different by the probe one and for simplicity we will assume a LO with a flat phase ($\varphi'_{\lambda,j} = 0$).

2.5.1 Multimode heterodyne detection

In order to characterize the spectral features of the multimode optical state, we develop a frequency-resolved approach by means of balanced heterodyne detection. The heterodyne trace is calculated as the differential signal between the intensities of the fields $\hat{\mathbf{E}}_1, \hat{\mathbf{E}}_2$ measured on the two photodiodes

$$\hat{\tilde{X}} = \widetilde{\gamma}\int dt(|\hat{\mathbf{E}}_1|^2 - |\hat{\mathbf{E}}_2|^2) = \gamma\sum_{\lambda,j}(\hat{d}^\dagger_{1,\lambda j}\hat{d}_{1,\lambda j} - \hat{d}^\dagger_{2,\lambda j}\hat{d}_{2,\lambda j}). \tag{2.40}$$

The interference is effective only among modes with the same polarization and frequency. Orthogonal polarizations do not interfere. The frequency selection is a consequence of the long temporal integration of the detector with respect to the pulse durations[2], which averages to zero the contribution from mixed terms. The proportionality factors $\widetilde{\gamma}, \gamma$ account for the proper measurement units. Expressing the output fields $\hat{d}_1$ and $\hat{d}_2$, obtained in analogy with the beam-splitter action in (2.28), we get

$$\hat{\tilde{X}}(\phi) = \gamma\sum_{\lambda,j}(\hat{a}_{\lambda j}\hat{z}^\dagger_{\lambda j}e^{-i\phi} - \hat{a}^\dagger_{\lambda j}\hat{z}_{\lambda j}e^{i\phi}). \tag{2.41}$$

[2]The integration time is on the order of the photodiode rise/fall times (μs) while the convolution between probe and LO lasts at most tens of ps (when 0.1 THz resolution is employed).

We assume that the external phase control ϕ is equal for each component.
The mode resolution is obtained selecting a specific component. We discuss in the next chapter how to practically implement the selection from the experimental point of view. The formal mode-resolved heterodyne output is then

$$\hat{\tilde{X}}_{\lambda j}(\phi) = \gamma(\hat{a}_{\lambda j}\hat{z}^{\dagger}_{\lambda j}e^{-i\phi} - \hat{a}^{\dagger}_{\lambda j}\hat{z}_{\lambda j}e^{i\phi}). \tag{2.42}$$

The expectation value calculated on a multimode coherent state can be expressed as

$$\langle\hat{\tilde{X}}_{\lambda j}(\phi)\rangle = \gamma\sqrt{2}|\zeta_{\lambda j}|\,\langle\hat{\tilde{X}}_{\lambda j}(\phi)\rangle = \gamma 2|\zeta_{\lambda j}||\alpha_{\lambda j}|\cos(\phi - \varphi_{\lambda j}) \tag{2.43}$$

from which we can retrieve the probe amplitude and phase spectra.

2.5.2 Multimode correlation

The multimode coherent states we used to introduce the multimode formalism are the result of a combination of independent components. Nevertheless, the more general characterization of a multimode state requires not only the description of the individual subsystems, but also of their interdependence or correlation. These effects are usually the result of the interaction between different modes and are of interest both to investigate the generating process and the exotic attributes imparted on the output state.
The general density matrix of a separable (non-entangled) state is the direct product of the individual subsystems of the N considered modes.

$$\hat{\rho} = \otimes_{n=1}^{N}\hat{\rho}_n. \tag{2.44}$$

In this case, there is no relation between the single states and the measurement of arbitrary observables $\hat{A}, \hat{B}$ in different n and n' subsystems are independent

$$\langle\hat{A}_n\hat{B}_{n'}\rangle = \langle\hat{A}_n\rangle\,\langle\hat{B}_{n'}\rangle\,. \tag{2.45}$$

When the expectation value of the composite system is different from the product of the individual ones the previous equation does not hold anymore. This because the expression for the density matrix is no more factorizable, $\hat{\rho} \neq \otimes_{n=1}^{N}\hat{\rho}_n$ [20] in the specific basis of modes considered. However, adopting a different basis can result in a density matrix representation with a separable structure [17]. If it does not exist any choice of modes such that the density matrix is separable, then the multimode state is defined purely entangled.
Nonetheless, even in the absence of pure entanglement it can result more convenient to describe the system of interest in a basis with a non separable density matrix. For instance, it can be more significant to choose the mode basis according to the detection system than with respect to an indirect abstract representation.
Remarkably, in the entangled representations we can retrieve signatures of the correlation between parts imprinted in the joint statistics. Considering the violation of the relation in eq. (2.45), a useful estimator of the degree of correlation is given by the covariance

$$\mathrm{Cov}[\hat{A}_n, \hat{B}_{n'}] = \langle\hat{A}_n\hat{B}_{n'}\rangle - \langle\hat{A}_n\rangle\,\langle\hat{B}_{n'}\rangle \tag{2.46}$$

In the optical framework, we know that the fundamental quantities are the quadrature operators and we calculate the covariance among them. In particular, we can

analyze both the polarization and frequency correlation

$$\mathrm{Cov}[\hat{X}_{\lambda j}(\phi), \hat{X}_{\lambda' j'}(\phi')] = \langle \hat{X}_{\lambda j}(\phi)\hat{X}_{\lambda' j'}(\phi')\rangle - \langle \hat{X}_{\lambda j}(\phi)\rangle \langle \hat{X}_{\lambda' j'}(\phi')\rangle . \tag{2.47}$$

In conclusion, in this chapter we introduced the analysis of the quantum state of a multimode optical system via optical heterodyne tomography. In the next we describe the experimental implementation of the multimode heterodyne approach in the ultrafast pump&probe context.

Chapter 3

The experimental technique

The Time-resolved Multimode Heterodyne Detection approach is the result of the combination between the ultrafast pump&probe scheme and the balanced heterodyne detection. The goal of the technique is to monitor the full state of the probe light scattered from a sample driven impulsively out of equilibrium. We illustrate the concept of the experimental scheme in Fig. 3.1. In a standard pump&probe experiment, the intensity of the probe pulse is measured as a function of the relative delay Δt with which the two pulses reach the sample. The adoption of the heterodyne scheme improves the standard detection of the probe radiation. The mixing with an intense Local Oscillator (LO) field in the heterodyne interferometer both optically amplifies the probe field and provides a phase reference. In this way, it allows us to study weak probes in the quantum regime and access the field degree of freedom.

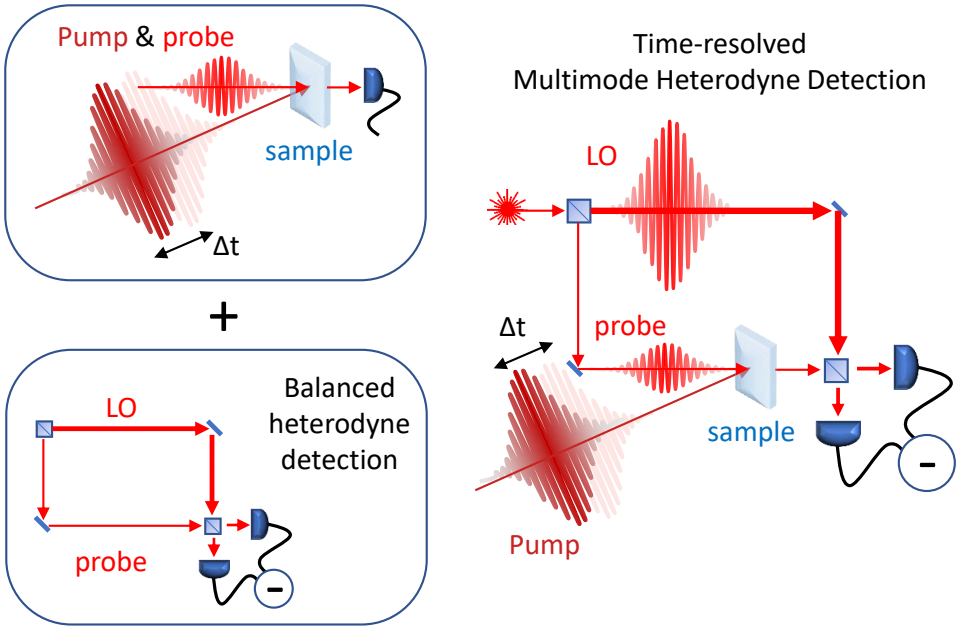

FIGURE 3.1: Time-resolved Multimode Heterodyne Detection results from the combination of ultrafast pump&probe experiment with a heterodyne detection interferential scheme.

In this chapter, we report the experimental details of the technique implementation. We start with an overview of the ultrafast setup and discuss the shaping capabilities of the ultrashort pulses employed. Then, we focus on the features of the multimode

approach, presenting the different optical schemes adopted to achieve frequency-resolved and correlation sensitive detection.

3.1 Overview of the pump&probe heterodyne setup

The time-resolved multimode heterodyne setup is sketched in Fig. 3.2 and it consists in a pulsed laser source which generates the ultrashort pulse repetitions employed in the pump&probe experiment, an optical interferometer, equipped with a double-pulse shaper, and a balanced differential detection.

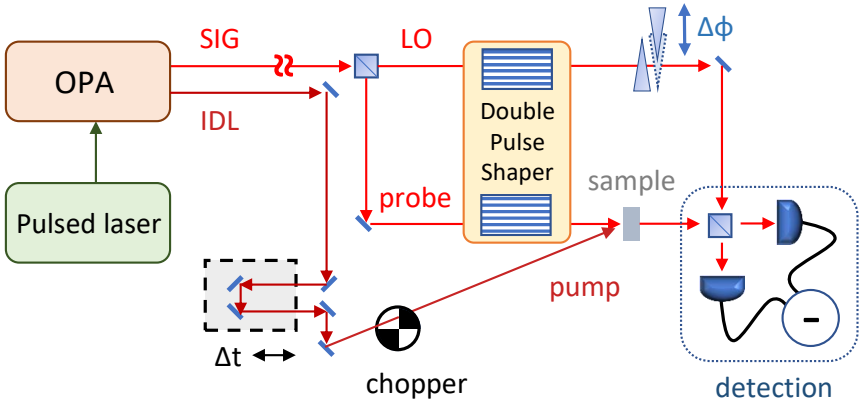

FIGURE 3.2: Layout of the experimental setup. Detailed description in text.

The laser system is made up of an Optical Parametric Amplifier (*Orpheus-F* by *Light Conversion*) pumped on the *Light Conversion Pharos Laser*. The laser source produces 100 μJ pulses with 1.2 eV photon energy and a duration <200 fs. The maximum repetition rate available is 200 kHz, but in our measurements we work at reduced sub-multiples to fit the detection speed. The two outputs of the OPA are a Signal and a Idler beam. The signal has a duration <50 fs and a tunable wavelength in the range of 650–900 nm (1.90-1.37 eV). The Idler is shorter than 100 fs, its energy is dependent on the Signal one (Sig+Idl = 2.4 eV) and spans the 1200–2500 nm (1.03-0.50 eV) range.
The Signal and Idler outputs are employed respectively to probe and pump the sample under examination. The Signal is split in a Local Oscillator and probe beams which are mixed in a Mach-Zehnder interferometer. The two arms of the interferometer are shaped independently in their amplitude and phase with a diffraction-based programmable shaper. The relative phase between LO and probe is controlled modifying the insertion of a pair of wedged windows.
The probe is transmitted[1] through the sample and combined with the LO in a balanced heterodyne detection scheme. Both probe and pump are focused at the sample and the respective spots have a diameter of 30 μm and 50 μm. The relative delay between pump and probe is instead tuned controlling the length of the pump path with a translation stage. On the pump path a chopper blade, rotating at a frequency sub-multiple of the laser rate in use, is employed to constantly reference the equilibrium response distinguishing the probe repetitions in *pumped* and *unpumped* dataset.

[1] In this thesis we treat transmission experiments, but in principle the setup can be adapted to a reflection configuration.

In the end, the probe transmitted through the sample is examined through the balanced heterodyne detection. In the most simple description the probe and LO are mixed on a non-polarizing 50:50 beam-splitter and equally divided between the two outputs, which are collected by the two channels of the differential detector. In our setup, we consider some more elaborated implementation scheme of the heterodyne measurement in order to fully exploit the multimode features and achieve frequency and polarization resolution. We will discuss a fast parallel acquisition of the various components with multi-channel arrays and a low-noise single-channel acquisition. In particular, we rely on the combination of heterodyne detection with pulse-shaping to frequency-resolve in the low-noise scheme. We dedicate specific sections in the following to illustrate the details of the developed detection configurations.

3.2 Optical pulse-shaping

A fundamental tool to improve the capabilities and versatility of the heterodyne setup is the pulse-shaper, which is used to tailor the probe and LO beams. In this section, we briefly introduce the diffraction-based programmable shaping of spectral amplitude and phase of the ultrashort pulses employed.
The spectral properties of a multimode pulse can indeed be manipulated by means of pulse-shaping techniques [21, 22, 23, 24]. A widely employed shaping scheme is the one relying on the spatial dispersion of the various spectral components. As exemplified in Fig. 3.3, the broad frequency bandwidth can be dispersed on the different frequency components, controlled and recombined in a $4f$-scheme. The different modes are horizontally focused in the Fourier plane by a cylindrical lens with focal length f. The modulation of the spectral attributes is obtained by the application of a spatial mask M in the focusing plane, which rules the propagation of the different modes of frequency ω as a function of the position in the Fourier plane. For instance, modulations in the mask absorption can be used to regulate the field amplitude or changes in the refractive index to induce phase shifts. In the end, the pulse bandwidth is reassembled following the reversed combination of optical elements.

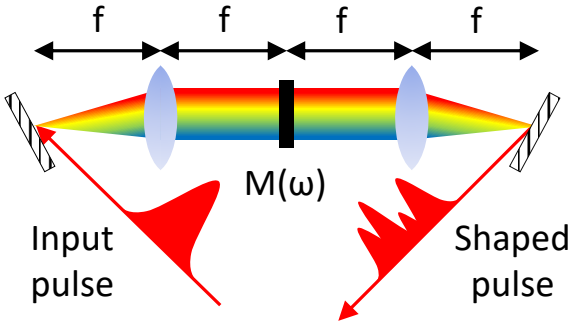

FIGURE 3.3: Pulse shaping scheme. The spectral components of the optical pulse are dispersed, focused on the Fourier plane and recombined in a 4f-scheme. The spatial mask M in the Fourier plane independently modifies the attributes of the various frequencies.

The characteristics of the output 'shaped' pulse are therefore dependent on the specific features of the adopted mask. Thus, tunable and programmable masks are required to gain control and variety of the shaping conditions. A suitable device to achieve this task is a Liquid-Crystal Spatial Light Modulator (LC-SLM).

The LC-SLM consists of a bi-dimensional screen composed by a pair of electrodes with a thin layer of nematic[2] liquid crystals placed between them. In particular, they are disposed in such a way that their director is parallel to the plane when no voltage is applied between them. The shaping capabilities of the device are based on the crystals birefringence. Owing to the anisotropic refractive index of the crystals, the phase of the light fields propagating through the liquid layer depends on the orientation of the nematic order (Fig. 3.4a), which can be controlled as a function of the applied voltage. In order to modulate the crystal orientation independently on different regions of the screen, the latter is formed by many pixel electrodes (Fig. 3.4b). In our setup we use the *Santec SLM-100* which is 1.5x1 cm wide with 1440x1050 pixels.

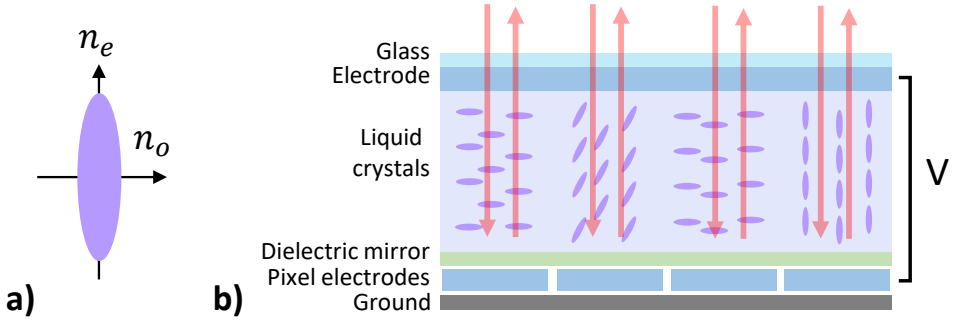

FIGURE 3.4: Operating principle of a Liquid-crystal based Spatial Light Modulator. The anisotropic refractive index of the nematic crystals (a) is employed to control the phase of the radiation. b) The nematic crystals are placed in between electrodes and their orientation is set as a function of the applied voltage.

In summary, the SLM is capable of building programmable 2D phase-masks. We now see how this ability can be exploited to shape not only the spectral phase, but also the amplitude.

Diffraction-based pulse-shaping

Contemporary shaping of spectral amplitude and phase of the optical pulse is achieved employing a 2D phase-mask in a diffraction-based configuration [22]. The intensity and the phase of the light diffracted from a grating are dependent on the spatial parameters of the periodic structure (Fig. 3.5a). The length of the diffraction period d rules the diffraction angle θ_m following the grating equation

$$d(sin\theta_m - sin\theta_i) = m\lambda, \tag{3.1}$$

where λ is the optical wavelength, θ_i the incidence angle and we consider the first order of diffraction $m = 1$. The optical phase of the diffracted beam can be tuned varying the phase of the periodic modulation, while the amplitude is dependent on the grating depth. Therefore, if we are able to regulate the grating profile, we can thus control the attributes of the diffracted light. In Fig. 3.5b, we represent how we can achieve this using the 2D SLM to produce programmable gratings. We can

[2]Liquid crystals are said to be in a nematic phase when their molecules have no positional order but tend to point in the same direction, identified as director.

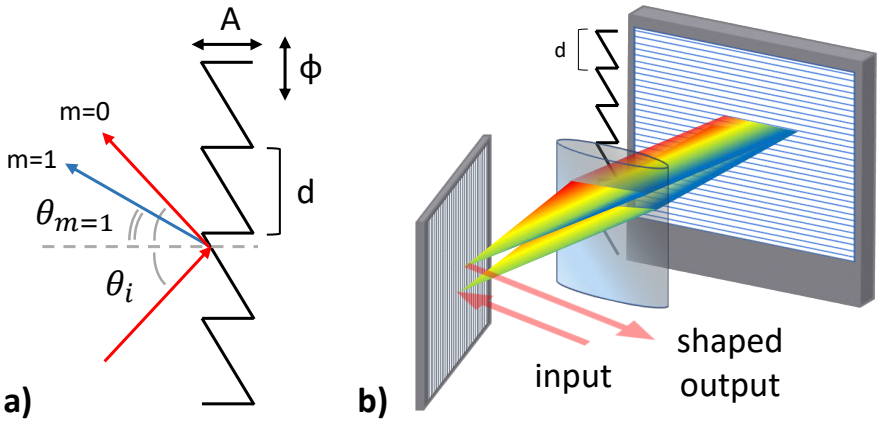

FIGURE 3.5: Diffraction-based pulse shaping. a) First-order diffraction from a grating is determined by the attribute of the periodic pattern (see text) b) Pulse shaper implementing a diffraction-based folded scheme consisting in a diffraction grating, cylindrical lens and a programmable LC-SLM screen.

indeed impart periodic modulations of the liquid crystal orientations, resulting in refractive index gratings. When employing a cylindrical lens, while along the x-axis the components are dispersed and focused, along the y-axis we can create a periodic phase grating. Moreover, we can set a different diffraction pattern for every frequency component. The frequency resolution will be limited by the SLM pixel size and the focus dimension along the x-axis.

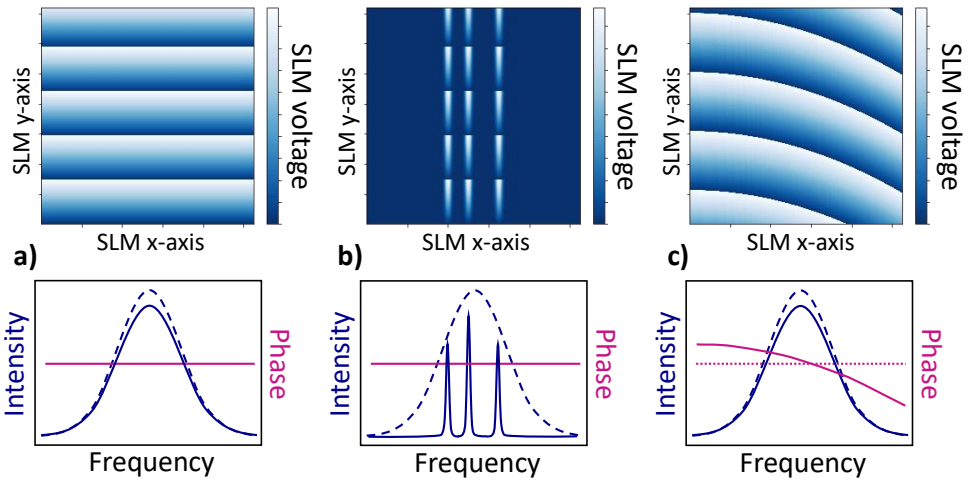

FIGURE 3.6: Examples of diffraction patterns for different shaping conditions. a) Unshaped condition. Spectral amplitude and phase are not modified with respect to the input pulse. b) Amplitude shaping. The spectral content is modified applying the grating only to selected components. c) Phase shaping. The shift of the grating phase modulates accordingly the spectral phase.

The spectral amplitude and phase of the output diffracted light can be shaped as a function of the gratings applied to each component. In Fig. 3.6 we report some example of 2D patterns visualized[3] in the SLM screen in order to achieve specific

[3]Precisely, we display only a reduced number of periods. On the SLM screen are actually present hundreds of them.

shaping conditions. In (a) we report the *unshaped* condition in which the relative amplitude and phase between spectral modes is not modified. In (b) we show the modulation of the spectral content by changing the grating depth. In particular, the blazed profile is applied only in three narrow regions of the spectrum, selecting three specific frequency components. In (c) we act instead on the spectral phase. The grating modulation is shifted in space quadratically as a function of the mode frequency. The resulting spectral phase follows the imparted trend and rules the temporal structure of the pulse. In particular, a quadratic modulation of the spectral phase results in a linear modification of the pulse chirp.

In the following sections, we will discuss the specific application of pulse-shaping in the multimode heterodyne detection experiment.

3.3 Multimode heterodyne detection

In section 2.5 we discussed the relevance of the multimode description [17] in the case of ultrashort laser pulses and introduced the formalism suitable for the multimode heterodyne measurement. Hereby, we present the experimental solutions adopted to implement the multimode heterodyne detection.
We employ two different acquisition schemes: a fast parallel acquisition of the spectral components with multichannel arrays of photodiodes and a low-noise detection with single-channel diodes combined with pulse-shaping. In addition, we introduce a polarization dependent optical design for the probe and LO recombination, which allow us to optimize the balanced detection and the correlation analysis.

3.3.1 Parallel array heterodyne detection

The simultaneous acquisition of many different spectral components in parallel is performed employing two multi-channel arrays of photodiodes. The full spectra

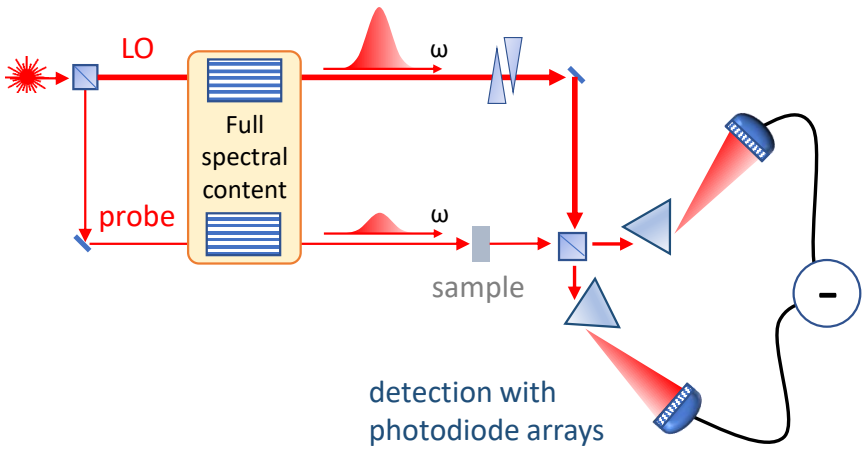

FIGURE 3.7: Parallel array detection scheme. The combined probe and LO beams are dispersed by prisms on a pair of multichannel arrays of photodiode detectors.

of the two heterodyne outputs are indeed equally dispersed by diffraction prisms and collected separately on the two arrays (Fig. 3.7). The acquisition is performed pulse-by-pulse and the resulting heterodyne trace is then the difference between the

separated array measurements.
The employed arrays are provided with 256 photodiodes (*Hamamatsu*) each and the home-built electronics permit to read the laser pulses at a maximum rate of 5 kHz. The energy resolution is limited by the optical spectral dispersion and focusing conditions and it is better than 2 meV.

3.3.2 Low-noise shaped heterodyne detection

As we discussed in Chapter 2, measuring the full quantum state of light means to characterize also the statistical properties of the radiation. Therefore, we need a detection system capable of measuring at best the optical noise, reducing instead the detrimental one coming from other sources. A useful scheme to improve this point consists in performing the subtraction between the two heterodyne outputs before the electrical amplification (Fig. 3.9a). In this way, the sum of the noise generated from two independent amplifiers is avoided. Adapting this solution to the multichannel setting is up to date still technically difficult. Therefore, in order to exploit the multimode frequency resolution in the low-noise single-channel configuration, we alternatively exploit pulse-shaping. As represented in Fig. 3.8, we select the desired frequency component to examine by shaping the LO content [19]. Hence, the amplification of the probe is effective only for the frequency corresponding to the selected LO mode.

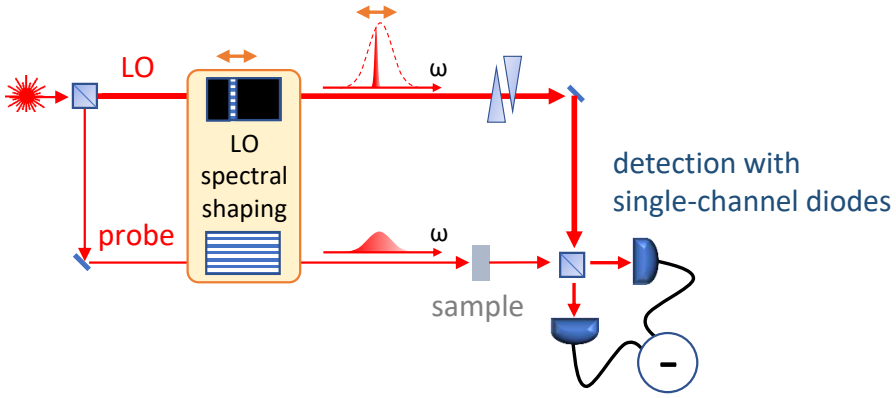

FIGURE 3.8: Low-noise shaped detection scheme. Frequency-resolved measurements are obtained with a low-noise single-channel detection by performing a mode selective heterodyne detection with a shaped Local Oscillator.

In the next paragraphs we report the details about the detector and double-shaper employed in our setup.

Low-noise differential detector

As mentioned, the single-channel heterodyne acquisition is performed by a low-noise differential detector. The currents produced by the illuminated photodiodes, which are connected in reverse bias, are directly subtracted prior to electronic amplification (Fig. 3.9a). We employ custom made detectors provided by *CAEN*, mounting *Hamamtsu S3883* Silicon photodiodes. The detector response (Fig. 3.9b) is then an analogic signal lasting $\sim 1\mu$s which is digitized with 30 MHz sampling and 16 bit dynamical range (*Spectrum M2i.exp*). The final acquired and saved output of the

measurement is the sum of the digitized point, weighted by the profile of the detector response. The maximum repetition rate of the laser pulses supported is 1 kHz, which is limited by the discharge time of the specific electronic components in use.

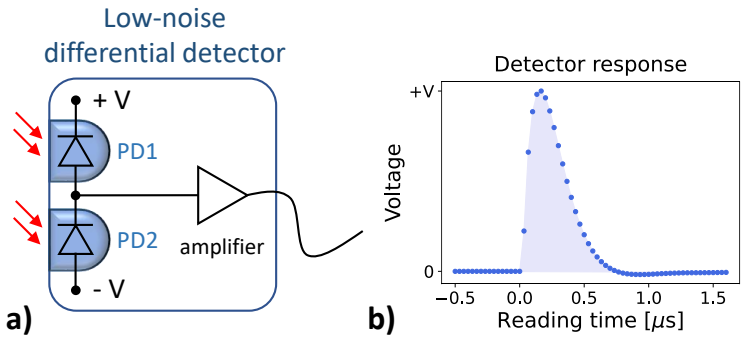

FIGURE 3.9: Low-noise differential detection. a) The currents produced by two photodiodes with opposite bias are directly subtracted before amplification. b) For every pulse repetition the detector produces a response curve which is digitized and integrated.

Double-pulse shaper

Our heterodyne setup is equipped with a double-pulse shaper able to control independently amplitude and phase of both probe and LO beams. The shaping capability is crucial in order to obtain frequency-resolution when dealing with single-channel detectors, but it is also very useful to control the temporal structure and compression of both the two pulses.

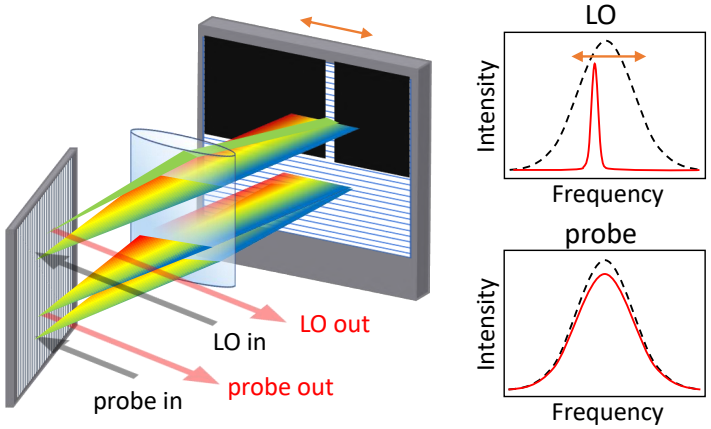

FIGURE 3.10: Double shaping scheme applied to the low-noise heterodyne detection. Probe and Local Oscillator are aligned on top of each other and shaped independently on different portions of same spatial light-modulator. The probe maintains its full spectral content, while in the LO is selected a narrow bandwidth.

As showed in Fig. 3.10, the double-shaping scheme is implemented aligning probe and LO one on top of the other and dividing the SLM screen in two parts.
In the specific case of frequency-resolved heterodyne with single-channel detection, the LO is shaped to a narrow spectral band which determines the examined probe

frequency. The shaper resolution in our setup is better than 0.4 meV. The probe pulse instead is not spectrally filtered, but the phase pattern is properly modulated in order to compress the pulse at the sample.

3.3.3 Balanced detection with tunable polarization splitting

The balanced subtraction of the two heterodyne outputs is a crucial parameter in order to properly cancel the classical noise and access the quantum fluctuations regime. However, from the practical point of view, the real specifications of commercial 50:50 non-polarizing beam splitter can deviate consistently (2-4 %) from the ideal splitting ratio. This issue can be improved adopting a polarization sensitive scheme [25, 26] as the one illustrated in Fig. 3.11. Indeed, the use of polarizing beam splitters and rotating waveplate allows us to finely tune the splitting ratio. In de-

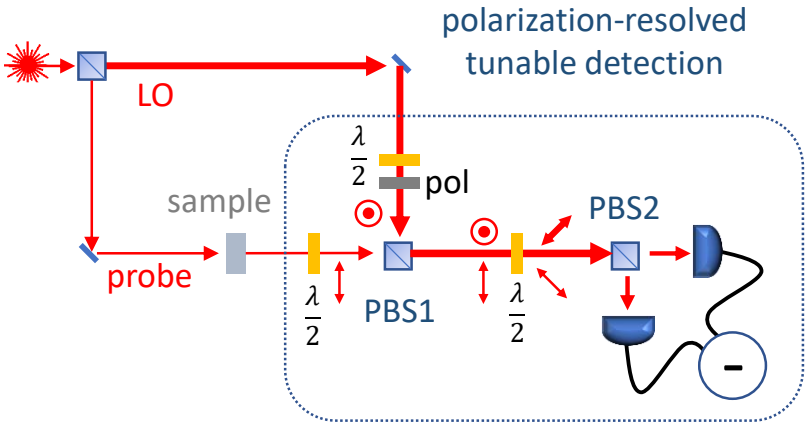

FIGURE 3.11: Tunable polarization splitting scheme. Polarization control optics (half-wave plates, polarizer and polarizing beam splitters) are exploited to developed an alternative scheme to the use of a single 50:50 beam splitter.

tail, polarizing beam-splitters (PBS) are objects which reflect the vertically polarized light and transmit the horizontal one. If we prepare probe and LO in two orthogonal states we can align them together on a single beam after PBS1. At this point, the polarization of both fields is rotated of 45° so that they are equally divided by PBS2. Remarkably, the polarization rotation can be tuned in order to get probe-LO with same intensity ratio on the the two channels. Furthermore, in order to balance the absolute amount of light in the two channels tunable attenuators can be employed. In addition to the balancing optimization, we highlight that this scheme is very useful also to implement more sophisticated detection schemes. Indeed, the recombination of probe and LO on a single beam increases the versatility of the optical design. Moreover, the polarization resolution enables the study of the polarization modes. In the following we see that these potentialities are particularly important for the study of correlations between modes.

3.4 Multimode correlation detection

In section 2.5.2 we discussed that a multimode state in general is not described by the sum of the individual subsystems, but information is contained also in the statistical correlations between them. We also defined the covariance between modes as a useful estimator of their interdependence.
We now describe the experimental measurement of the covariance between quadrature modes. In particular, we report both the analysis of frequency and polarization correlations.

3.4.1 Frequency correlation

Frequency-resolved measurements of the spectral bandwidth of optical pulses can be employed to reconstruct the covariance map of the multimode spectrum [18, 19, 27, 28]. Hereby, we show that sensitivity to statistical correlations can be obtained in both the parallel array and single-channel shaped detection schemes. The fundamental requirement is the contemporary pulse-by-pulse measurement of the two modes considered.

Parallel array detection

The parallel acquisition with the photodiode arrays is the fastest method to reconstruct the full covariance map. Indeed, measuring simultaneously 256 channels, recording a single train of pulse repetitions is sufficient to build the 256x256 symmetric covariance matrix between the outputs of the different components. Nevertheless, the noise performance of our array detectors is not high enough to measure the quantum fluctuations with high-quality, and it is relevant to implement the correlation detection also with the low-noise configuration.

Single-detector scheme

The low-noise detection permits to measure the covariance with high sensitivity, but it implies a point by point reconstruction of the covariance map, measuring a pair of modes at a time. While using the low-noise single-channel detection the role of pulse-shaping is crucial, because it is employed to shape in the LO the modes of the pair of frequencies under examination. Hence, with the setup depicted in Fig. 3.12 the statistics of the sum between the two considered quadrature modes is acquired.
In order to calculate the covariance is necessary to measure also the statistics of the individual modes. Then the covariance is given as a function of the variance of the different datasets as

$$\mathrm{Cov}[\hat{X}_{\omega_1}, \hat{X}_{\omega_1}] = \frac{1}{2}\left(\sigma^2_{\hat{X}_{\omega_1}+\hat{X}_{\omega_2}} - \sigma^2_{\hat{X}_{\omega_1}} - \sigma^2_{\hat{X}_{\omega_2}}\right). \tag{3.2}$$

Double-detector scheme

The polarization dependent splitting scheme proposed in Fig. 3.11 can be exploited, together with the use of a second single-channel detector, to speed up the acquisition time of the pair correlation in the low-noise setting. Designing the setup in Fig. 3.13 it is possible to record simultaneously and separately the two modes in analysis. In this way, it is possible to save the time required to reference the individual systems.

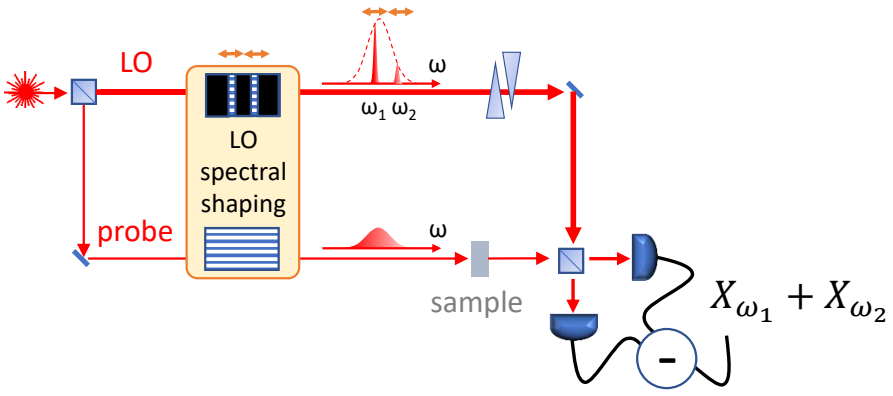

FIGURE 3.12: Frequency correlation detection scheme with a single-channel differential detector. The combined statistics of the state of a pair of modes is obtained shaping a double frequency spectrum in the LO.

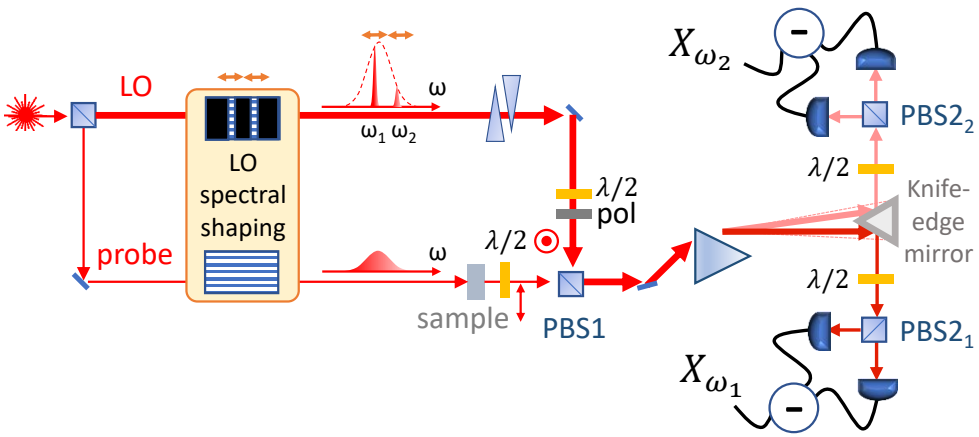

FIGURE 3.13: Double-detector frequency correlation detection scheme. The use of a pair of differential detectors allows for the contemporary low-noise acquisition of two separated frequency modes.

3.4.2 Polarization correlation

In addition to the multimode structure associated to the different frequency components, the optical fields also present two orthogonal polarization modes, which can carry different information and be correlated. The polarization dependent splitting in Fig. 3.11 can thus be conveniently adapted to reveal the full polarization state with the setup showed in Fig. 3.14. Precisely, the two outputs of PBS1 can be used

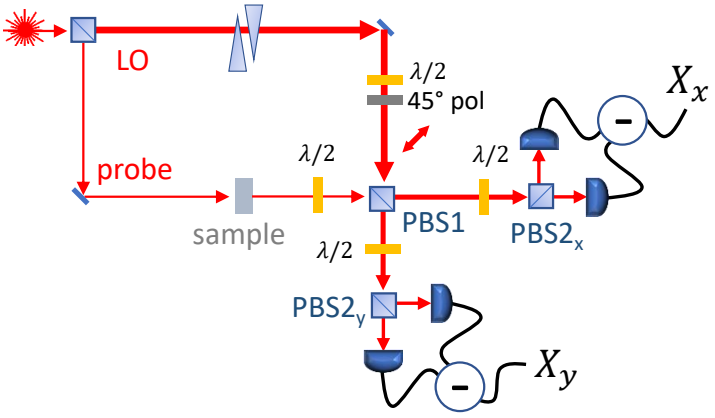

FIGURE 3.14: The polarization dependent splitting scheme allows for the contemporary acquisition of the two polarization modes with a pair of low-noise detectors.

to separate the x and y polarization components. In order to send LO light in both the polarization channels the linear polarization of the LO is oriented at 45° before PBS1. Finally, the separate heterodyne detection of the two polarization modes can be performed simultaneously with two detectors.
We highlight that this setup can be used to study the ellipticity of the probe polarization, which is important for instance when dealing with probes scattered from birefringent systems.

In the end we also underline that the frequency and polarization schemes described in this section, even if discussed separately, are not exclusive and can be implemented together.

Chapter 4

Characterization of the probe coherent state

In this chapter, we present the fundamental attributes of the ultrafast probe pulses employed in our multimode heterodyne detection experiments. Precisely, we test them in order to verify the consistency of their description in terms of coherent multimode states.
We report the results of typical frequency-resolved quadrature measurements attainable with the parallel array and low-noise detector acquisition schemes illustrated in the previous chapter. The single-pulse resolution is exploited to analyze the statistical distribution of repeated acquisitions and check the capability to work in the optical shot noise regime. The calibrated noise levels are then employed to perform a quantitative tomography reconstruction of the optical state.

4.1 Frequency-resolved quadrature map

Multimode heterodyne detection collects the field quadrature of different spectral components. Hence, the relevant degrees of freedom are the quadrature phase (i.e. the delay between probe and LO) and the mode frequency. The output of a measurement can therefore be pictured as a 2-D map, where the heterodyne spectral response is represented as a function of the LO delay.
In the following, we show and compare the frequency-resolved quadrature map acquired with the two detection schemes described in Chapter 3. At first we perform the simultaneous acquisition of the spectral components with multichannel array detectors. Then, we measure the frequency modes separately with the low-noise single-channel detectors exploiting pulse shaping of the LO.

Parallel detection

In the parallel detection configuration described in Fig. 3.7 in the previous chapter, the two output beams exiting the last beam-splitter are frequency dispersed and separately recorded by two multichannel array detectors with 256 pixels. The relative spectra are shown in Fig. 4.1a and are obtained averaging a thousand repetitions. Most of the observed intensity is relative to the LO light because in the examined case the probe intensity (10^5 photons/pulse) is 10^3 times weaker than the LO (10^8 photons/pulse). The probe induced interferential modulation (opposite in the two channels) is revealed by the difference of the two spectra, which is the heterodyne spectral response depicted in Fig. 4.1b. The heterodyne signal depends on the phase of the interference between probe and LO. The different responses reported describe the dependence of the spectral interference with respect to the probe-LO delay. In the present case of a Fourier-Transform-limited pulse, at the overlap all

the modes have the same interferential conditions and same sign of the heterodyne modulation, while fringes are observed if probe and LO are separated in time. This is a consequence of the frequency mismatch between different components, which acquire different phases for the same temporal probe-LO delay.

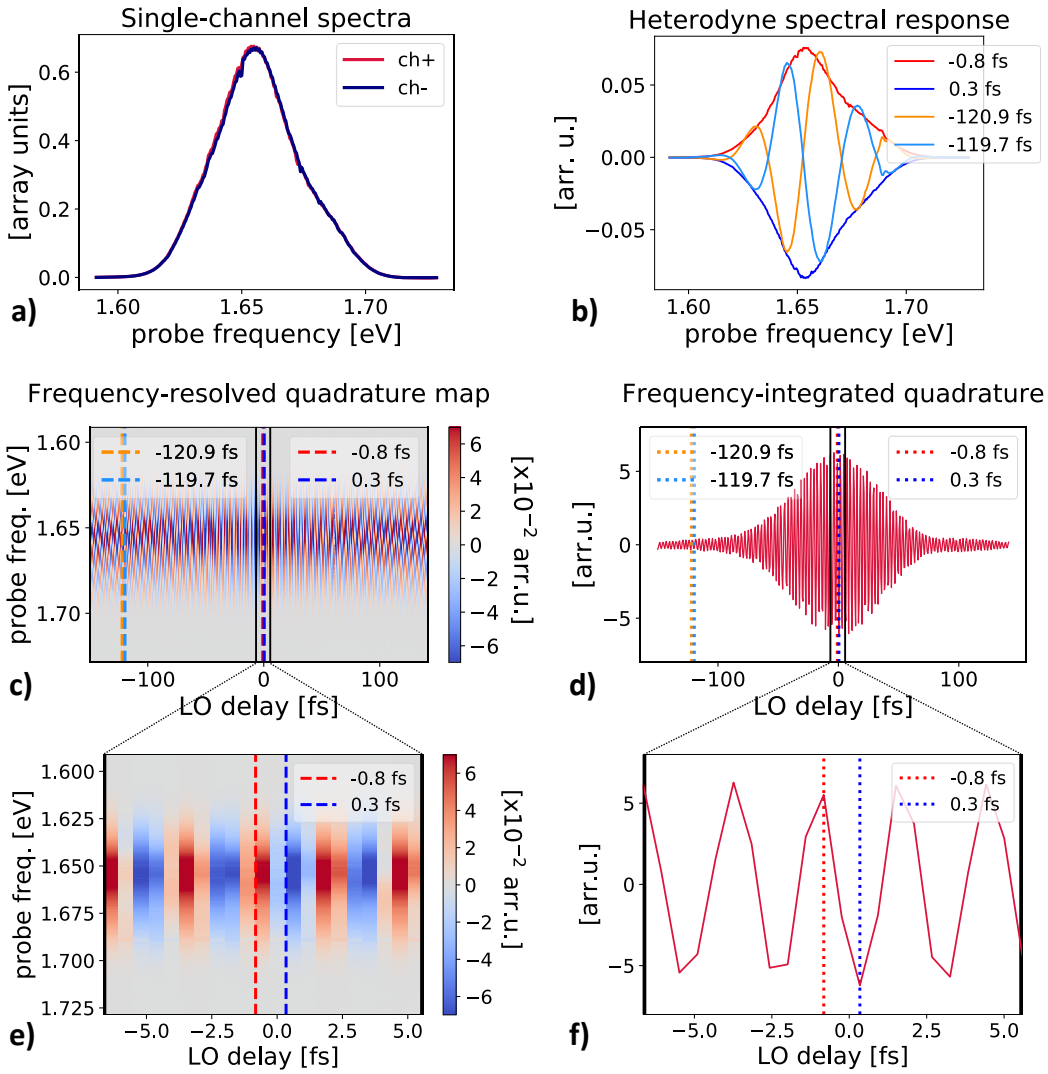

FIGURE 4.1: Quadrature map with parallel detection. a) Intensity spectra of the two photodiode arrays. b) Heterodyne differential signal obtained subtracting the two array spectra. The spectral profile of the interference fringes is dependent on the delay between probe and LO. c) Frequency-resolved quadrature map, measured for the different interference phases scanning the probe-LO delay. d) Frequency-integrated quadrature, obtained summing the map in (c), reveals the temporal convolution between probe and LO. e,f) Details of frequency-resolved and integrated quadrature in the central probe-LO overlap range.

The various heterodyne spectral traces acquired scanning the LO delay are collected to obtain the full frequency-resolved interferogram in Fig. 4.1c. The pulsed nature of the radiation employed is revealed by integration of the latter map along the frequency axis, which leads to the quadrature in Fig. 4.1d. The profile of its amplitude modulation, indeed, results from the convolution of the ∼50 fs long probe and LO pulses.

From the practical point of view, our measurements will generally limit the focus on few quadrature periods at the overlap, as detailed in Fig. 4.1e-f. There the phase mismatch between the different frequencies in the pulse bandwidth is still negligible. Thus, the relative phase between the mode quadratures in the overlap range is indicative of the difference between probe and LO spectral phases. If the two have the same spectral phase, the quadrature map has a flat phase profile. Otherwise, the phase trend depends on the relative chirp between the two. In the present example, both probe and LO are optimally compressed (Fourier-transform-limited). The absence of relative chirp is confirmed by the phase match between the quadratures of the spectral components.

Low-noise detection

The implementation of a low-noise differential detector, with the configuration shown in Fig. 3.8, allows us to improve the signal-to noise ratio of the measurement to the detriment of the capability to collect simultaneously many spectral modes. The spectral resolution is preserved thanks to the frequency selective amplification of the probe with a shaped LO and we build the frequency-resolved quadrature map (Fig. 4.2a) with subsequent acquisitions with different single-mode LOs (Fig. 4.2b).

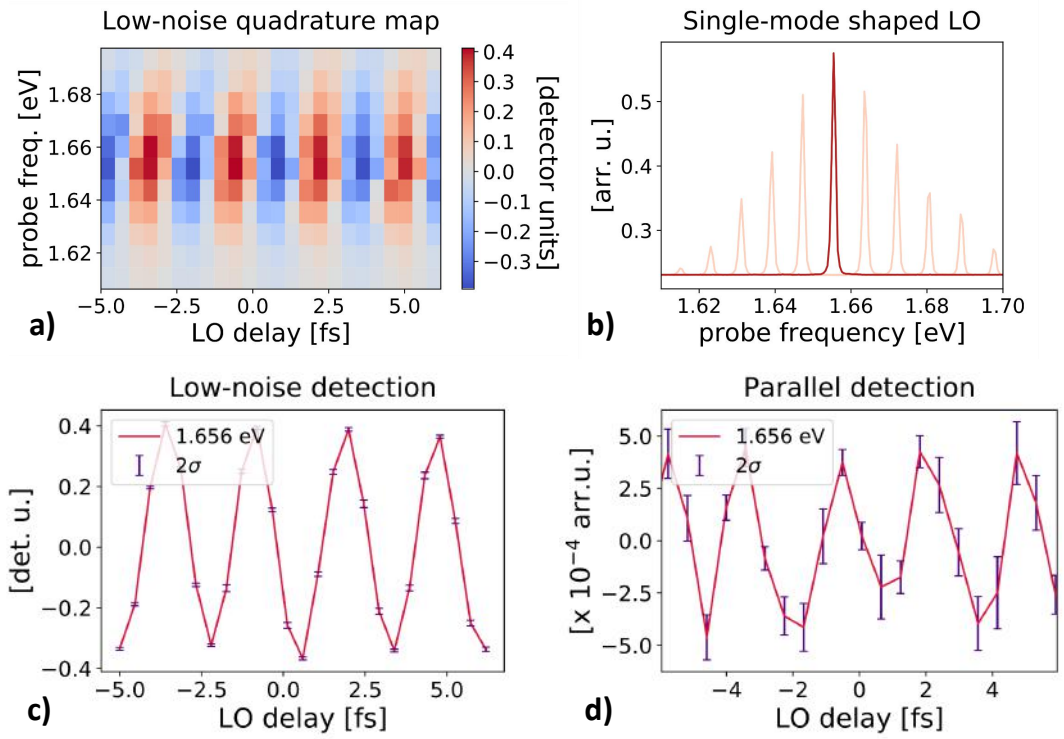

FIGURE 4.2: Multimode heterodyne measurement with low-noise detection. a) Frequency-resolved quadrature map, obtained combining low-noise single-mode acquisitions with various narrow LOs as a function of the probe-LO delay. b) Intensity spectra of the different single-mode shaped LOs employed. In red we highlight the single-mode LO used to measure the data in (c). c) Low-noise heterodyne trace of the central mode with about 10 photons per pulse in the signal beam. d) Quadrature of the central mode with 10 photons per pulse acquired with parallel array detection for comparison with (c).

The better quality of the measurement attained with the low-noise configuration

with respect to the parallel array acquisition can be appreciated comparing them in the same illumination condition. We consider a probe with $\sim$ 10 photons/pulse in the central mode and acquire 800 repetitions per point in the low-noise scheme (Fig. 4.2c) and 3000 repetitions with the arrays (Fig. 4.2d). The uncertainty is estimated as standard deviation (σ) of independent acquisitions and it reveals a signal-to-noise ratio 10 times better with the low-noise detection in this intensity regime.

4.2 Multimode noise characterization

The single-pulse detection methods used allow for the description of the experiment in terms of repeated measurements on equally prepared quantum states. Hence, we are able to collect the pulses statistical distribution, which is representative of the physical state of the examined light. Moreover, the balanced differential scheme adopted for the heterodyne detection removes classical-related instabilities and permits a discrimination of the intrinsic quantum fluctuations. In particular, performing a heterodyne measurement with the LO only, i.e. in the probe vacuum state, characterizes the quantum limited Shot Noise.
In order to verify our sensitivity to the quantum statistical properties of light, we need to distinguish the Shot Noise level from the electronic and laser instabilities. In this section, we quantify the different contributions and check the linear poissonian Shot Noise dependence on the photon number in comparison to the excess noise of super-poissonian classical sources.

4.2.1 Laser noise

At first, we analyze the spectral attributes of the laser radiation considering the multi-channel array acquisition of the LO light, shown in Fig. 4.3. In order to have a quantitative reference we calibrate the array readout units measuring the power of the incoming light. The repeated acquisition of the pulse spectrum forms a train of successive records at the laser rate (Fig. 4.3b). Thanks to this regular temporal spacing, we can apply a Fourier-Transform analysis in order to filter the frequency components linked to slow drifts and periodic noises.
We evaluate the spectral dependent variance of the datasets as a function of the incoming intensity. We observe that both original (Fig. 4.3c) and FT-filtered data (Fig. 4.3d) have a variance about 100 times bigger than the impinging intensity, signaling the presence of classical fluctuations exceeding the shot-noise level. We also note that the FT-filter is effective in reducing the random fluctuations and this smooths the spectral intensity dependence. The distribution is peaked at the spectral saddle points, suggesting a dominant contribution of frequency-jitter instabilities.

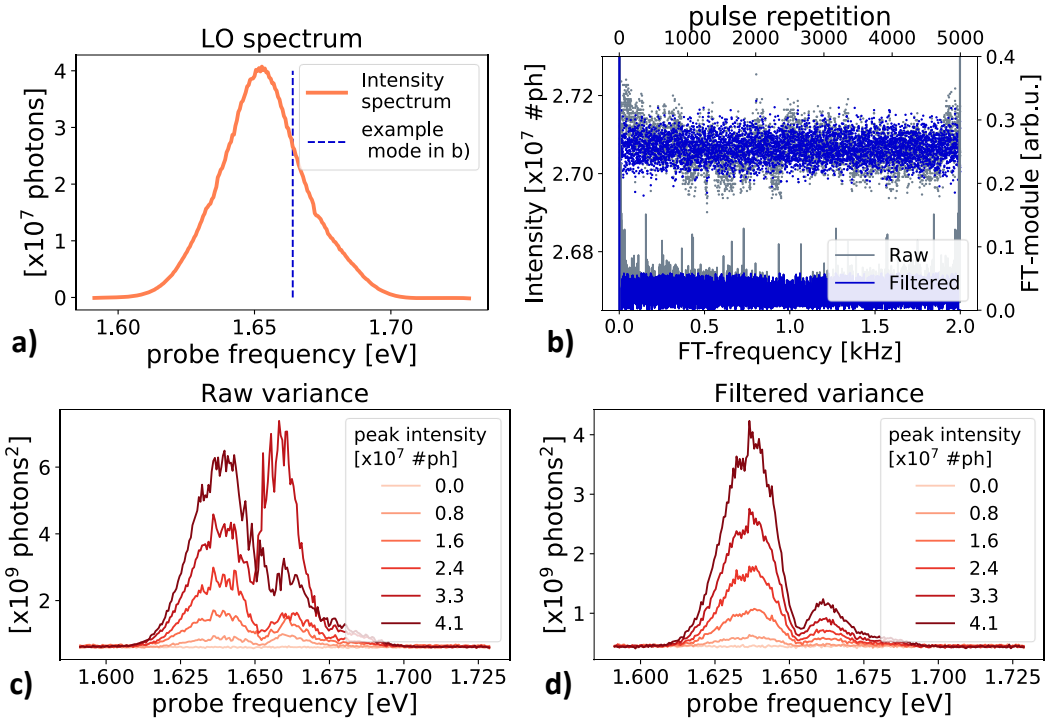

FIGURE 4.3: Intensity dependent spectral noise of the laser source. a) Intensity spectrum b) Raw and filtered set of pulses (top) with corresponding Fourier-Transform spectra (bottom). c) Raw data variance. d) FT-filtered variance. The FT-analysis reduces the noise removing periodic fluctuations and slow drifts. The variance peaked at the saddle points suggests the presence of frequency-jitter instabilities.

4.2.2 Shot Noise

The fundamental element to discriminate the intrinsic quantum noise from the environmental instabilities is the balanced differential scheme, through which classical fluctuations are canceled.

Parallel detection

In the case of multichannel detection, the subtraction is performed between the spectra acquired by the two photodiode arrays. We see in Fig. 4.4a that the differential acquisition strongly reduces the measured variance with respect to the one measured in Fig. 4.3. However, the dominant contribution is associated to the background response, which is representative of the detector Electronic Noise (EN) level. Considering the latter as an additive term, we discriminate the Shot Noise by subtracting the EN level to the full FT-filtered variance. The result is plotted in Fig. 4.4b, where the comparison with the LO intensity spectrum confirms the Shot Noise variance to be equal to the LO number of photons. In Fig. 4.4c the Shot Noise spectrum as a function of intensity is reported, highlighting the intensity dependent improvement of the Shot-to-Electronic noise ratio.

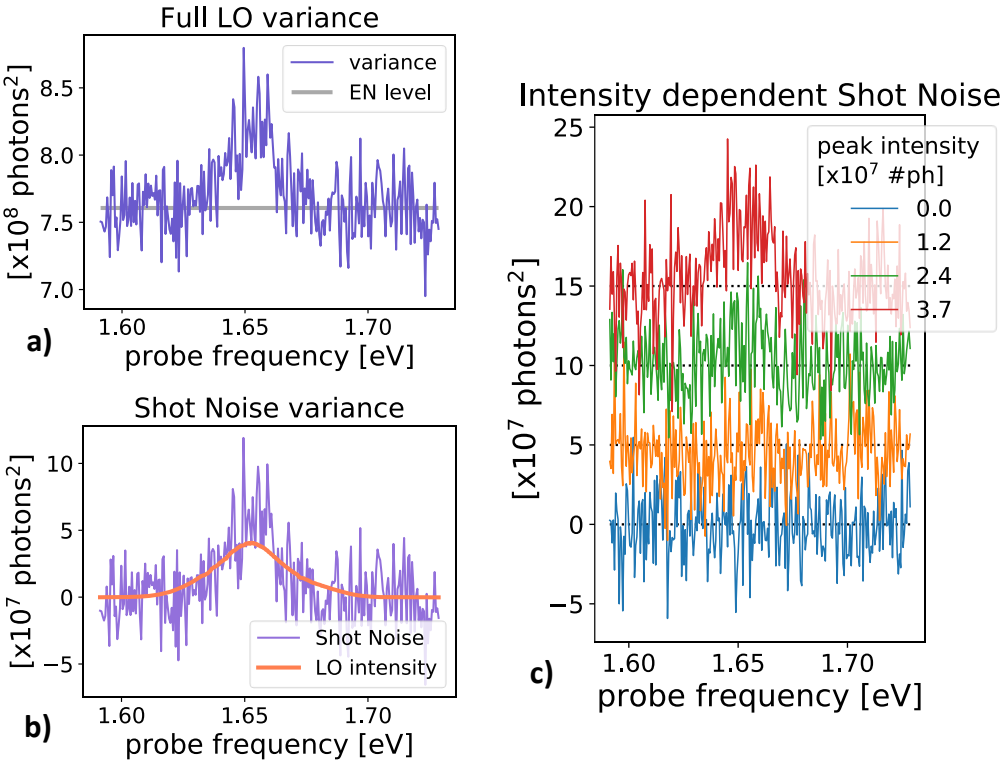

FIGURE 4.4: Shot Noise characterization with parallel detection. a) Full variance of the differential detection output. b) Shot Noise (SN) spectrum obtained subtracting the Electronic Noise (EN) to the full variance, compared with the LO intensity. c) Intensity dependent shot noise (shifted). The Shot Noise variance increases linearly with the optical intensity, improving the SN/EN ratio.

Low-noise detection

The Shot-to-Electronic Noise ratio, which estimates the quality of the quantum fluctuations measurement, is greatly increased by employing the low-noise differential detector. We characterize the Shot Noise response of our two low-noise detectors in the same measurement, exploiting the double-differential detector setup in Fig. 3.13. Thanks to a frequency splitting scheme, each detector collects a different side of the spectrum. As previously performed for the arrays, the detector outputs are calibrated in photon units.
The results in Fig. 4.5a show that the EN level is about two orders of magnitude smaller than with the photodiode array configuration, while the amount of employed LO light is comparable[1]. The Shot Noise (full variance-EN) dependence on LO intensity is displayed in Fig. 4.5b and the linear relation is highlighted for two selected modes in Fig. 4.5c. We highlight that the variance is equal to the number of LO photons.

[1]The direct subtraction prior to amplification in the low-noise scheme preserves the detector from saturating its differential response and permits to employ relatively high intensity LO even with a very sensitive detector.

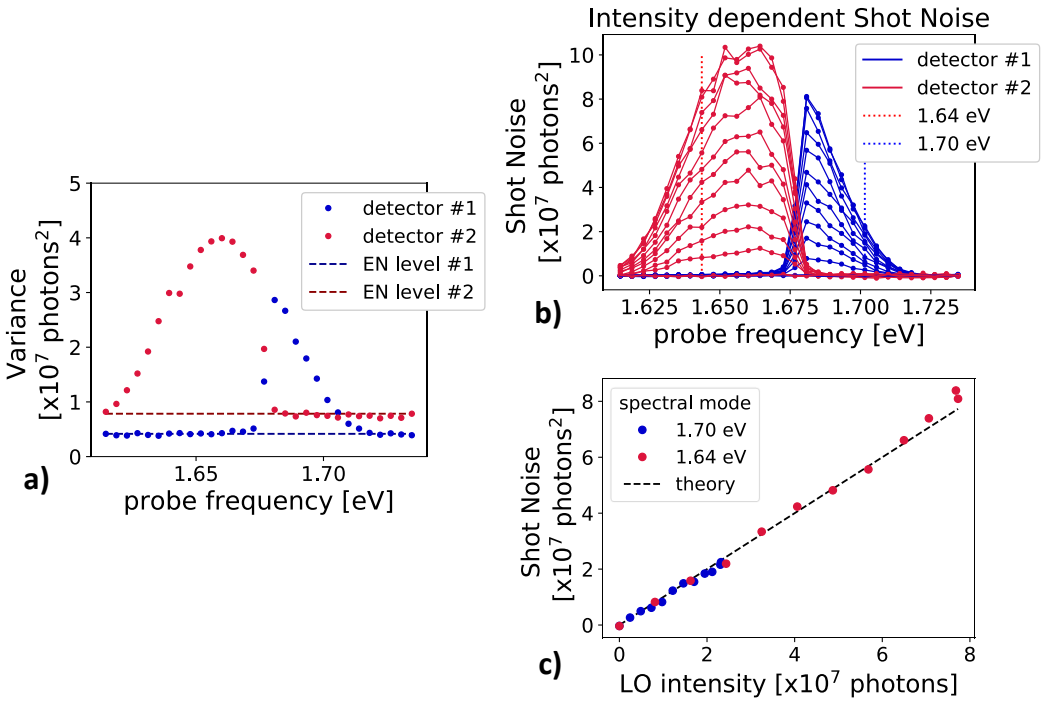

FIGURE 4.5: Shot Noise characterization with low-noise detection. The two sides of the probe spectrum are acquired by two separate detectors like in Fig. 3.13. a) Balanced heterodyne spectral noise. b) Spectral Shot Noise for different LO intensities. c) Linear dependence of the Shot Noise with respect to the LO intensity for selected frequency modes.

4.3 Probe state tomography

After having analyzed the properties of the LO and thus referenced the probe vacuum state, we focus on obtaining the full characterization of the probe field through heterodyne detection. In particular, in this section we present the analysis to achieve the optical tomography of the coherent probe state in the photon phase space.
Experimentally, we collect in the frequency-resolved quadrature map the heterodyne trace output $\tilde{X}$ which is generally proportional to the field quadrature X, expressed in phase space units (see derivation of eq. 2.32),

$$\tilde{X}_\omega(\phi^{LO}) = \gamma\sqrt{2}|z_\omega|X_\omega(\phi^{LO}) \tag{4.1}$$

where z, X are expressed in photon field units and γ is the unit conversion factor for the arbitrary $\tilde{X}$ units. In order to perform quantitative estimations in phase space units, we need to renormalize the output with

$$X_\omega = \frac{\tilde{X}_\omega}{\gamma\sqrt{2}|z_\omega|}. \tag{4.2}$$

The required factors can be obtained with calibrated intensity measurements. If it is not possible to externally calibrate the acquisition units or to quantify the LO components in terms of number of photons, we can exploit the absolute intrinsic reference given by the LO Shot Noise, which maps the vacuum noise. Indeed, the quadrature

operator variance for the vacuum state in phase space units is

$$\sigma^2_X{}^{|0\rangle} = \langle 0| X^2 - \bar{X}^2 |0\rangle = \frac{1}{2} \tag{4.3}$$

while the measured variance reads

$$\sigma^2_{\tilde{X}}{}^{|0\rangle} = \gamma^2 |z|^2. \tag{4.4}$$

Therefore, with this reference we get an evaluation of the factor $\gamma|z|$ and the measured trace can be renormalized to photon phase space units as

$$X = \frac{\tilde{X}}{\sqrt{2\sigma^2_{\tilde{X}}{}^{|0\rangle}}}. \tag{4.5}$$

Actually, in the presence of electronic noise (EN) [10, 11], the measured variance would be overestimated, $\sigma^2_{\tilde{X}}{}^{|0\rangle} = \gamma^2|z|^2 + EN$, and the normalization must be corrected as

$$X = \frac{\tilde{X}}{\sqrt{2(\sigma^2_{\tilde{X}}{}^{|0\rangle} - EN)}}. \tag{4.6}$$

We present an example of normalized heterodyne trace in Fig. 4.6, showing its quadrature mean value and variance. We select a narrow frequency mode in the spectrum (1.64 eV, 0.5 meV bandwidth). In order to have an independent test on the amplitude of the quadrature measured, we record the probe intensity with a power meter. Precisely, since we perform the experiments with a beam too weak to be directly detected, we measure it before attenuation with a calibrated filter. The intensity of the considered probe mode is about 1 photon/pulse.

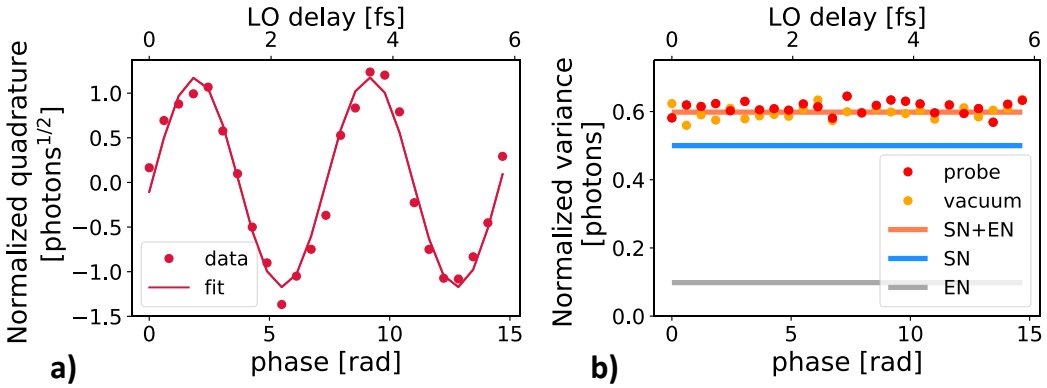

FIGURE 4.6: Quadrature normalized in photon phase space units. a) Mean-value data and relative fit. b) Normalized variance and reference noise levels.

Recalling that for a coherent state $|\alpha_\omega\rangle$ we have

$$\langle X_\omega(\phi^{LO})\rangle = \frac{1}{\sqrt{2}} \langle a_\omega e^{-i\phi^{LO}} + a^\dagger_\omega e^{i\phi^{LO}} \rangle = \sqrt{2}|a_\omega| \cos(\omega t + \phi_\omega + \phi^{LO}), \tag{4.7}$$

it is insightful to perform a sinusoidal fit $f = A\cos(\omega(t + \Delta t^{LO}) + \phi_\omega)$ with respect to the LO delay Δt^{LO} (Fig. 4.6a). Considering that the mean photon number can be

expressed as $\langle I \rangle = |\alpha|^2$ we can estimate it from the fit as $\langle I \rangle = \frac{A^2}{2}$. In the present example we have $\langle I \rangle = 0.69 \pm 0.06$ photons/pulse (fit error, uncertainty on calibration neglected). We underline that the result agrees with the expected value from the intensity estimation with power meter and calibrated filter.
Regarding the variance, we see in Fig. 4.6b that, as expected for a coherent state, there is no evident dependence on the quadrature phase and that quantitatively it is set at the vacuum level defined by the sum of the Shot (=1/2) and Electronic Noise.

In order to obtain a more complete representation of the optical state in analysis, we perform the tomography reconstruction of the phase space Wigner function, as previously presented in section 2.3. Loading as input of the reconstruction algorithm the quadrature and phase (X_i, ϕ_i) of every single-pulse experimental realization, we calculate as output the quasi-probability Wigner distribution. In Fig. 4.7 we display the results retrieved for the reference vacuum state (a) and for the considered probe with a mean photon number ~ 1 (b).

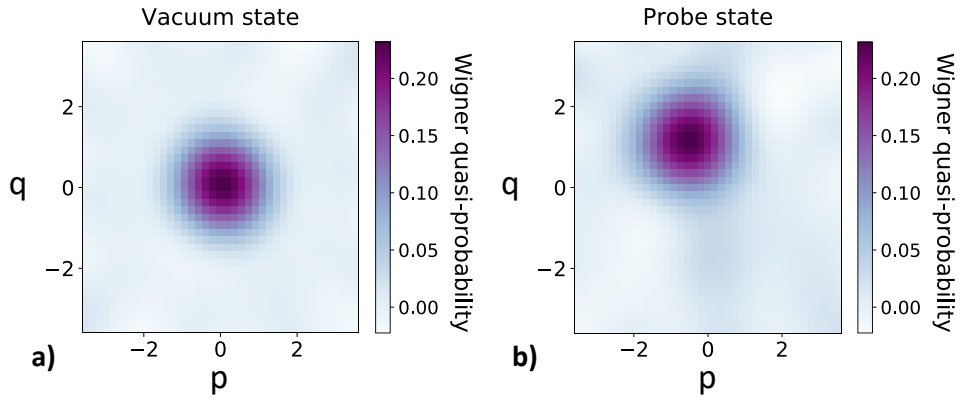

FIGURE 4.7: Measured probe Wigner function. a) Vacuum state b) Coherent state of the probe mode with a mean photon number of about 1 photon/pulse.

We observe that the vacuum state is a gaussian state centered at the phase space origin, while the probe state is displaced due to its coherent amplitude. From the quantitative point of view, we calculate the expectation value for the number operator and its variance employing the pattern tomography estimators presented in eq. (2.27). The inefficiency introduced by the electronic noise can be corrected by setting the estimator efficiency parameter [10, 11] to

$$\eta = \frac{SN}{SN + EN}. \tag{4.8}$$

We report the results in Tab. 4.1 and we comment that the obtained values are in agreement with the expected intensity and with the poissonian statistics ($N = \sigma_N^2$) proper of a coherent state.

TABLE 4.1: Result of the pattern tomography reconstruction of the considered optical mode for the photon number operator and its variance.

	N [#photons]	σ_N^2 [#photons^2]
probe (fit)	$0.69 \pm .0.06$	-
probe	0.67 ± 0.03	0.74 ± 0.10
vacuum	0.00 ± 0.01	0.01 ± 0.03

4.4 Frequency correlation

As introduced in section 2.5.2, the multimode nature of the ultrashort pulses employed allows us to explore the correlation and entanglement between different components. The multimode structure of the considered coherent state description is built as a tensor product of the single-frequency components, $|\alpha\rangle = \otimes_\omega |\alpha_\omega\rangle$. Therefore, in this framework the spectral modes are independent and correlation among them should not arise.
We verify the uncorrelated character of the probe light measuring the experimental covariance between modes. In order to discuss our setup sensitivity to the attributes of the quantum limited Shot Noise, we discriminate the contributions associated to the detector noise and to the classical fluctuations of the laser source.

4.4.1 Environmental setup correlations

While the quantum fluctuation of the coherent state are independent for the various spectral modes, some extrinsic correlation can be introduced by other noise sources in the setup.
The parallel multichannel acquisition is well-suited to simultaneously acquire the covariance map for a large number of components. As a drawback, though, we already observed in Fig. 4.4 that our array detectors are affected by a non-negligible readout noise. Moreover, in Fig. 4.8a we record the covariance map of the empty detector and we note some stripes out of the diagonal. These modulations signal the correlation set by a cross-talk effect between the array diodes and limit the performance of the detection scheme.
In comparison, we underline that the low-noise detection configuration avoids this issue because the differential detector is realized with separated diodes and in the double-detector scheme two modes are analyzed by two distinct devices.
Another noise contribution in the experiment arises from the instabilities of the laser system. We characterize them by acquiring the covariance map of the LO spectrum with an array detector (Fig. 4.8b). In Fig. 4.4 we showed the features of the variance, which we now equivalently retrieve along the diagonal of the covariance map. The checkered structure of the map describes fluctuations of the same sign for modes on the same side of the frequency spectrum, while anti-correlated deviations for modes at the opposite side. This result is representative of instabilities dominated by frequency-jitters of the pulse spectral content.
Since the latter statistical features are proper of the laser source, they affect the experiment whatever the detection device we adopt. Nevertheless, the balanced differential heterodyne subtraction is effective in canceling the undesired classical fluctuations and discriminating the quantum statistics.

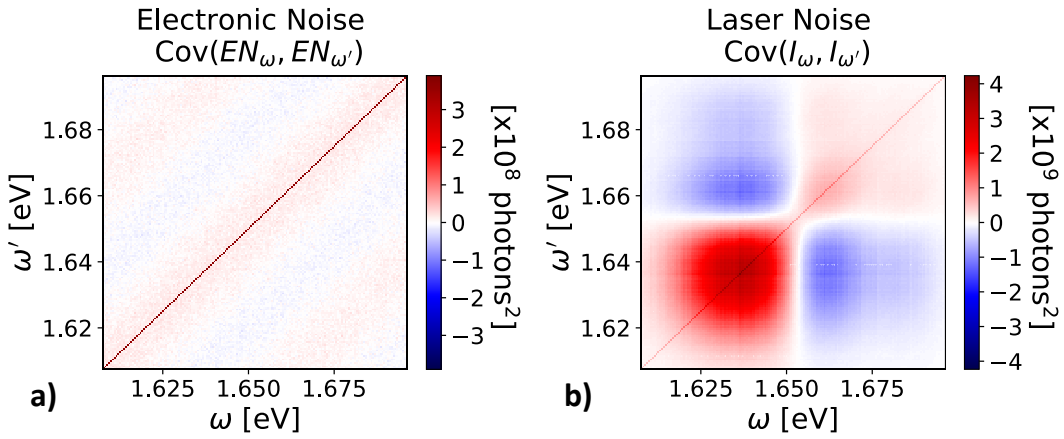

FIGURE 4.8: Setup correlations. a) Array electronic noise covariance map. b) Laser fluctuations covariance map.

4.4.2 Shot Noise correlations

The intrinsic Shot Noise statistics is examined with a balanced heterodyne measurement of the LO light, i.e. the vacuum state. In Fig. 4.9a we show the covariance map obtained with the parallel detection. We observe that thanks to the differential acquisition the laser correlations are removed and the remaining features are the ones due to the detection.

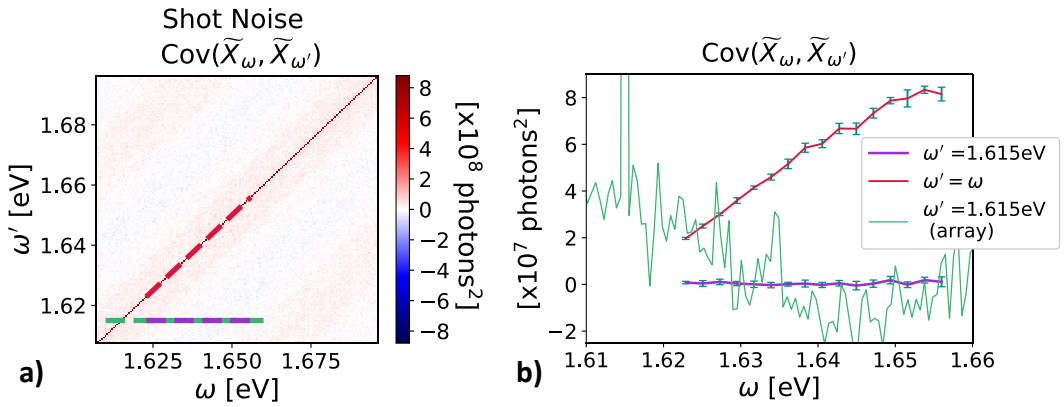

FIGURE 4.9: Shot Noise covariance. a) Covariance map acquired with parallel detection. b) Selected details of covariance map measured with low-noise detection and comparison with array acquisition.

The low-noise configuration is less affected by the detection artifacts and in Fig. 4.9b we present the relative results in comparison with the array map. We display the diagonal trace (red), which is representative of the shot noise variance, and a covariance profile for one fixed frequency component (purple), which is compared to the corresponding data in the array map (green). We see that the measurement is greatly improved ignoring the array response and that no correlation is distinguished out of the low-noise uncertainty. A reference parameter to quantify the signal-to noise ratio is the proportion between standard deviation of covariance and the shot noise variance (diagonal covariance terms), which in our condition is set to 2%.

Chapter 5

Non-gaussian statistical features of pulsed second-harmonic light

The phase space statistics of an optical mode in a coherent state is a two dimensional normal distribution which has the width limited by the Heisenberg principle. When we measure the corresponding mode quadrature, we are evaluating a marginal of such distribution, which is in turn characterized by a gaussian statistics centered around its expectation value. Nevertheless, in the following we highlight that in a pulsed multimode approach this description requires a more careful treatment comprehensive of the absolute phase of the optical field.
We discuss the absolute phase of a pulse introducing the Carrier-Envelope Phase (CEP) description. In general the CEP takes a random value pulse by pulse, while the coherent state is described with reference to a well-defined phase. We note that, despite this fact, in the previous chapter we correctly characterize the employed probe in terms of coherent states, but the equivalence there holds thanks to the locked relative phase between probe and Local Oscillator, which makes heterodyne detection insensitive to the absolute phase. However, the latter condition is not generally true. For instance, the CEP role needs an explicit consideration in the case of frequency conversion experiments [29], where we will indeed reveal a non-gaussian behavior for the quadrature statistics.
In this chapter we investigate the multimode heterodyne detection of Second Harmonic Generation light. The setup capability to collect the optical state statistics is exploited to analyze the emerging non-gaussian features. We perform quantitative tomography reconstruction and discuss the results with reference to phase-randomized coherent states.

5.1 Carrier-Envelope Phase

When dealing with pulsed electric fields it is possible to reference the absolute phase of the optical pulse introducing the Carrier-Envelope Phase (CEP) [30].
The temporal dependence of the field can be described as a fast oscillating *carrier wave*, evolving at frequency ω_c, which is multiplied by a slowly varying *envelope* function $f(t)$.

$$E(t) = f(t)e^{i(\omega_c t+\psi)} + c.c. \tag{5.1}$$

The CEP phase is defined as the difference between the maximum of the envelope and the maximum of the field, which is expressed by the factor ψ.
We depict the time domain representation of the periodic train of pulses in Fig. 5.1a. Successive pulses are generated at a fixed repetition rate from a mode-locked laser. However, they are not pulse to-pulse CEP-stable because a relative phase shift between carrier and envelope occurs. If the shift $\Delta\psi$ is not a multiple of 2π, successive

pulses present a different CEP phase.
The origin of the instability is twofold. On one hand the difference between group and phase velocity due to the propagation in the cavity medium introduces a phase slippage with respect to the envelope. On the other hand, it is not constant, due to the unavoidable mechanical nanometric instability of the cavity parameters, which also adds a certain degree of randomness to the phase jump.

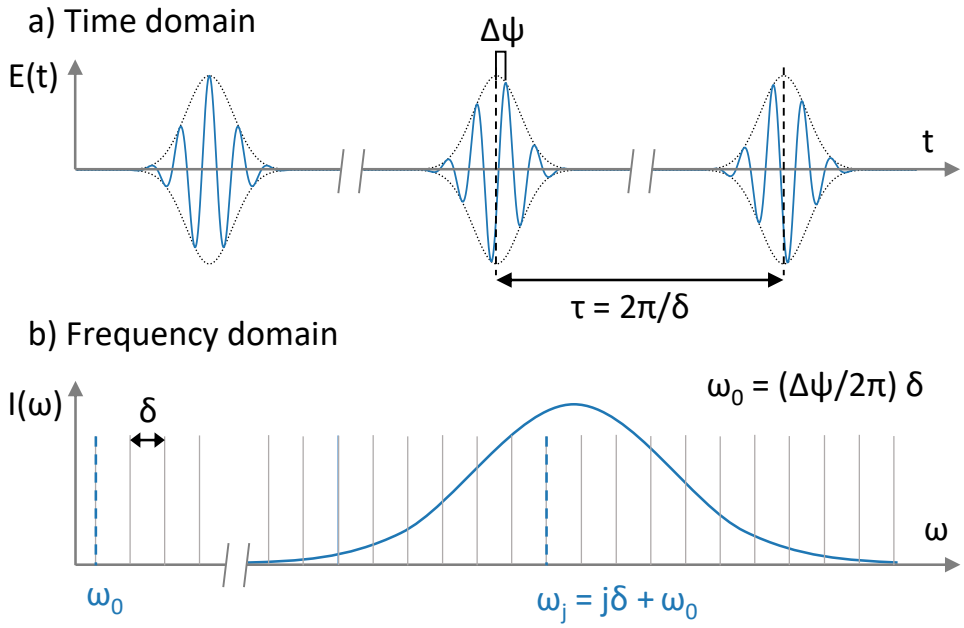

FIGURE 5.1: Carrier-Envelope Phase. a) Time domain representation. The absolute phase of the electric field is characterized as the difference between the maximum of the envelope and the maximum of the field. In general the CEP phase changes pulse-to-pulse. Successive pulse are periodically separated by a period τ (rep.rate δ). b) Pulse spectrum in the frequency domain. The frequency modes of the field are spaced by the repetition rate δ and the CEP instability determines the frequency offset ω_0.

Since we are dealing with a periodic sequence of pulses, it is insightful to analyze them also in the frequency domain.
The pulse envelope is a periodic function such that $f(t+\tau) = f(t)$. Conversely, the carrier is not in general the same after the interval τ between two pulses. If we label the repetition rate as $\delta = 2\pi/\tau$, we indeed have that the carrier frequency is not always an integer multiple of δ but it can present a frequency offset $\omega_0 < \delta$.

$$\omega_c = n_c\delta + \omega_0 \tag{5.2}$$

We can exploit the latter expression to rewrite the field separating the factors with periodicity τ from the one accounting for the CEP shift.

$$E(t) = (f(t)e^{in_c\delta t})e^{i\omega_0 t} + c.c. = \tilde{f}(t)e^{i\omega_0 t} + c.c. \tag{5.3}$$

From the previous equation we can define the CEP shift between two subsequent pulses as $\Delta\psi = \omega_0\tau$. This expression signals the link between the CEP time-shift and its representation in the frequency domain. Indeed, the periodic function $\tilde{f}$ can be represented with a Fourier sum of modes spaced by the repetition rate δ, so that

the field reads

$$E(t) = \sum_{j=0}^{\infty} \tilde{f}_j e^{ij\delta t} e^{i\omega_0 t} + c.c. = \sum_{j=0}^{\infty} \tilde{f}_j e^{i(j\delta+\omega_0)t} + c.c. \tag{5.4}$$

Therefore, as shown in Fig. 5.1b we have that the field spectrum is characterized by a multimode comb of modes with frequency

$$\omega_j = j\delta + \omega_0, \quad j \in \mathbb{N}. \tag{5.5}$$

where the offset ω_0 is indicative of the CEP evolution.
As a consequence of this, frequency conversion processes can be sensitive to the CEP offset. For example, the frequency doubling in second harmonic generation

$$\omega_{SHj} = 2\omega_j = j\delta + 2\omega_0 \tag{5.6}$$

implies a doubling of the CEP offset and a change of the absolute phase with respect to the one of the fundamental.

5.2 Heterodyne of the pump second-harmonic

In order to highlight the role of the absolute phase of the field we adapt our pump&probe heterodyne scheme presented in Fig. 3.1 implementing a Second Harmonic Generation (SHG) experiment.
The pump and probe/LO beams employed are produced respectively as Idler and Signal outputs of an Optical Parametric Amplifier. Our OPA is seeded with a white-light continuum generated by the laser fundamental and pumped by the laser second harmonic. With this typology of OPA implementation, as pointed out it in [31], the relative phase between Idler and Signal, i.e. pump and probe, is fixed.

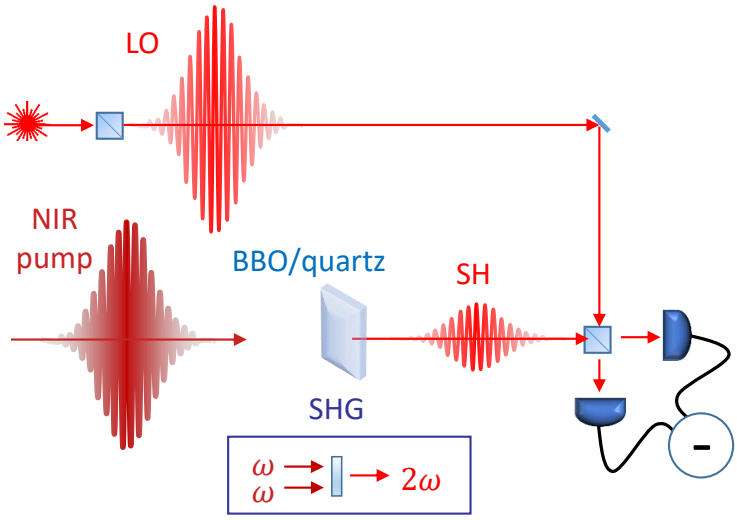

FIGURE 5.2: Heterodyne detection of Second Harmonic Generation. The Near-Infrared pump is frequency converted in a non-linear sample (BBO or quartz) and detected with the visible LO.

We now consider the heterodyne detection experiment. We have that also the phase between probe and LO is locked, being obtained from the same OPA-Signal beam,

and the measured quadrature expresses a well-defined phase. This description complicates if we include in the experiment frequency-conversion processes, like SHG. Actually, in the latter case the absolute phase of the generated light is twice the input one, $\psi_{SH} = 2\psi_i$. To recap, we have LO and pump (Sig/Idl) with the same phase ψ_i and the Second Harmonic (SH) light with phase $2\psi_i$. Therefore, the phase difference between the SH and the reference LO would result in the almost random initial CEP phase $\psi_i = \psi_{SH} - \psi_i$.
Exploiting SHG we can thus design an absolute phase sensitive experiment. In detail, recalling that the pump (Idler) and LO (Signal) have the same absolute phase, we can apply the previous reasoning to perform an heterodyne detection of the pump Second Harmonic (SH). In order to detect an effective interference between SH and LO we implement a configuration (Fig. 5.2) in which the pump SH generated at a non-linear sample (BBO or quartz) is resonant to the LO ($\omega_{LO} = 2\omega_{pump}$). In detail we tune in the range $\omega_{pump} \sim 0.8$ eV = 1550 nm and $\omega_{LO} \sim 1.65$ eV = 750 nm.
We underline that a requirement to get the heterodyne interference is also to match the SH and LO k-vectors. We fulfill it by aligning the pump collinear to the probe. We note that after the sample we dump the pump and select the SH with prisms and low-pass filters, in order to avoid spurious effect on the detector.

5.2.1 Frequency-resolved single pulse measurements

For a first experimental test we employ a Barium Borate (BBO) sample to generate with high efficiency the pump Second Harmonic. We acquire the heterodyne response with the parallel array scheme (described in Fig. 3.7) and thanks to the efficient SHG we show in Fig. 5.3a that we are able to discriminate the interferential modulation already in the single-pulse response. At the same time, the heterodyne signal strongly changes pulse by pulse and the average response on many repetitions is null. This behavior is the result of the completely randomized phase difference between SH and LO due to the laser absolute phase. The average output is indeed the integral on all quadrature phases.
In this framework, then, the empty mean value of the pulse distribution is not

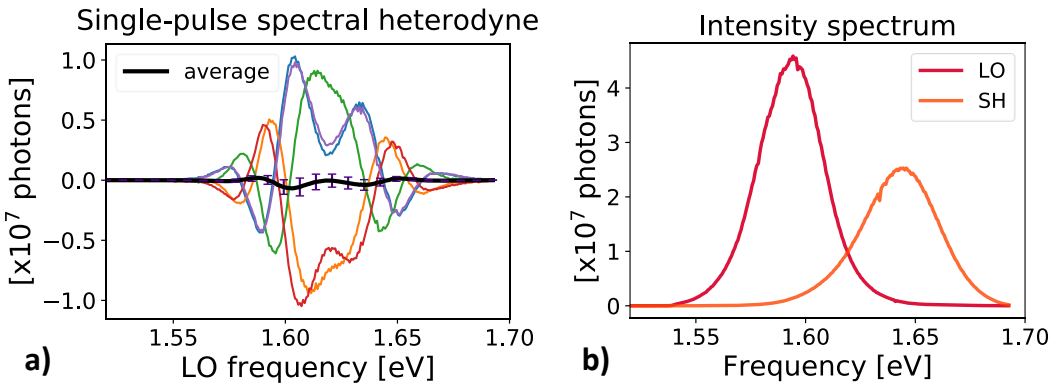

FIGURE 5.3: a) Single pulse heterodyne spectra of SH light generated in BBO. Each pulse presents randomly a different interference fringe pattern, which cancel on the average response. b) Reference intensity spectra of LO and Second Harmonic Generated light.

representative of the state of the system. On the other hand, fundamental information is inferable from the higher order statistics. In the following, we investigate the distribution features proper of the optical state under examination.

5.3 Low-noise study of second-harmonic statistics

The characterization of the pump Second Harmonic heterodyne experiment requires a detailed study of the optical statistics. In order to analyze it quantitatively with reference to the quantum shot noise regime, we adopt the low-noise detection scheme (Fig. 3.8). Since the amount of light detectable in this configuration is limited (the detector response would eventually saturate), we reduce the SHG efficiency by employing a non phase matched quartz sample and detuning the pump-LO resonance. We explore the effects on the pulse distribution as a function of the various degrees of frequency, LO phase and pump intensity.

5.3.1 Frequency response

We start by measuring the dependence on the different spectral components of the multimode configuration.
The first step of our quantitative analysis is the calibration of the LO shot noise for the different spectral components. The observable descriptive of the statistical distribution is the histogram of the values taken by each single-pulse acquisition. We display in Fig. 5.4a the relative map as a function of the LO frequency. We note

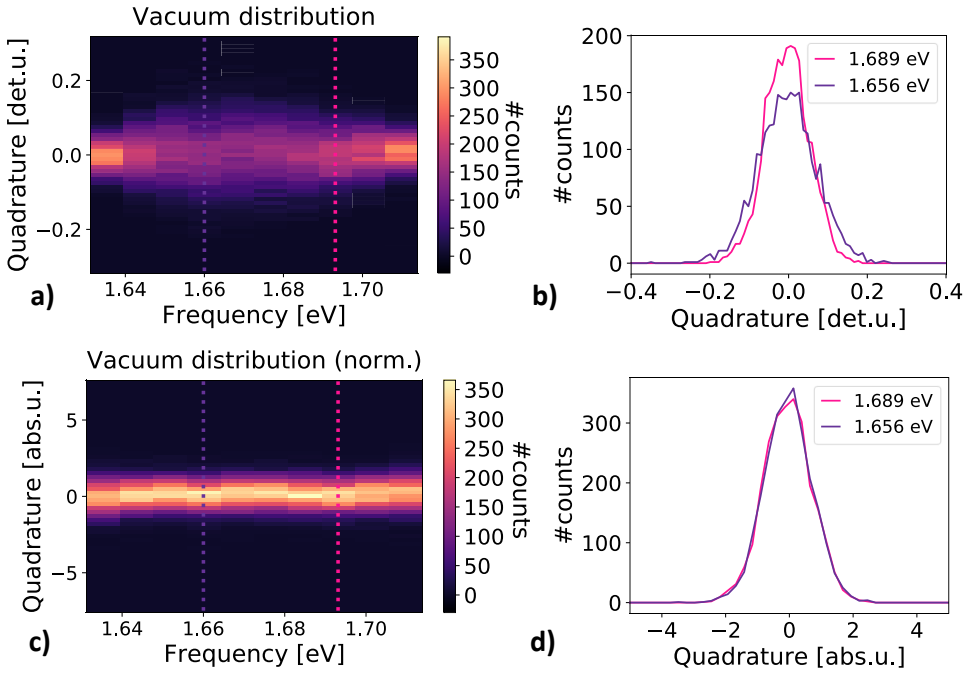

FIGURE 5.4: Histogram representation of the vacuum state gaussian distribution. a) Raw LO shot noise distribution map, b) LO modes have different distribution histograms. c) Normalized vacuum distribution map in absolute phase space units, d) rescaled LO modes have the same histogram distribution.

the expected gaussian shape and the width of the distribution enlarges in agreement with the LO spectrum intensity. We compensate the effect of the different LO strengths normalizing every component to the vacuum response in absolute phase space units. Precisely, we follow the procedure described in section 4.3. We require that the rescaled vacuum quadrature variance reads $\sigma^2_{X^{vac}_{\omega}} = 1/2$ and show the result in Fig. 5.4c.
We now test the SH heterodyne response in absolute units. The measurement output is reported in Fig. 5.5. We observe a bi-modal feature rising on the low energy part of the spectrum, which is the spectral range where the LO is resonant to the tail of the pump generated SH (Fig. 5.5c). Therefore, we deduce that the non-gaussian shape revealed (Fig. 5.5c) is a signature of the generated SH state.

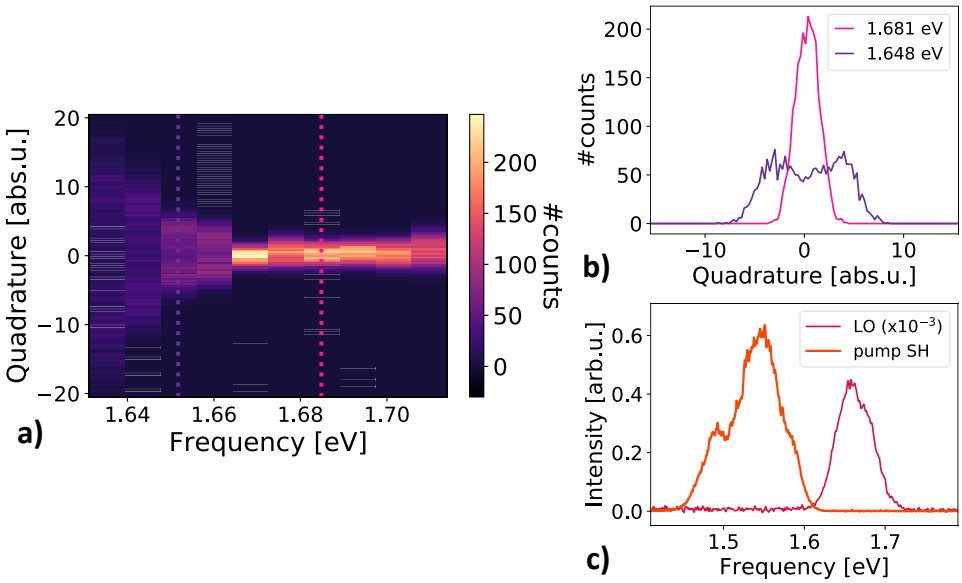

FIGURE 5.5: Frequency-resolved response of Second Harmonic light.
a) Frequency dependent distribution of the heterodyne measurement. b) Distribution histograms at selected frequencies. c) Reference intensity spectra of LO and pump pulses.

5.3.2 LO phase dependence

We now examine the quadrature phase dependence of the SH state. In order to do it, we select a spectral mode at 1.64 eV, where we distinguish the SH bi-modal feature, and scan the LO phase delay. In Fig. 5.6 we see that the SH distribution (b) is phase independent as it is the vacuum one (a).
In addition, we also consider the distribution measured with a probe coherent state together with the SH state. We obtain that the mean value oscillation proper of the coherent state harmonic oscillator (c) is modulating the shift of the bi-modal distribution (d). We can describe this setting as a system formed by a stochastic phase oscillator on top of an harmonic oscillator.

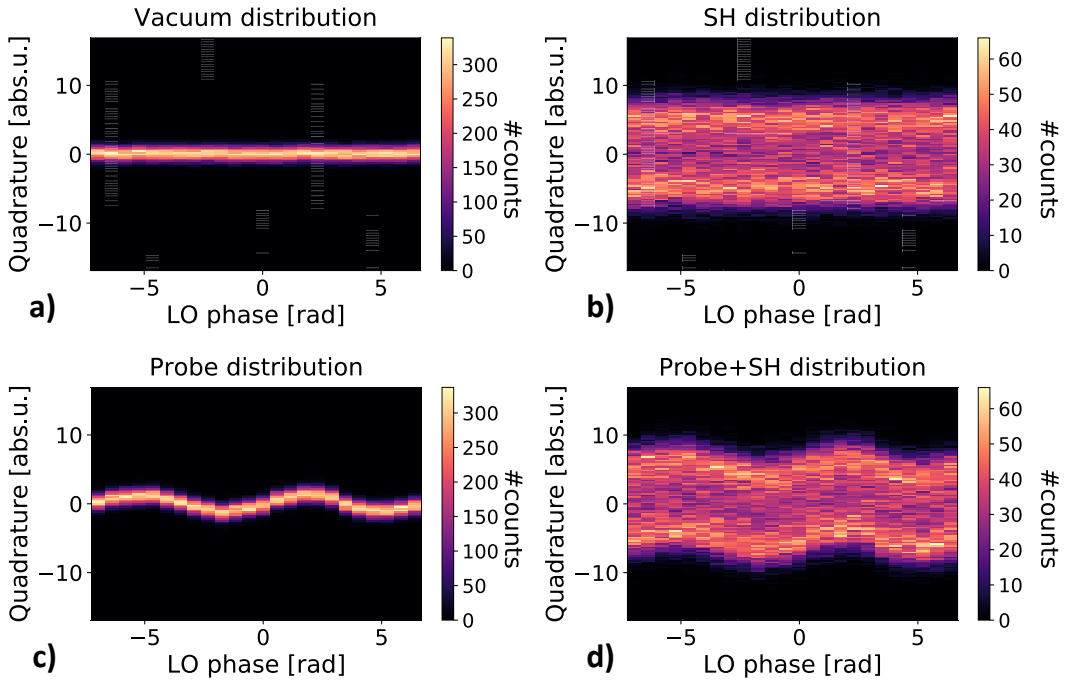

FIGURE 5.6: Phase dependence of the quadrature distribution. a) Vacuum state b) SH state c) Probe state d) Probe+SH.

5.3.3 Pump-intensity dependence

We evaluate the non-gaussian response as a function of the pump intensity to obtain a trend insightful of the considered effect. We clarify in Fig. 5.7a that the separation between the two peaks of the bi-modal distribution is an increasing function of the pump fluence. In particular, in Fig. 5.7b we quantify this dependence calculating the distribution variance with respect to the fluence and we find a good agreement with a third-order polynomial fit.

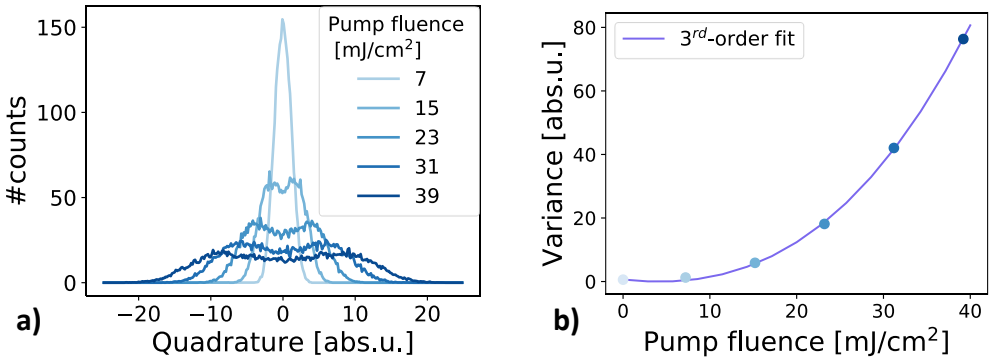

FIGURE 5.7: Pump-intensity dependence of SH distribution. a) Histogram of the SH distribution for different pump fluences. b) Trend of the distribution variance as a function of pump fluence.

5.4 Phase-randomized states

In this section we rationalize the previously collected evidences of a non-gaussian statistics with focus to the absolute phase of the optical state.
We introduce a description in terms of phase-randomized states [32, 33]. This class of states, also known as phase-averaged states (PHAVs), is characterized by a non-gaussian distribution and it is used in quantum communication protocol applications. Their peculiarity is the absence of a well-defined phase in the optical phase space. In particular, as depicted in Fig. 5.8 the Wigner distribution of a phase-averaged coherent state can be formally built rotating isotropically around the origin the coherent state one. Hence, the obtained ring-like distribution describes a completely undetermined phase, while the Poisson statistics of the number operator is preserved.

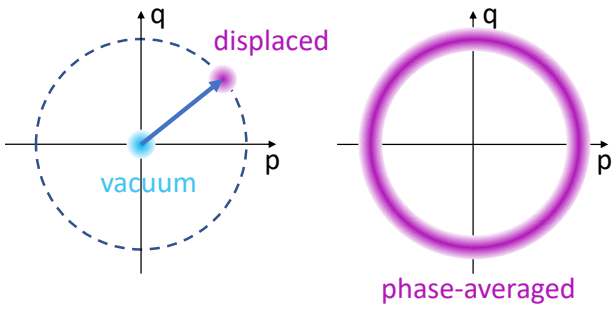

FIGURE 5.8: Phase space distribution of coherent states. The phase-averaged coherent state distribution is obtained integrating the displaced coherent state over all the phase angles.

Taking into account the absolute phase sensitivity of the Second Harmonic heterodyne configuration and the random Carrier-Envelope Phase of the laser pulses, we associate the measured SH light to a phase-randomized state. In order to verify the consistency of our data with this description we perform two analysis.
From the experimental point of view, we exploit the peculiar absolute phase stabilization device of our laser system to test its effect on the output.
In the end, we reconstruct the Wigner function and obtain quantitative estimation of photon number observables by means of optical tomography.

5.4.1 CEP stabilization

The absolute phase of a pulsed field, described with the Carrier-Envelope Phase (CEP), usually takes an almost random value for each repetition in a train of pulses emitted by a mode-locked laser source. This fluctuations result while propagating through a medium owing to the mismatch between the group and phase velocities, which rule the envelope and carrier propagation respectively.
Nevertheless, several schemes have been proposed in order to stabilize the CEP [34, 30]. Our laser source is indeed equipped with a CEP stabilization option (*MENLO Systems XPS800*). With some similarities to the SH experiment under consideration, its operating principle consists in referencing the CEP value with a $f-2f$ interferometer, which realizes the interaction between the laser fundamental and its second harmonic, and then employing a feedback opto-electronics to adjust the absolute phase to the selected value.

Since we claim that the non-gaussian feature observed is due to the randomized absolute phase of the employed laser pulses, it is insightful to test the consequence of the CEP stabilization. In Fig. 5.9 we show the different outputs obtained with random CEP (a) or with active phase stabilization (b). We verify a strong dependence on

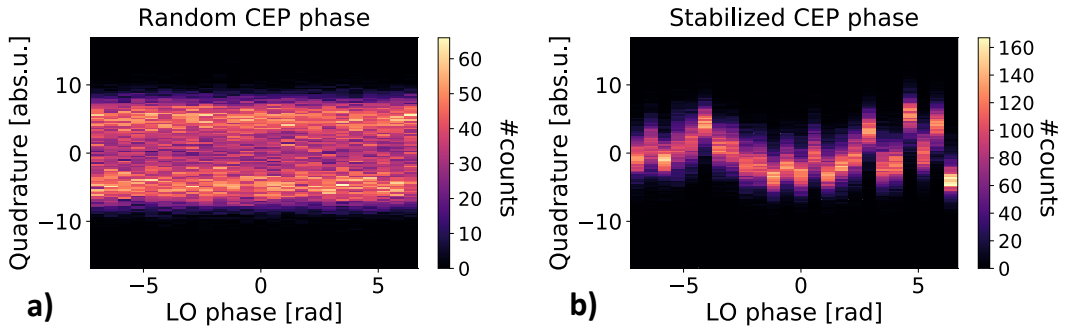

FIGURE 5.9: Carrier-Envelope Phase stabilization of the Second Harmonic Heterodyne. a) CEP not stable. b) CEP stable.

the absolute phase behavior. The bimodal character of the histogram profile disappears and the distribution narrows. The quadrature mean value shift also suggests the appearance of a coherent oscillation. However, the phase stabilization performance is limited (few hundreds of mrad in the ms-scale) and the residual phase noise doesn't permit a clear discrimination of this expected feature.

5.4.2 Optical state tomography

We now resort to optical tomography techniques to characterize the full SH state and check whether it respects the attributes of a phase-randomized system.

Wigner function reconstruction

We reconstruct the Wigner function in the optical phase space for different pump intensities, for a selected LO mode (i.e. 1.64 eV). The results are displayed in Fig. 5.10. In (a) we reference the vacuum state (pump = 0). In (b,c) we analyze the state distribution with increasing pump power, to which corresponds a bigger amount of generated SH light.
We observe the ring-shaped Wigner function proper of phase-averaged states, the radius of which increases with the pump fluence. We also note that the width of the distribution ring enlarges while the SH light rises. We quantify this qualitative survey with pattern tomography analysis. We report the result for the considered Wigner plots in Tab.5.1. They signal a deviation from a coherent state behavior, involving a modification of the photon number statistics in the second harmonic generation process. We discuss the origin of this photon noise modulation in the following by modeling the second harmonic interaction.

Quantitative model for number statistics analysis

The optical tomography of the second harmonic light state indicates a super-poissonian statistics of the number operator ($\sigma_N^2 > N$). In order to discuss this evidence, we model the second harmonic interaction and compare with the experimental data the predicted photon number statistics dependence as a function of the

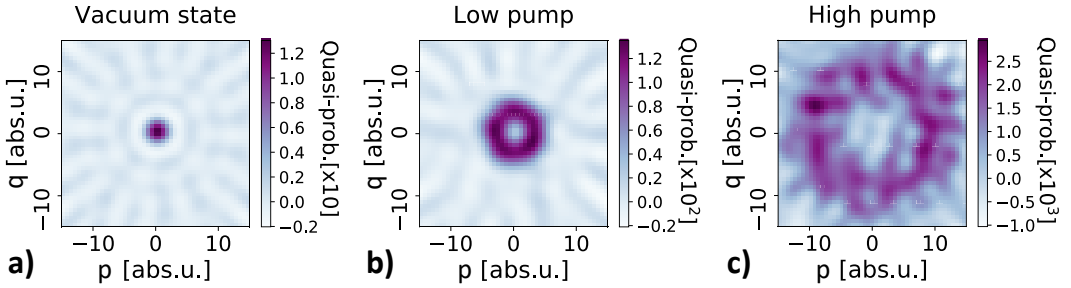

FIGURE 5.10: Wigner function of measured phase randomized state. a) vacuum state b) Phase averaged state (few photons) c) Phase averaged state (many photons).

TABLE 5.1: Result of the pattern tomography reconstruction of the considered Second Harmonic light mode for the photon number operator and its variance.

	N [#photons]	σ_N^2 [#photons^2]
vacuum	0.00 ± 0.01	0.01 ± 0.03
low pump	5.3 ± 0.1	14 ± 2
high pump	41.5 ± 0.7	568 ± 72

pump intensity.
Non-linear interaction processes are described with the high-order terms of the optical susceptibility χ, which rule the polarization field as

$$\mathbf{P} = \chi\mathbf{E} = \chi^{(1)}E + \chi^{(2)}EE + \chi^{(3)}EEE + \chi^{(4)}EEEE + \dots . \tag{5.7}$$

With this we can express the matter-radiation interaction energy and employ it as evolution hamiltonian of the system

$$H = -\mathbf{P} \cdot \mathbf{E}. \tag{5.8}$$

The second harmonic generation is due to the 2^{nd}-order susceptibility $\chi^{(2)}$, and we can represent it with the hamiltonian[1]

$$H^{(SH)} = ig\chi^{(2)}(a^\dagger a^\dagger s - aas^\dagger) \tag{5.9}$$

where we expressed the involved pump and SH electric fields with their ladder operators a and s, respectively, and g is a proportionality coupling factor. Moreover, since the pump field is very intense and negligibly depleted by the low-efficiency of the SH conversion in quartz, we can express it as a classical field α

$$H^{(SH)} = ig\chi^{(2)}|\alpha|^2(s - s^\dagger). \tag{5.10}$$

The evolution of an arbitrary operator O after the interaction time τ can be calculated integrating the action of the hamiltonian for the considered time interval. The

[1]We express only the energy conserving terms associated to $\chi^{(2)}$ and limit the discussion to a single-mode formalism.

result is expressed as a function of the commutator between the observable and the hamiltonian as

$$O(\tau) = O(0) + i\int_0^\tau dt[H, O(t)]. \tag{5.11}$$

The expected number of second harmonic generated photons, calculated perturbatively up to second order in the susceptibility reads

$$N = s^\dagger s(\tau) = s^\dagger s(0) - \tau g\chi^{(2)}|\alpha|^2(s(0) + s^\dagger(0)) + \tau^2(g\chi^{(2)})^2|\alpha|^4. \tag{5.12}$$

Therefore, the average number of the generated SH light calculated in the initial state ($\langle s(0)\rangle = 0$) is

$$\langle N\rangle = +\tau^2(g\chi^{(2)})^2|\alpha|^4 = +\tau^2(g\chi^{(2)})^2 I^2, \tag{5.13}$$

and it is proportional to the square of the pump intensity I.
In Fig. 5.11a we fit the experimental data with the expected quadratic trend. However, we observe the fit agreement is not good and, as also suggested by the third-order fit in Fig. 5.7b, we reason about higher-order contributions.
Since the inversion symmetry is only weakly broken in quartz (i.e. small χ^2) and the pump electric field is very intense due to both ultrashort pulse duration and focusing condition (size = $(50\mu m)^2$), also the quadrupole second harmonic generation gives a relevant contribution. This process is ruled by the 4^{th}-order non-linear susceptibility, with hamiltonian

$$H^{(q-SH)} = ig'\chi^{(4)}((a^\dagger)^3 as - a^3 a^\dagger s^\dagger) = ig'\chi^{(4)}|\alpha|^4(s - s^\dagger) \tag{5.14}$$

where we also considered a classical pump field.
The expected intensity dependence for the quadrupole effect is

$$\langle N^{(4)}\rangle = \tau^2(g'\chi^{(4)})^2 I^4 \tag{5.15}$$

which would overestimate the experimental trend power. However, we need to consider the combined evolution of the hamiltonian $H = H^{(SH)} + H^{(q-SH)}$ which leads to the operator expression

$$N = s^\dagger s - \tau|\alpha|^2(g\chi^{(2)} + g'\chi^{(4)}|\alpha|^2)(s + s^\dagger) + \tau^2|\alpha|^4(g\chi^{(2)} + g'\chi^{(4)}|\alpha|^2)^2. \tag{5.16}$$

and corresponding initial state mean value

$$\langle N\rangle = \tau^2(g\chi^{(2)})^2 I^2 + 2\tau^2 g\chi^{(2)} g'\chi^{(4)} I^3 + \tau^2(g'\chi^{(4)})^2 I^4. \tag{5.17}$$

In Fig. 5.11a we confirm that a fit function of the form in eq. 5.17 correctly matches the measurement data.

We now consider the photon number variance

$$\sigma_N^2 = \langle N^2\rangle - \langle N\rangle^2 \tag{5.18}$$

and calculate its evolution using the dipole+quadrupole number operator in eq. 5.16

$$\sigma_N^2 = \tau^2|\alpha|^4(g\chi^{(2)} + g'\chi^{(4)}|\alpha|^2)^2 = \langle N\rangle. \tag{5.19}$$

The photon number variance equal to the mean number of photons is an attribute of the poissonian statistics, therefore we would expect a coherent statistics for the

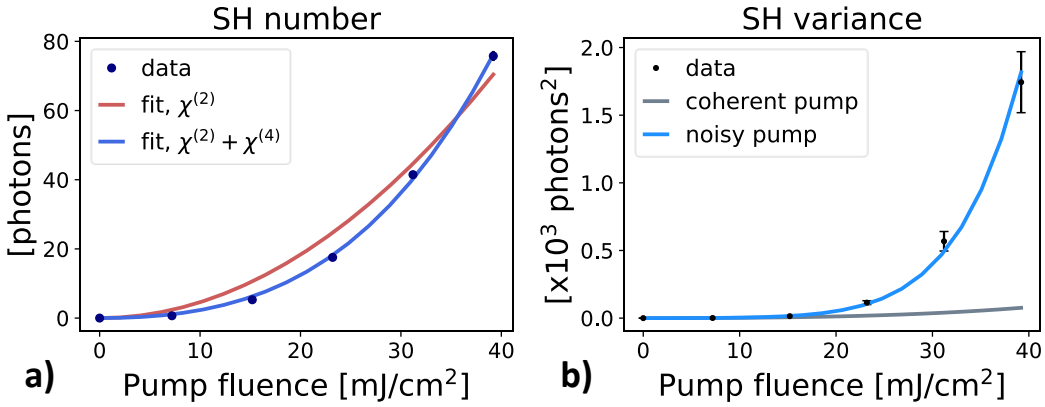

FIGURE 5.11: Quantitative analysis of pump dependent second harmonic number statistics. a) Photon number, fit of experimental data with 2^{nd} and 4^{th}-order non-linear susceptibility models. b) Variance, data comparison with model estimations obtained with mean-value fit parameters.

second harmonic light according to the previous equation. However, we see in Fig. 5.11b that this prediction does not agree with the experiment, where an important amount of excess noise is detected.
We consider this discrepancy due to the classical pump approximation, which neglects the relative statistics. The model is suitable in the case of a coherent pump input, which has negligible signal-to-noise ratio in the high intensity regime. It fails, instead, if other fluctuations (i.e. the laser source noise) are present [35, 36]. In order to take them into account we consider the intensity as a classical random variable and propagate its noise. We sum this contribution to the coherent one and obtain

$$\sigma_N^2 = \left|\frac{dN}{dI}\right|^2 \sigma_I^2 + \langle N \rangle \tag{5.20}$$

which, considering intensity dependent fluctuations ($\sigma_I = kI$), has an intensity dependence of the form

$$\sigma_N^2 = k^2\tau^2 I^2 \left(2(g\chi^{(2)})^2 I + 6g\chi^{(2)} g'\chi^{(4)} I^2 + 4(g'\chi^{(4)})^2 I^3\right)^2 + \langle N \rangle \,. \tag{5.21}$$

We successfully fit this expression in Fig. 5.11b keeping fixed the parameters $g\chi^{(2)}$ and $g'\chi^{(4)}$, which were obtained from the mean value analysis.
In conclusion, we address the excess noise to classical pump fluctuations, likely due to the small fraction of environmental noise which is not eliminated by the balanced differential scheme.

5.5 Multimode correlations

In the previous sections, we considered the statistical properties of each optical mode independently. Hereafter, we focus instead on the correlation between different components which emerge owing to the phase-randomized character of the investigated Second Harmonic light. In detail, we reveal a response which depends on the interference between the SH and LO pulses and we study it shifting the temporal overlap between the two pulses.

Time-dependent interference response

As already described in Fig. 4.1b, changing by several optical cycles the temporal LO overlap modifies the phase relation between the different components, owing to their frequency mismatch. The spectrum of the multimode heterodyne trace is indeed characterized by interference fringes.
We display the single-pulse spectrum[2] measured for SH light at two different LO delays in Fig. 5.12a,b. The fringe frequency is set by the temporal LO delay, it approaches zero at the overlap (when all modes have the same interference condition) while fast oscillations rise moving away. On the other hand, the phase of the modulation is fluctuating as it is ruled by the absolute CEP of the pulse.

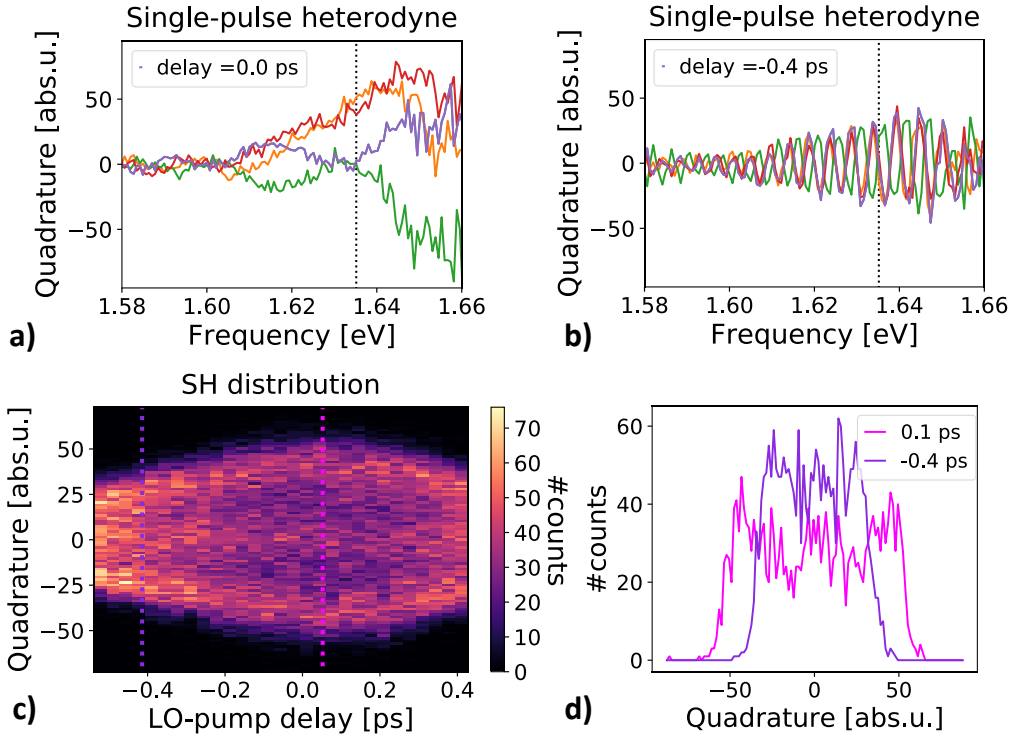

FIGURE 5.12: Second Harmonic interference dependence on the LO-pump overlap. a) Spectrally uniform single-pulse response at the overlap. b) Modulated single-pulse spectral response with separated pulses. c) Time-dependent distribution map. d) Distribution histograms at selected LO delays.

In Fig. 5.12c,d we report the peculiar bimodal distribution of the phase-randomized quadrature for a selected mode, describing its temporal behavior. The SH non-gaussian signal is optimized at the LO overlap, while it decreases on a ps-scale accordingly to the THz-scale resolution of the frequency-resolved detection system.

Time-dependent correlation map

We now study the correlations of the multimode state by calculating the Pearson correlator for the frequency-dependent quadrature as a function of the LO-pump

[2]The experiment is performed in the BBO sample configuration to improve the signal and get a distinguishable single-pulse response.

delay. The Pearson correlation map for two quadrature modes is defined as

$$\rho(X_\omega, X_{\omega'}) = \frac{\mathrm{Cov}[X_\omega, X_{\omega'}]}{\sigma_{X_\omega}\sigma_{X_{\omega'}}} \tag{5.22}$$

where the covariance is normalized by the standard deviations of the considered modes. We show the relative maps for some selected delay in Fig. 5.13 and we reveal a strong and time-dependent response. We rationalize the observed correlation fringes in view of the delay dependent profile of the heterodyne spectrum, which sets a phase relation between modes and gets randomized by the CEP.

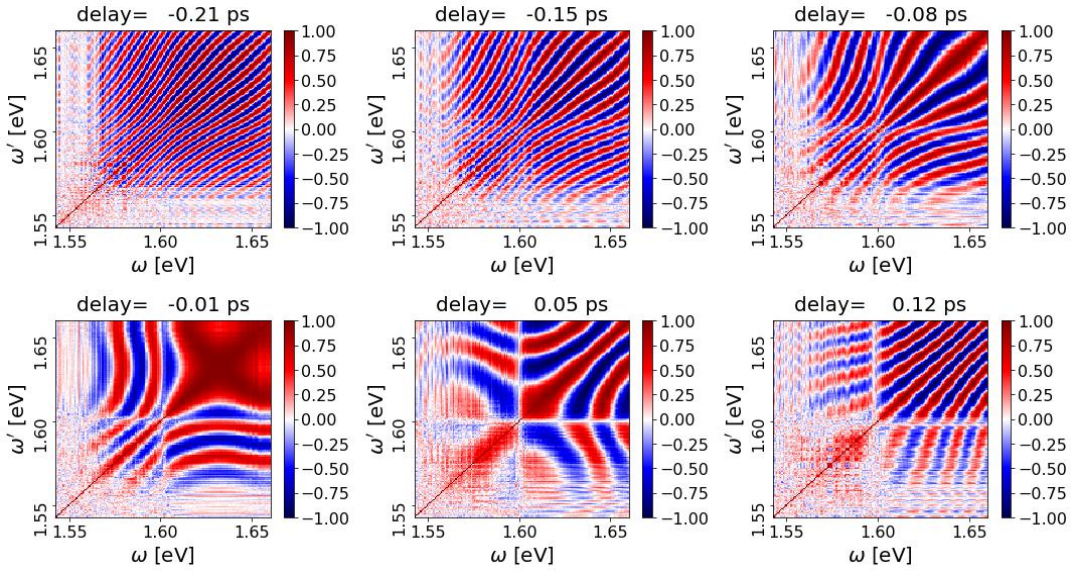

FIGURE 5.13: Second Harmonic correlation map dependent on the temporal LO overlap. Correlation fringes appear as a consequence of the LO overlap dependent spectral modulation.

We note that the correlations are revealed as a consequence of the interference with the LO and are not a feature of the SH state considered alone. Nevertheless, in this phase-randomized framework, especially if the single-pulse response is noisy and unresolvable, this statistical feature can be exploited to retrieve the temporal structure of the pulse. For instance, the analysis of the correlation fringe frequency could supply the information regarding temporal shifts of the pulse in non-equilibrium experiments even if there is no fixed phase relation between probe and LO.

References - part I

[1] U. Fano. "Description of States in Quantum Mechanics by Density Matrix and Operator Techniques". *Rev. Mod. Phys.* 29 (1957).

[2] U. Leonhardt and H. Paul. "Measuring the quantum state of light". *Progress in Quantum Electronics* 19.2 (1995).

[3] A. I. Lvovsky and M. G. Raymer. "Continuous-variable optical quantum-state tomography". *Rev. Mod. Phys.* 81 (2009).

[4] D.-G. Welsch, W. Vogel, and T. Opatrný. "II Homodyne Detection and Quantum-State Reconstruction". Ed. by E. Wolf. Vol. 39. Progress in Optics. Elsevier, 1999.

[5] G. Mauro D'Ariano, M. G. Paris, and M. F. Sacchi. "Quantum Tomography". Ed. by P. W. Hawkes. Vol. 128. Advances in Imaging and Electron Physics. Elsevier, 2003.

[6] J. Johansson, P. Nation, and F. Nori. "QuTiP: An open-source Python framework for the dynamics of open quantum systems". *Computer Physics Communications* 183.8 (2012).

[7] A. I. Lvovsky. "Squeezed Light". *Photonics*. John Wiley & Sons, Ltd, 2015. Chap. 5. ISBN: 9781119009719.

[8] R. Schnabel. "Squeezed states of light and their applications in laser interferometers". *Physics Reports* 684 (2017). Squeezed states of light and their applications in laser interferometers.

[9] M. Esposito, F. Randi, K. Titimbo, G. Kourousias, A. Curri, R. Floreanini, F. Parmigiani, D. Fausti, K. Zimmermann, and F. Benatti. "Quantum interferences reconstruction with low homodyne detection efficiency". *EPJ Quantum Technology* 3 (2016).

[10] M. Esposito, F. Benatti, R. Floreanini, S. Olivares, F. Randi, K. Titimbo, M. Pividori, F. Novelli, F. Cilento, F. Parmigiani, and D. Fausti. "Pulsed homodyne Gaussian quantum tomography with low detection efficiency". *New Journal of Physics* 16.4 (2014).

[11] J. Appel, D. Hoffman, E. Figueroa, and A. I. Lvovsky. "Electronic noise in optical homodyne tomography". *Phys. Rev. A* 75 (2007).

[12] T. Richter. "Determination of field correlation functions from measured quadrature component distributions". *Phys. Rev. A* 53 (1996).

[13] M. G. Raymer and M. Beck. "7 Experimental Quantum State Tomography of Optical Fields and Ultrafast Statistical Sampling". *Quantum State Estimation*. Ed. by M. Paris and J. Řeháček. Berlin, Heidelberg: Springer Berlin Heidelberg, 2004. ISBN: 978-3-540-44481-7.

[14] K. E. Dorfman and S. Mukamel. "Nonlinear spectroscopy with time- and frequency-gated photon counting: A superoperator diagrammatic approach". *Phys. Rev. A* 86 (2012).

[15] E. O. Potma and S. Mukamel. "Theory of Coherent Raman Scattering". *Coherent Raman Scattering Microscopy*. Ed. by J.-X. Cheng and X. S. Xie. CRC Press, 2016.

[16] H. P. Yuen and V. W. S. Chan. "Noise in homodyne and heterodyne detection". *Opt. Lett.* 8.3 (1983).

[17] C. Fabre and N. Treps. "Modes and states in quantum optics". *Rev. Mod. Phys.* 92 (2020).

[18] J. Roslund, R. M. de Araújo, S. Jiang, C. Fabre, and N. Treps. "Wavelength-multiplexed quantum networks with ultrafast frequency combs". *Nature Photonics* 8.2 (2013).

[19] R. Medeiros de Araújo, J. Roslund, Y. Cai, G. Ferrini, C. Fabre, and N. Treps. "Full characterization of a highly multimode entangled state embedded in an optical frequency comb using pulse shaping". *Phys. Rev. A* 89 (2014).

[20] R. I. A. Davis, R. Delbourgo, and P. D. Jarvis. "Covariance, correlation and entanglement". *Journal of Physics A: Mathematical and General* 33.9 (2000).

[21] A. M. Weiner. "Femtosecond pulse shaping using spatial light modulators". *Review of Scientific Instruments* 71.5 (2000).

[22] J. C. Vaughan, T. Hornung, T. Feurer, and K. A. Nelson. "Diffraction-based femtosecond pulse shaping with a two-dimensional spatial light modulator". *Opt. Lett.* 30.3 (2005).

[23] A. Monmayrant, S. Weber, and B. Chatel. "A newcomer's guide to ultrashort pulse shaping and characterization". *Journal of Physics B: Atomic, Molecular and Optical Physics* 43.10 (2010).

[24] N. Forget, V. Crozatier, and T. Oksenhendler. "Pulse-measurement techniques using a single amplitude and phase spectral shaper". *J. Opt. Soc. Am. B* 27.4 (2010).

[25] M. Cooper, C. Söller, and B. J. Smith. "High-stability time-domain balanced homodyne detector for ultrafast optical pulse applications". *Journal of Modern Optics* 60.8 (2013).

[26] T. Gerrits, S. Glancy, and S. W. Nam. "A balanced homodyne detector and local oscillator shaping for measuring optical Schrödinger cat states". *Advanced Photon Counting Techniques V*. Ed. by M. A. Itzler and J. C. Campbell. Vol. 8033. International Society for Optics and Photonics. SPIE, 2011.

[27] Y. Cai, J. Roslund, G. Ferrini, F. Arzani, X. Xu, C. Fabre, and N. Treps. "Multimode entanglement in reconfigurable graph states using optical frequency combs". *Nature Communications* 8.1 (2017).

[28] R. Schmeissner, J. Roslund, C. Fabre, and N. Treps. "Spectral Noise Correlations of an Ultrafast Frequency Comb". *Phys. Rev. Lett.* 113 (2014).

[29] A. de Bohan, P. Antoine, D. B. Milošević, and B. Piraux. "Phase-Dependent Harmonic Emission with Ultrashort Laser Pulses". *Phys. Rev. Lett.* 81 (1998).

[30] D. J. Jones, S. A. Diddams, J. K. Ranka, A. Stentz, R. S. Windeler, J. L. Hall, and S. T. Cundiff. "Carrier-Envelope Phase Control of Femtosecond Mode-Locked Lasers and Direct Optical Frequency Synthesis". *Science* 288.5466 (2000).

[31] A. Baltuška, T. Fuji, and T. Kobayashi. "Controlling the Carrier-Envelope Phase of Ultrashort Light Pulses with Optical Parametric Amplifiers". *Phys. Rev. Lett.* 88 (2002).

[32] A. Allevi, S. Olivares, and M. Bondani. "Manipulating the non-Gaussianity of phase-randomized coherent states". *Opt. Express* 20.22 (2012).

[33] A. Allevi, M. Bondani, P. Marian, T. A. Marian, and S. Olivares. "Characterization of phase-averaged coherent states". *J. Opt. Soc. Am. B* 30.10 (2013).

[34] H. and Telle, G. Steinmeyer, A. Dunlop, J. Stenger, D. Sutter, and U. Keller. "Carrier-envelope offset phase control: A novel concept for absolute optical frequency measurement and ultrashort pulse generation". *Applied Physics B* 69 (1999).

[35] A. Allevi and M. Bondani. "Direct detection of super-thermal photon-number statistics in second-harmonic generation". *Opt. Lett.* 40.13 (2015).

[36] G. Chesi, M. M. Wauters, N. Fasola, A. Allevi, and M. Bondani. "Second Harmonic Revisited: An Analytic Quantum Approach". *Applied Sciences* 9.8 (2019).

Part II

Dissecting coherent phonon dynamics in quartz

Unveiling and controlling the time evolution at the atomic and ultrafast scale of low energy excitations is the key to attain coherently driven new functionalities of materials. The associated Raman response is commonly measured in pump&probe experiments. It relies on the fact that impulsive photo-excitation (i.e. the interaction with light pulses on a timescale shorter than the period of the excitation in the material) triggers coherent non-equilibrium states of low energy excitations, such as phonons [1, 2], magnons [3], or electronic excitations [4, 5, 6], whose time evolution can be subsequently characterized by the ultrashort probe pulse.

The energy transfer between the optical pulse and the material depends on the nature of the examined sample. Transparent systems are the ideal playground to study coherent vibrational excitations. Indeed, in these materials dissipative electron dynamics is small and can be in first approximation neglected. In this condition, the interaction can be described effectively as a direct coupling between the ultrashort pulses and the low-energy modes.

In this framework, the dominating process is dubbed Impulsive Stimulated Raman Scattering (ISRS). ISRS takes place in Raman-active media owing to the interaction between two photon fields whose energy difference matches the energy of a low-energy mode. The overall process results in the creation (Stokes) or annihilation (anti-Stokes) of an excitation in the system.

ISRS has been historically introduced and discussed treating only the high intensity limit where both the coherent vibrational state in matter, which is often dubbed *coherent phonon*[1], and the interacting electric field are described in a classical formalism [7, 8, 9]. However, more recently ISRS processes have emerged as a powerful tool for quantum information and it has been shown that ISRS can be at play even with relatively weak pulses and be used to store/retrieve single photons in/from the elastic field of materials [10, 11] as well as frequency convert single photons through non-linear processes which can occur in probe pulses containing only a few photons [12]. In this context, a growing interest in studying coherent non-equilibrium Raman dynamics with low intensity pulses is emerging.

Time-resolved Multimode Heterodyne Detection is a tool designed to explore the low-energy excitations in the mentioned quantum regime. The following chapters of the thesis are dedicated to characterize the ISRS light-phonon interaction dynamical response mapped on the various optical degrees of freedom available thanks to Multimode Heterodyne.

In Chapter 6 we introduce a theoretical description of ISRS in a fully quantum formalism, suitable for the description of the interaction with low intensity optical probes [13].

Chapter 7 validates the model predictions reporting the results of coherent control experiments in the benchmark α-quartz sample [14]. We highlight the capability of discriminating the spectrally resolved ultrafast dynamics separately for the quadrature amplitude and phase, which turn out to be related to the atomic momentum and position respectively.

In the end, we discuss the statistical features introduced by the non-linear ISRS interaction in Chapter 8. In detail, we focus on the correlations imparted by the exchange of quanta of vibrational excitations among interacting spectral components [15].

[1]The phrase is a synthesis of the more complete expression 'coherent state of the vibrational elastic field'.

Chapter 6

Quantum Model for Impulsive Stimulated Raman Scattering

The interaction between ultrashort light pulses and non-absorbing materials is dominated by Impulsive Stimulated Raman Scattering (ISRS). This effect is fundamental in the description of light-matter energy exchanges, in particular in the excitation of coherent vibrational states.
The description of ISRS in the context of pump&probe experiments is based on effective classical models accounting for the interaction between the phonon and pulsed electromagnetic fields [7, 8, 9]. These are well representative of the physical system in the classical spectroscopy framework, where the number of involved photons is huge and a mean-field representation is appropriate. However, they are no longer suitable when dealing with quantum spectroscopies, which reveal the nature of the interaction at its fundamental quantum scale.
Since the proposed Multimode Heterodyne Detection aims to exploit optical probes with quantum character, we require a suitable tool to account for the attributes specific of this setting. In particular, a quantum mechanical formalism would unfold the statistical information proper of the system state.

In this chapter, we develop a theoretical description of ISRS where, without making any semi-classical approximation, we treat both photon and phonon degrees of freedom at the quantum level [13]. Precisely, we model the system hamiltonian on the basis of the dipole interaction energy. We distinguish two distinct light-matter interaction terms and analyze the relative effects on the phonon and photon degrees of freedom. We achieve this by calculating the evolution of the relevant observables, with focus on the quadrature measured in the Multimode Heterodyne experiment.

6.1 Light-phonon interaction

A dielectric medium is polarized by an electromagnetic wave propagating through it. The components of the polarization field $\mathbf{P}$ are expressed in terms of the impinging electric field $\mathbf{E}$ and the material susceptibility tensor χ:

$$P_\lambda = \epsilon_0 \sum_{\lambda'} \chi_{\lambda\lambda'} E_{\lambda'}, \tag{6.1}$$

where λ is the polarization index and ϵ_0 is the electric permittivity of the vacuum. In our model, we limit the discussion to the case of lossless materials, which are described with an hermitian susceptibility. In particular, we consider that the optical

range of interest is away from absorption regions and we assume the susceptibility is a constant function of the optical energy. One of the fundamental ingredients of the whole discussion is the susceptibility tensor dependence on the lattice deformations, i.e. those caused by excited vibrational modes. Considering tiny displacements out of the equilibrium position, the susceptibility can be perturbatively expanded around its initial value $\boldsymbol{\chi}^{(0)}$ as a function of the lattice normal modes coordinates q_n, also referred to as phonon positions (n labels the mode) [16, 17]:

$$\chi_{\lambda\lambda'}(q_1,\ldots,q_N) = \chi^{(0)}_{\lambda\lambda'} + \sum_n \chi^{(1)}_{\lambda\lambda'}(n) q_n. \tag{6.2}$$

where we defined $\chi^{(1)}_{\lambda\lambda'}(n) := \left(\delta\boldsymbol{\chi}/\delta q_n\right)_{\lambda\lambda'}\Big|_{q_n=0}$ the components of the rank three non-linear susceptibility tensor $\boldsymbol{\chi}^{(1)}$. In order to simplify the notation, in the following we neglect the summation over n and discuss the interaction of a single phonon mode with light. We note that the refractive index depends on the susceptibility, $\boldsymbol{n} = \sqrt{1+\boldsymbol{\chi}}$. Therefore, eq. (6.2) implies a modulation of the material refractive properties as a function of the phonon position operator[1].

In order to study the non-dissipative[2] light-matter interaction we obtain the bulk hamiltonian from the energy density required to establish the polarization $\mathbf{P}$ in a dielectric sample, which is given by [18]

$$\begin{aligned} U(\vec{x},t) &= -\mathbf{P}(\vec{x},t)\cdot\mathbf{E}(\vec{x},t) \\ &= -\epsilon_0 \sum_{\lambda\lambda'} \chi_{\lambda\lambda'} E_{\lambda'}(\vec{x},t) E_\lambda(\vec{x},t). \end{aligned} \tag{6.3}$$

We proceed to quantize the previous expression, where we remind that the susceptibility is phonon modulated as in eq. (6.2). The elastic field q describing the vibration in the crystal, together with its momentum p, and the electric field E_λ polarized along λ can be quantized as follows

$$E_\lambda(\vec{x},t) = i\sum_j \sqrt{\frac{\omega_j}{2V\epsilon_0}} \left(a_{\lambda j} e^{-i(\omega_j t - \vec{k}_j\cdot\vec{x})} - a^\dagger_{\lambda j} e^{i(\omega_j t - \vec{k}_j\cdot\vec{x})}\right), \tag{6.4}$$

$$q(\vec{x},t) = \frac{1}{\sqrt{2m\Omega V_S}} \left(b^\dagger e^{i(\Omega t - \vec{u}\cdot\vec{x})} + b e^{-i(\Omega t - \vec{u}\cdot\vec{x})}\right), \tag{6.5}$$

$$p(\vec{x},t) = i\sqrt{\frac{m\Omega}{2V_S}} \left(b^\dagger e^{i(\Omega t - \vec{u}\cdot\vec{x})} - b e^{-i(\Omega t - \vec{u}\cdot\vec{x})}\right). \tag{6.6}$$

In writing the previous expressions we used $\vec{u}, \vec{k}_j$ for the vibration and electric field wave vectors, respectively, Ω, ω_j are the frequencies of the lattice vibration and electric field, m is the effective mass of the mode, V is the quantization volume of the electric field and V_S is the volume of the sample. The annihilation and creation operators of photonic modes $a_{\lambda j}$ and $a^\dagger_{\lambda j}$ are such that $[a_{\lambda j}, a^\dagger_{\lambda' k}] = \delta_{jk}\delta_{\lambda\lambda'}$, where λ, j

[1] In this discussion we only take into account the refractive effects involving the transmitted light fields. We note that extending the presented formalism to the reflective degrees of freedom also their response can be treated.

[2] We note that in the presence of absorption the imaginary part of the susceptibility would generate the issue of a non-hermitian hamiltonian. Thus, a complete description of the dynamics in dissipative materials would require an extension of the model, following for instance an approach based on open quantum system theory [19].

are the polarization and frequency indices, respectively. In particular, we consider a set of modes with offset frequency ω_0 and spaced by δ: $\omega_j = j\delta + \omega_0, j \in \mathbb{N}$. The phononic degree of freedom are described with b and $b^\dagger$, satisfying the commutation relation $[b, b^\dagger] = 1$.
The interaction Hamiltonian without any approximation is therefore obtained integrating $U(\vec{x})$ over the volume of the sample and reads

$$\mathcal{H}_{\text{int}} = \int_{V_S} \mathrm{d}\vec{x}\epsilon_0 \sum_{\lambda\lambda'} \left[\chi^{(0)}_{\lambda\lambda'} + \sum \chi^{(1)}_{\lambda\lambda'} \frac{1}{\sqrt{2m\Omega V_S}} \left(b^\dagger \mathrm{e}^{i(\Omega t - \vec{u}\cdot\vec{x})} + b\mathrm{e}^{-i(\Omega t - \vec{u}\cdot\vec{x})} \right) \right] \times$$
$$\times \sum_{j\ell} \frac{\sqrt{\omega_j \omega_\ell}}{2V\epsilon_0} \left(a_{\lambda j} \mathrm{e}^{-i(\omega_j t - \vec{k}_j\cdot\vec{x})} - a^\dagger_{\lambda j} \mathrm{e}^{i(\omega_j t - \vec{k}_j\cdot\vec{x})} \right) \left(a_{\lambda'\ell} \mathrm{e}^{-i(\omega_\ell t - \vec{k}_\ell\cdot\vec{x})} - a^\dagger_{\lambda'\ell} \mathrm{e}^{i(\omega_\ell t - \vec{k}_\ell\cdot\vec{x})} \right). \tag{6.7}$$

The effects of the hamiltonian in the system operators are obtained applying the unitary evolution operator $U = e^{-it\mathcal{H}_{int}}$. For a general observable O in the Heisenberg picture it holds

$$O(t) = U^\dagger(t) O U(t) \tag{6.8}$$

which leads to

$$\frac{dO}{dt} = i[H, O] \quad \text{and} \quad O(t) = O(t_0) + i \int_{t_0}^{t} dt'[H, O(t')]. \tag{6.9}$$

Therefore, we have that the integration accounting for a τ lasting interaction reads

$$O(t+\tau) = O(t) + i \int_{t}^{t+\tau} dt'[H(t'), O(t')] \tag{6.10}$$

In order to simplify the spatial and temporal integration, which will account for momentum and energy conservation respectively, we consider that the phonon energy is usually much smaller than the optical frequencies involved. As a consequence of this we can assume $k_j - k_l \simeq u \simeq 0$. Therefore, we can simplify the evolution defining the hamiltonian $H_{int}(t)$ as the sum of the terms which do not vanish through the integrations

$$H_{int} = H_{Ref} + H_{Ram}. \tag{6.11}$$

The first term, which we dub *refractive*, is given by:

$$H_{Ref} = -\frac{V_S}{2V} \sum_{\lambda\lambda', j} \omega_j \chi^{(0)}_{\lambda\lambda'} \left(a^\dagger_{\lambda j}\, a_{\lambda' j} \,+\, a_{\lambda j}\, a^\dagger_{\lambda' j} \right) \tag{6.12}$$

where V_S and V are the sample and quantization volumes and ω_j the photon frequencies indexed by j. H_{Ref} describes the redistribution of photons between the two polarizations which is mediated by the static birefringence ($\chi^{(0)}$).

The second term contributing to the hamiltonian, dubbed *Raman*, is phonon dependent and given by:

$$H_{Ram} = -\frac{\sqrt{V_S}}{2V\sqrt{2m\Omega}} \sum_{\lambda\lambda', j} \omega_j\, \chi^{(1)}_{\lambda\lambda'} \left[\left(a^\dagger_{\lambda j} a_{\lambda' j + \frac{\Omega}{\delta}} \right) b^\dagger + \left(a_{\lambda j} a^\dagger_{\lambda' j + \frac{\Omega}{\delta}} \right) b \right], \tag{6.13}$$

where Ω is the phonon frequency and m its effective mass. The two terms of H_{Ram} represent the Stokes and Anti-Stokes processes. Photons with energy ω_j and

polarization λ are destroyed by $a_{\lambda j}$ and photons of energy $\omega_j \pm \Omega$ and polarization λ' are created by $a^\dagger_{\lambda' j \pm \frac{\Omega}{\delta}}$, together with the emission ($b^\dagger$) and annihilation (b) of a phonon, respectively.

We stress that H_{Ref} and H_{Ram} are representative of the major effects observed in experiments. Importantly, H_{Ref} acts as a beamsplitter relocating photons at a fixed frequency between the two polarizations, that does not imply an effective transfer of energy between the light and the sample. We will thus refer to it as Linear Refractive Modulation (LRM). Conversely, H_{Ram} rules the actual Impulsive Stimulated Raman Scattering (ISRS), which involves the exchange of a quantum of the elastic energy between the probe light pulse and the crystal, resulting in a transfer of spectral weight between different spectral components.
Using this notation, in the following we discuss separately the two different effects, LRM and ISRS, commenting on how they modify the transmitted light and the phonon phase-space.

6.1.1 Linear Refractive Modulation

H_{Ref}, (6.12), describes the redistribution of photons between the two optical polarizations. The $\boldsymbol{\chi}^{(0)}$ equilibrium susceptibility, that is without phonon excitation, describes static refractive effects like birefringence and dichroism. In particular, we consider the case of an isotropic sample with an hermitean susceptibility of the form

$$\boldsymbol{\chi}^{(0)} = \begin{pmatrix} u & -i|w|e^{i\xi} \\ i|w|e^{-i\xi} & u \end{pmatrix} \tag{6.14}$$

where $|w|$ and ξ quantify respectively the polarization rotation and ellipticity induced in a linearly polarized input beam.
The phononic degrees of freedom are not affected by the action of H_{Ref}. Concerning the optical ones, the induced evolution by LRM can be calculated as

$$a_{\lambda j}(\tau) = \sum_{\lambda'} \exp\left(i\tau \frac{V_S}{2V}\omega_j \boldsymbol{\chi}^{(0)}\right)_{\lambda\lambda'} a_{\lambda' j}(0) \tag{6.15}$$

with

$$\exp\left(is\boldsymbol{\chi}^{(0)}\right)_{\lambda\lambda'} = \exp(isu)\begin{pmatrix} \cos(s|w|) & +e^{i\xi}\sin(s|w|) \\ -e^{-i\xi}\sin(s|w|) & \cos(s|w|) \end{pmatrix}. \tag{6.16}$$

The quadrature reads accordingly

$$\begin{aligned} X_{\lambda j}(\tau,\phi) =& \frac{1}{\sqrt{2}} a_{\lambda j}(\tau) e^{-i(\omega_j t+\phi)} + c.c. = \\ =& \cos\left(\tau\frac{V_S}{V}\omega_j|w|\right) X_{\lambda j}\left(0, \phi - \tau\frac{V_S}{V}\omega_j u\right) \\ & \pm \sin\left(\tau\frac{V_S}{V}\omega_j|w|\right) X_{\lambda' j}\left(0, \phi - \tau\frac{V_S}{V}\omega_j u \pm \xi\right) \end{aligned} \tag{6.17}$$

From the latter equation we can appreciate the role of the factor $|w|$ in ruling the quadrature amplitude by mean of the polarization rotation process, and also the effect of the factors u and ξ in controlling the field phase during the propagation through the sample.

In addition, the intensity measured after the LRM interaction can be expressed as

$$I_{\lambda j}(\tau) = a^{\dagger}_{\lambda j} a_{\lambda j}(\tau) = \cos^2\left(\tau \frac{V_S}{V}\omega_j |w|\right) I_{\lambda j}(0) + \sin^2\left(\tau \frac{V_S}{V}\omega_j |w|\right) I_{\lambda' j}(0) \\ \pm \sin\left(\tau \frac{V_S}{V}\omega_j |w|\right) \cos\left(\tau \frac{V_S}{V}\omega_j |w|\right) (a^{\dagger}_{\lambda} a_{\lambda'} e^{\mp i\xi} + a^{\dagger}_{\lambda'} a_{\lambda} e^{\pm i\xi}). \tag{6.18}$$

6.1.2 Impulsive Stimulated Raman Scattering

The energy exchange in the sample is modeled by the Raman Hamiltonian, H_{Ram} (6.13). The phonon related non-linear susceptibility coefficients $\chi^{(1)}_{\lambda\lambda'}$ are assumed real, such that $\chi^{(1)}_{\lambda\lambda'} = \chi^{(1)}_{\lambda'\lambda}$, and small in absolute value, so they represent a perturbative modification of the equilibrium tensor. Unlike the LRM hamiltonian which is solved exactly, we indeed exploit a perturbative approach to perform the ISRS calculations. For a general observable we obtain its evolution up to second order in the interaction parameter $\tau\chi^{(1)}$ with

$$O(\tau) = O(0) + i\tau[H_{Ram}, O(0)] - \frac{\tau^2}{2}[H_{Ram}, [H_{Ram}, O(0)]]. \tag{6.19}$$

The evolution of the phonon operator b reads

$$b(\tau) = b(0) + i\frac{\tau\sqrt{V_S}}{2V\sqrt{2m\Omega}} g, \tag{6.20}$$
$$\text{where} \quad g = \sum_{\lambda\lambda', j} \chi^{(1)}_{\lambda\lambda'}\, \omega_j\, a^{\dagger}_{\lambda j} a_{\lambda' j + \frac{\Omega}{\delta}},$$

which in turn gives the mean values of the phonon phase-space variables position q and momentum p, modified with respect to a generic phonon initial state as

$$\begin{cases} \langle q(\tau)\rangle = \langle q(0)\rangle\,, \\ \langle p(\tau)\rangle = \langle p(0)\rangle + \frac{\tau}{2V}\gamma, \end{cases} \tag{6.21}$$
$$\text{with} \quad \gamma = \langle g\rangle = \textstyle\sum_{\lambda\lambda', j} \chi^{(1)}_{\lambda\lambda'}\, \omega_j\, |\alpha_{\lambda j}||\alpha_{\lambda' j + \frac{\Omega}{\delta}}|,$$

where we assumed coherent states of the radiation with the same spectral phase. This shows that the result of a sudden Raman interaction is a displacement along the momentum axis, as depicted in Fig. 6.1. The squared radius R^2 gives the mean value of the phonon number $N = b^{\dagger} b$, which, to second order in the $\tau\chi^{(1)}$ coupling parameter, results

$$\langle N(\tau)\rangle = \langle N(0)\rangle + \frac{\tau V_S}{2Vm\Omega}\gamma\,\langle p(0)\rangle + \frac{\tau^2 V_S}{8V^2 m\Omega}\,\langle g^{\dagger} g\rangle\,. \tag{6.22}$$

We notice that the first order contribution depends on the value of the momentum p before the interaction, while the second order term is proportional to the mean value of the operator $g^{\dagger}g$, which equals γ^2 if light states are classical (coherent states such that $|\alpha|^2 \gg 1$). The formalism is descriptive of both pump and probe interactions. The second order term is usually negligible with respect to the first one unless $\langle p(0)\rangle = 0$. For example, probing the excited phonon relies on the first term, while the pump excitation from thermal equilibrium on the second.
The effects on the phonon degrees of freedom have their counterparts on the photon

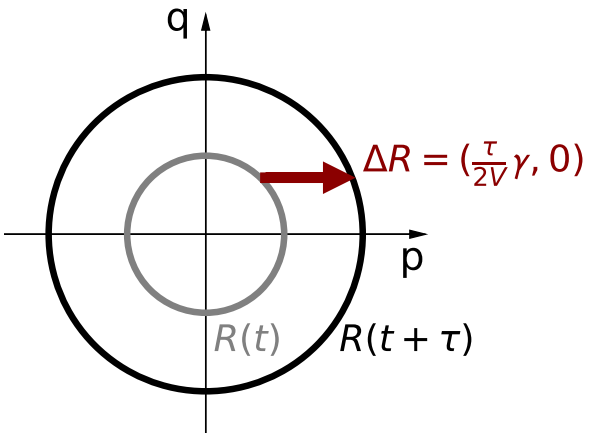

FIGURE 6.1: Phase space representation of the Raman interaction between light and phonon. The circular trajectory is the one followed by the free evolution of the coherent phonon, modeled as an harmonic oscillator. Light-phonon imparts a positive momentum displacement (arrow) modifying the radius of the phonon trajectory.

ones. The intensity of the transmitted light at a certain frequency ω_j and polarization λ, computed as $\langle I_{\lambda j}(\tau)\rangle = \langle a^\dagger_{\lambda j}(\tau)\, a_{\lambda j}(\tau)\rangle$ reads

$$\begin{aligned}\langle I_{\lambda j}(\tau)\rangle = &\langle I_{\lambda j}(0)\rangle \\ &+ \frac{\tau V_S}{2Vm\Omega}\sum_{\lambda'}\chi^{(1)}_{\lambda\lambda'}\omega_j|\alpha_{\lambda j}|\left(|\alpha_{\lambda' j+\frac{\Omega}{\delta}}| - |\alpha_{\lambda' j-\frac{\Omega}{\delta}}|\right)\left(\langle p(0)\rangle + \frac{\tau}{4V}\gamma\right) \\ &+ \tau^2\gamma'_j.\end{aligned} \tag{6.23}$$

In (6.23) the term in $\langle p(0)\rangle$ results from first order contributions and is proportional to the difference in amplitude between the modes corresponding to the frequencies $\omega_j + \Omega$ and $\omega_j - \Omega$. The terms in γ and γ' result from second order interaction. Among them one can recognize a contribution with a structure similar to the first order ($\langle p(0)\rangle$ substituted by γ) and a further one γ'_j which depends on the mean-values of squared phonon operators (see Supplementary Material in [13] for γ' full derivation).
If we examine the quadrature up to first order we have

$$X_{\lambda j}(\tau,\phi) = \frac{1}{\sqrt{2}}\left(a_{\lambda j} + i\frac{\tau\sqrt{V_S}\omega_j}{2V\sqrt{2m\Omega}}\sum_{\lambda'}\chi^{(1)}_{\lambda\lambda'}(a_{\lambda' j+\frac{\Omega}{\delta}}b^\dagger + a^\dagger_{\lambda' j-\frac{\Omega}{\delta}}b)\right)e^{-i(\omega_j t+\phi)} + c.c. \tag{6.24}$$

which for the mean value reads

$$\begin{aligned}\langle X_{\lambda j}(\tau,\phi)\rangle = \langle X_{\lambda j}(0,\phi)\rangle + \frac{\tau V_S\omega_j}{2\sqrt{2}V}\sum_{\lambda'}\chi^{(1)}_{\lambda\lambda'}\Big((|\alpha_{\lambda' j+\frac{\Omega}{\delta}}| - |\alpha_{\lambda' j-\frac{\Omega}{\delta}}|)\cos(\omega_j t+\phi)\frac{\langle p(0)\rangle}{m\Omega} \\ +(|\alpha_{\lambda' j+\frac{\Omega}{\delta}}| + |\alpha_{\lambda' j-\frac{\Omega}{\delta}}|)\sin(\omega_j t+\phi)\,\langle q(0)\rangle\Big).\end{aligned} \tag{6.25}$$

We highlight that in the latter also a position dependent modulation is present. Since the quadrature is defined such that $\langle X(\phi)\rangle = \frac{1}{\sqrt{2}}|\alpha|\cos(\omega t+\phi)$, the momentum

related term describes a modification in the amplitude, in agreement with (6.23). Otherwise, the one controlled by the position is associated to a phase shift of the quadrature. We remind that in the previous expression we considered all the modes with the same spectral phase and we note that in the case of an elliptical polarization ($\varphi_\lambda \neq \varphi_{\lambda'}$) these interpretation should be adapted.

Equipped with this general machinery, we now proceed to study in detail the expected signatures in pump&probe experiments.

6.2 Pump&probe approach

Pump&probe experiments provide standard techniques in time-resolved spectroscopy, whereby a first intense laser pulse (the pump) excites the vibrational degrees of freedom of a sample and a second pulse, less intense, is used to probe non-equilibrium features. By repeating the experiment at different time-delays between pump and probe, one can retrieve information about the phonon dynamics in the sample.

In the following, we describe how the theoretical model presented in the previous section applies in this framework, highlighting the different effects due to subsequent interaction of the pump and the probe pulses. We will consider the pump acting on the phonon equilibrium state at a reference time, and study the non-equilibrium response as a function of the delay time Δt. In particular, we describe two different regimes. Firstly, we take into account the interaction of a second pump pulse as a function of the phase of the vibrational mode, in order to describe the coherent dynamical control of the phonon. We then adapt this description to the probing process, which is the specific case of a weak interacting pulse.

Figure 6.2 shows a sketch of the pump&probe interactions under examination with reference to the phonon phase space description.

6.2.1 Pump interaction

We assume the pump impinging on the sample at equilibrium, where the phonon position and momentum have zero average $\langle q(0)\rangle = \langle p(0)\rangle = 0$ (Fig. 6.2, left). This is the case for instance if the initial state of the vibrational degrees of freedom has a thermal distribution.

The ISRS effect on the intensities of the different frequency components of the pump pulses are here evaluated neglecting the equilibrium LRM. The first order term is null because of $\langle p(0)\rangle = 0$ and we also neglect the term ${\gamma'}_j^{pump}$ because the phonon population is negligible with respect to the photon number. The transmitted pump intensity is given by

$$\begin{aligned}\langle I_{\lambda j}^{pump}(\tau)\rangle_{\Delta t=0} &= \langle I_{\lambda j}^{pump}(0)\rangle \\ &+ \tfrac{\tau^2 V_S}{8V^2 m\Omega}\gamma^{pump}\sum_{\lambda'}\chi^{(1)}_{\lambda\lambda'}\omega_j|\alpha_{\lambda j}^{pump}|\left(|\alpha_{\lambda' j+\frac{\Omega}{\delta}}^{pump}| - |\alpha_{\lambda' j-\frac{\Omega}{\delta}}^{pump}|\right),\end{aligned} \tag{6.26}$$

where $\langle I_{\lambda j}^{pump}(0)\rangle_0$ is the intensity of the spectral components priorly to the interaction and the second term can be interpreted as an effective red-shift of the pulse spectrum. Indeed, assuming the incoming pulse to have a Gaussian spectrum centered in ω_0, equation (6.26) implies that modes with frequency smaller than ω_0 are amplified (because the difference $|\alpha_{\lambda' j+\frac{\Omega}{\delta}}^{pump}| - |\alpha_{\lambda' j-\frac{\Omega}{\delta}}^{pump}|$ is positive), while modes with frequency higher than ω_0 are suppressed. This description rationalizes well the pump red-shift

observed in experiments [7, 20].
Correspondingly, according to (6.21), the phonon system is shifted from the origin of the phase space ($\langle q(0)\rangle_0 = 0, \langle p(0)\rangle_0 = 0$) along the momentum axis to a trajectory of radius

$$R \equiv \langle p(\tau)\rangle_0 = \frac{\tau}{2V}\gamma^{pump}. \tag{6.27}$$

6.2.2 Coherent control

After the impulsive excitation, the vibrational mode evolves in time, neglecting dissipation, along its circular trajectory in the phase space following its free evolution hamiltonian $H_{free} = \Omega b^\dagger b$. The phonon system is indeed represented by a quantum harmonic oscillator. Remarkably, we can analyze the interaction of the radiation with the excited coherent phonon in analogy with a forced harmonic oscillator. Hence, in the following we underline the ISRS capability in controlling coherently the phonon-photon energy exchange at the femtosecond scale.
The phonon time-dependent evolution of the phase space observables at a given time delay (t) from the pump excitation are summarized as:

$$\begin{cases} t < 0, & \langle q(0)\rangle_{\Delta t} = \langle p(0)\rangle_{\Delta t} = 0 \\ t > 0, & \langle q(0)\rangle_{\Delta t} = \frac{R}{m\Omega}\sin(\Omega\Delta t), \quad \langle p(0)\rangle_{\Delta t} = R\cos(\Omega\Delta t). \end{cases} \tag{6.28}$$

With these explicit expression we can evaluate the contributions in (6.22) and (6.23) in order to describe the energy exchange between the phonon and a second optical pulse (#2)

$$\begin{cases} \langle \Delta N\rangle_{\Delta t} = \frac{\tau V_S}{2Vm\Omega}\gamma^{\#2}\langle p\rangle_{\Delta t} + \frac{\tau^2 V_S}{8V^2 m\Omega}(\gamma^{\#2})^2 \\ \langle \Delta I_{\lambda j}\rangle_{\Delta t} = \frac{\tau V_S}{2Vm\Omega}\sum_{\lambda'}\chi^{(1)}_{\lambda\lambda'}\omega_j|\alpha^{\#2}_{\lambda j}|(|\alpha^{\#2}_{\lambda' j+\frac{\Omega}{\delta}}| - |\alpha^{\#2}_{\lambda' j-\frac{\Omega}{\delta}}|)\left(\langle p\rangle_{\Delta t} + \frac{\tau}{4V}\gamma^{\#2}\right) + \tau^2\gamma'^{\#2}_j. \end{cases} \tag{6.29}$$

It results that the amplification of the vibrational mode is favoured when the ISRS process takes place in phase with the phonon momentum, while it is damped when π out of phase. On the other hand, the corresponding amount of energy is respectively taken from/left in the pulse which gets spectrally red/blue shifted.
We note that a second pulse with the suitable intensity in the damped oscillator configuration would even completely quench the coherent oscillation. Although, we underline that such prepared vibrational state could in principle differ by the original empty ground state in its statistical distribution, in particular if the system is characterized by incoherence or inhomogeneity. This framework would thus be an interesting playground where to exploit the statistical sensitivity of Time-resolved Heterodyne Detection.

6.2.3 Probe interaction

The probe interaction with the sample is a peculiar case of coherent control in which we employ a weakly perturbative light pulse. In this setting, indeed, the focus is not set on modifying the attributes of the system, but in monitoring its evolution. In particular, the aim is to map the material attributes on the probe optical degrees of freedom.
We can read these information imprinted in the multimode quadrature $X_{\lambda j}$. We describe in eq. (6.17) and (6.25) the quadrature response relative to the LRM and ISRS effects separately. However, in the actual experiment the two processes need to

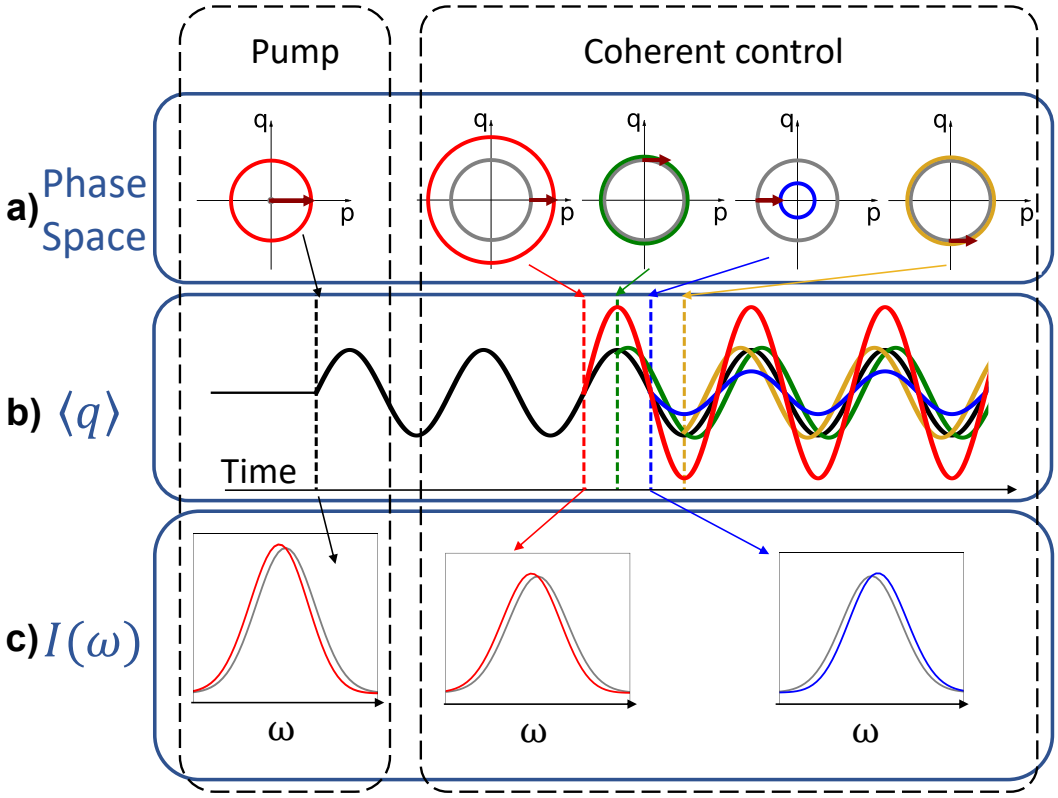

FIGURE 6.2: Coherent control of excitations in the vibrational phase space. a) Pump and probe induced displacements (arrow) describe the effect on the vibrational energy ($\frac{\langle p^2 \rangle}{2m} + \frac{1}{2} m\Omega^2 \langle q^2 \rangle$). Depending on the phase space coordinates at the interaction time the phonon oscillation (b) can be amplified (red) or damped (blue). The corresponding effect on the transmitted pulse spectra (c) is a *red-shift* or *blue-shift*, respectively. The energy exchange is most important at the momentum extremes. At the position extremes instead the oscillation amplitude is minimally modified, while it is experienced a phase shift of the oscillation.

be considered together. In particular, in order to discriminate the symmetry of the non-linear susceptibility tensor $\chi^{(1)}$, a convenient choice for the detection geometry is a reference frame with the polarization analyzer aligned along the main axes of the polarization ellipsis. The latter configuration is described acting on the system with hamiltonian H_{Rot} which is analogous to H_{Ref}, but has tensor structure of the kind

$$\chi^{(0)}_{Rot} = \begin{pmatrix} 0 & +i|w| \\ -i|w| & 0 \end{pmatrix} \tag{6.30}$$

which accounts only for the compensation of the polarization rotation effect, neglecting the dichroism.
If we consider a linearly polarized input state aligned along $\lambda = x$

$$\begin{pmatrix} \langle a_{xj}(0)\rangle \\ \langle a_{yj}(0)\rangle \end{pmatrix} = \begin{pmatrix} |\alpha_j^{probe}| \\ 0 \end{pmatrix}, \tag{6.31}$$

the equilibrium ($H_{Ref} + H_{Rot}$) measured elliptical polarization state has the form

$$\begin{cases} \langle a_{xj}\rangle = k_x(|w|, \xi)|\alpha_j^{probe}| \\ \langle a_{yj}\rangle = ik_y(|w|, \xi)|\alpha_j^{probe}| \end{cases} \tag{6.32}$$

where the amplitudes are a function of the birefringence parameters $|w|, \xi$. Taking into account relatively small refractive effects we can set $k_x \gg k_y$.
The Raman interaction can be considered a perturbation of the latter state due to H_{Ram}. Adapting (6.25) to this elliptic input leads to the phonon dependent modulations

$$\begin{aligned} \langle X_{xj}(\phi)\rangle_{\Delta t} = \sqrt{2}k_x|\alpha_j^{probe}|\cos(\omega_j t + \phi) \\ + \frac{\tau k_x V_S \omega_j}{2\sqrt{2}V}\chi^{(1)}_{xx}\Big((|\alpha^{probe}_{j+\frac{\Omega}{\delta}}| - |\alpha^{probe}_{j-\frac{\Omega}{\delta}}|)\cos(\omega_j t + \phi)\frac{\langle p\rangle_{\Delta t}}{m\Omega} \\ + (|\alpha^{probe}_{j+\frac{\Omega}{\delta}}| + |\alpha^{probe}_{j-\frac{\Omega}{\delta}}|)\sin(\omega_j t + \phi)\langle q\rangle_{\Delta t}\Big). \end{aligned} \tag{6.33}$$

and

$$\begin{aligned} \langle X_{yj}(\phi)\rangle_{\Delta t} = \sqrt{2}k_y|\alpha_j^{probe}|\sin(\omega_j t + \phi) \\ + \frac{\tau k_x V_S \omega_j}{2\sqrt{2}V}\chi^{(1)}_{yx}\Big((|\alpha^{probe}_{j+\frac{\Omega}{\delta}}| - |\alpha^{probe}_{j-\frac{\Omega}{\delta}}|)\cos(\omega_j t + \phi)\frac{\langle p\rangle_{\Delta t}}{m\Omega} \\ + (|\alpha^{probe}_{j+\frac{\Omega}{\delta}}| + |\alpha^{probe}_{j-\frac{\Omega}{\delta}}|)\sin(\omega_j t + \phi)\langle q\rangle_{\Delta t}\Big). \end{aligned} \tag{6.34}$$

where we considered only the dominant contributions in each of the two polarizations.
The measured phonon dynamics is imprinted through the dependence on the phase space observables q and p. We highlight that the $\pi/2$ phase shift between the two polarization components determines the attributes of their dynamical response.
The x-component (eq. (6.33)), parallel to the main polarization, is ruled by the diagonal elements of the susceptibility tensor. The phonon momentum modulation is in phase with the quadrature, thus describes a change in the quadrature amplitude. In

detail, it generates the spectral shift of the spectral content associated with the forcing/damping of the vibrational oscillation. On the other hand, the position related term is most effective in modifying the quadrature phase, which result in a shift of the same sign on all the spectral modes.
Conversely, the orthogonal y-polarization (eq. (6.34)), owing to the elliptical polarization, has a $\pi/2$ shifted equilibrium quadrature which reverses the properties of the detected dynamics. The involved tensor terms are the out-of-diagonal ones which are characteristic of polarization mixing symmetries. Indeed, in the hamiltonians H_{Ref} in eq. (6.12) and H_{Ram} in eq. (6.13), they rule the interaction between modes with orthogonal polarization. The amplitude modulation is ruled by the spectrally uniform term dependent on the phonon position. On the contrary the phase dynamics guided by the phonon momentum has an opposite response on the two spectral sides.
In conclusion, we underline that the analysis of the quadrature dynamics allows us to discriminate the contribution of atomic position and momentum related effects in the coherently oscillating dynamics. The predictions elaborated in this chapter will guide our interpretation of the Time-resolved Heterodyne measurements performed on quartz in the next chapter.

Chapter 7

Pump&probe heterodyne measurements

We report the experimental investigation of coherent vibrational Raman dynamics performed via Time-resolved Heterodyne measurements in the α-quartz sample. Crystalline quartz is an ideal platform wherein to test the prototypical phonon response generated by Impulsive Stimulated Raman Scattering. The sample is indeed endowed with high transparency, photo-resistance and with distinguishable Raman modes. We are therefore in a suitable setting to verify the consistency of the experiment with the quantum ISRS model developed in the previous chapter. The object of the analysis is to address the pump&probe non-equilibrium dynamics associated with the coherent phonon, with focus in discriminating the modulation of the frequency-resolved quadrature phase and amplitude.
Firstly, we introduce the representation of the measurement output and discuss the distinctive features of the general dynamical response in the main polarization component of the probe field. Afterwards, we exploit the polarization geometry to analyze the exhibition of different effects depending on the symmetry of the considered lattice mode. Moreover, we probe the behavior of the explored observables also in the case of coherent control of the vibrational excitation, performing double-pump studies.

7.1 Disentangling amplitude and phase dynamics

Standard pump&probe spectroscopies rely on the measurement of the integrated optical intensity. Remarkably, heterodyne detection, exploiting the interference with the LO, allows us to preserve the field information and disentangle its amplitude and phase contributions.
A Time-resolved Multimode Heterodyne measurement consists in reconstructing the frequency-resolved quadrature of the probe pulse as a function of the delay of the pump pulse. In particular, we are interested in the non-equilibrium modulation of the spectral amplitude and phase.
In Fig. 7.1 we present the multimode quadrature of the employed probe recorded with the parallel array detection scheme (Fig. 3.7). Every quadrature point is obtained acquiring a train of 200 pulse repetitions. We quantify the optical amplitude A and phase φ through a sinusoidal fit of each single-mode quadrature ($A_\omega \cos(\omega t + \varphi_\omega)$, Fig. 7.1a). The results are included in the spectrum in Fig. 7.1c.
The pump&probe output is obtained retrieving the fit parameters for the different pump delays Δt. Precisely, we focus on the evolution of the differential between

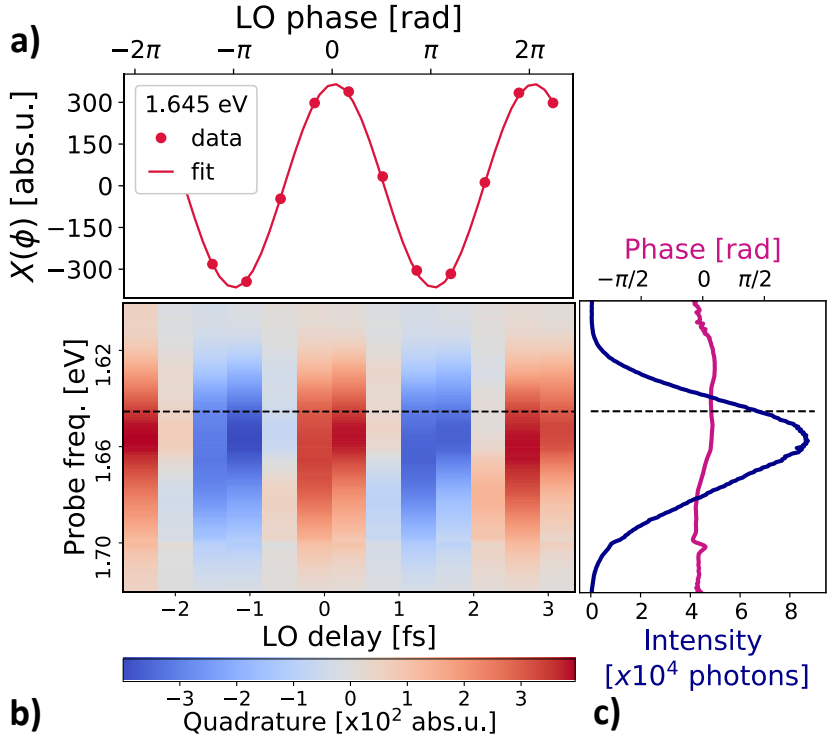

FIGURE 7.1: Equilibrium spectrum of the probe quadrature. The quadrature of each frequency-component (a) is analyzed from the full map acquired with the array detection (b). The result of the fit are collected in the phase and intensity ($I = A^2/2$) spectra in (c).

the perturbed (*pumped*) and the constantly referenced[1] equilibrium (*unpumped*) response. The result are the frequency-delay maps $\Delta A_\omega(\Delta t), \Delta\varphi_\omega(\Delta t)$ in 7.2.
We report a measurement whereby the probe pulse with fluence 0.7 μJ/cm^2 investigates[2] the non-equilibrium dynamics produced by a 30 mJ/cm^2 pump. We observe in the output an oscillating dynamics of the non-equilibrium modulation.
Importantly, the spectral dependence of these features are different comparing the phase and amplitude maps. The oscillation phase is spectrally uniform for the phase, while the two sides of the spectrum have an opposite modulation in the amplitude map.
In Fig. 7.3 we analyze the coherent oscillations revealed. In detail, we plot the results of the interaction in selected spectral ranges. We average the phase modulation along the full spectrum, while we distinguish the contributions of the two opposite sides for the amplitude. We isolate the oscillation frequencies by mean of Fourier Transform analysis (Fig. 7.3b) and we identify some quartz Raman modes [21]. In particular, the main contribution is related to the total-symmetric 6 THz mode.
As suggested by the dotted reference line in Fig. 7.3a, we can appreciate that the amplitude trends of frequencies on opposite sides of the spectrum are in anti-phase to each other, while the phase modulation is $\pi/2$ shifted with respect to them. In order to rationalize the observed dynamics, we refer to the model developed in the previous chapter. In particular, we consider eq. (6.33), describing the detection of the

[1] By means of a chopper blade on the pump beam we alternately acquire the pumped and the reference condition, in order to monitor slow interferometer phase drifts and laser intensity fluctuations.

[2] The probe is amplified with a LO 10^3 times more intense (10^8 photons per pulse).

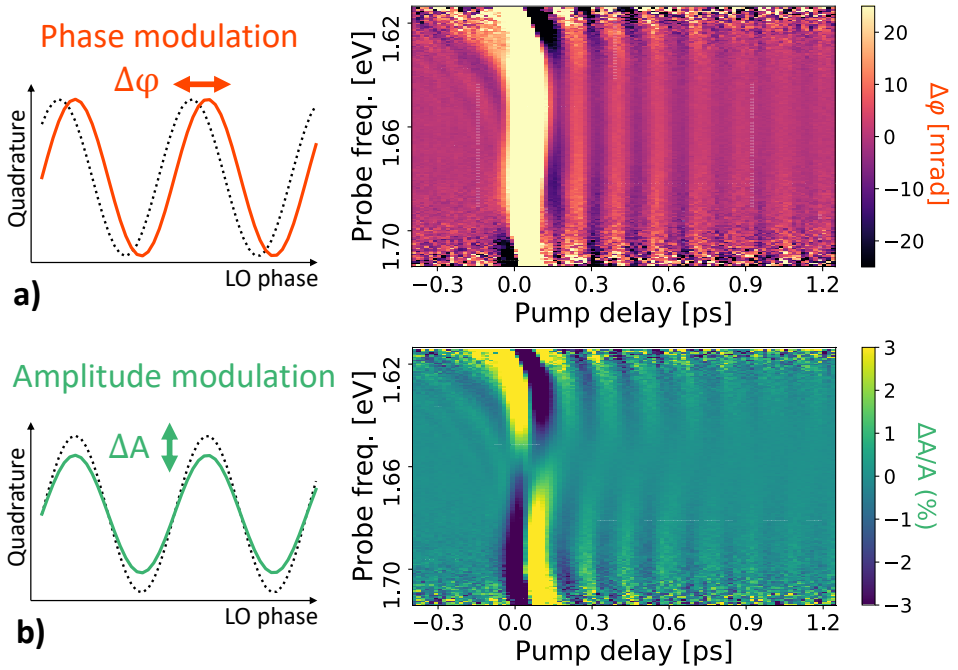

FIGURE 7.2: Pump&probe field dynamics in quartz. The differential of the phase (a) and amplitude (b) fit parameters between the perturbed and equilibrium condition is showed as a function of the pump delay in frequency-time-resolved maps.

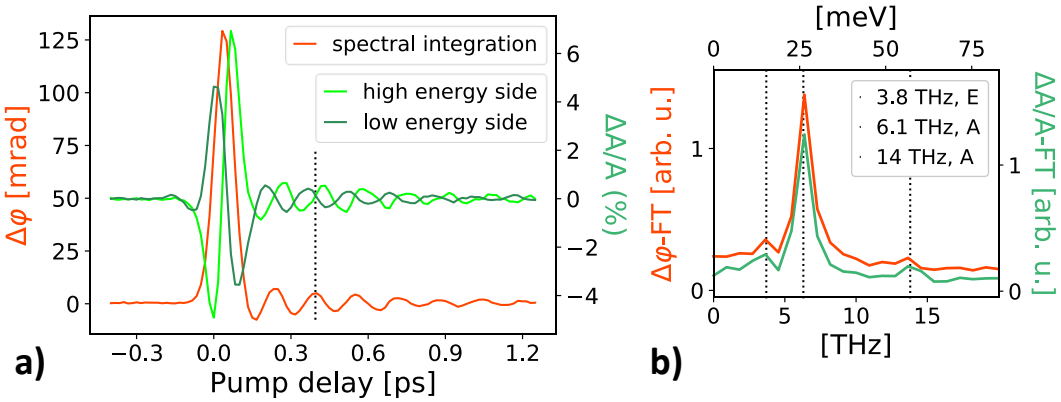

FIGURE 7.3: Analysis of the coherent oscillations in the field dynamics. a) Coherent phonon oscillations obtained averaging the time-response for selected spectral regions (Full spectral range for the phase modulation, separated analysis of the two spectral sides for the amplitude). The dotted line highlights the $\pi/2$ shift between amplitude and phase modulations. b) Average among the probe modes of the Fourier Transform module of the oscillating traces. Three phonon modes (3.8, 6.1 and 14 THz) are identified.

main polarization component, which presents two different modulation terms ruled respectively by the phonon position and momentum.
If the probe interacts with the coherent vibrational state at a time when the atoms have the maximum momentum the Stokes process dominates and high frequency photons are down-converted. On the contrary, when the probe impinges on the sample when the atoms are coherently moving with minimum momentum a partial quench of the atomic motion can be triggered and the probe-phonon interaction is dominated by the Anti-Stokes process; i.e. low frequency photons are up-converted and an effective energy transfer between the elastic field and the probe occurs. Conversely, the time dependence of the phase of the different spectral components exhibits a uniform behavior across the probe spectrum and it is $\pi/2$ shifted with respect to the amplitude oscillation. This indicates that the phase response results from the linear modulation of the sample refractive properties. The real part of the refractive index is dependent on the lattice displacements and the time domain response of the phase is ruled by the coherently evolving atom position.

Hence, we disentangle the amplitude and phase contributions in the field dynamics. We show that they are in general different and descriptive of distinct physical effects. In the next paragraph we study how these properties behave scaling down the probe to the photon number regime dominated by the quantum noise.

Low-noise detection in the quantum probe regime

The quantum nature of the optical probe gets more relevant as we decrease its intensity to a relatively small number of photons. However, the performance of our experiment would be limited by the detection capability to discriminate weak fields and by the intensity related cross-section of the probe interaction effects. Therefore a compromise between acquisition time, signal-to-noise ratio and probe intensity has to be reached.
We discussed in Chapter 4 how the low-noise differential detection scheme is a useful tool to improve the quality of the measurement. Here, we employ the latter in the pump&probe experiment in order to be capable of dealing with a weak quantum probe. We report the relative equilibrium quadrature in Fig. 7.4 acquired with 1000 repetitions per point.
Quantitatively, the experiment is performed with a few hundreds of photons in the probe bandwidth selected by the LO (Fig. 7.4c). The fact that we work with this amount of photons per mode means we can access the shot noise regime, where the probe photon statistics is dominated by quantum fluctuations ($\sigma_N = \sqrt{N}$), which overcome the classical instabilities (which scale linearly on the order of 0.1–1% for our laser source).
Importantly, such a probe intensity is sufficient to trigger a non-equilibrium response able to overcome the noise level. In Fig. 7.5 we show the pump&probe maps obtained in this setting. We see that the magnitude of the phase shift and of the normalized amplitude modulation are comparable with the ones observed in the high intensity regime with a similar pump intensity. Otherwise, in this framework the absolute quantity of scattered light corresponds only to a range of 1-10 photons.
We highlight that the time-domain response of the phase gives a significantly better signal-to-noise ratio than the amplitude. This can be understood by considering that the pump-induced amplitude modulation is a non-linear Raman effect inducing the scattering of a small fraction of photons, while the phase modulation is the result of changes in the material dielectric function which are independent of the probe intensity. This suggests that in the low probe photon number, phase modulation is a

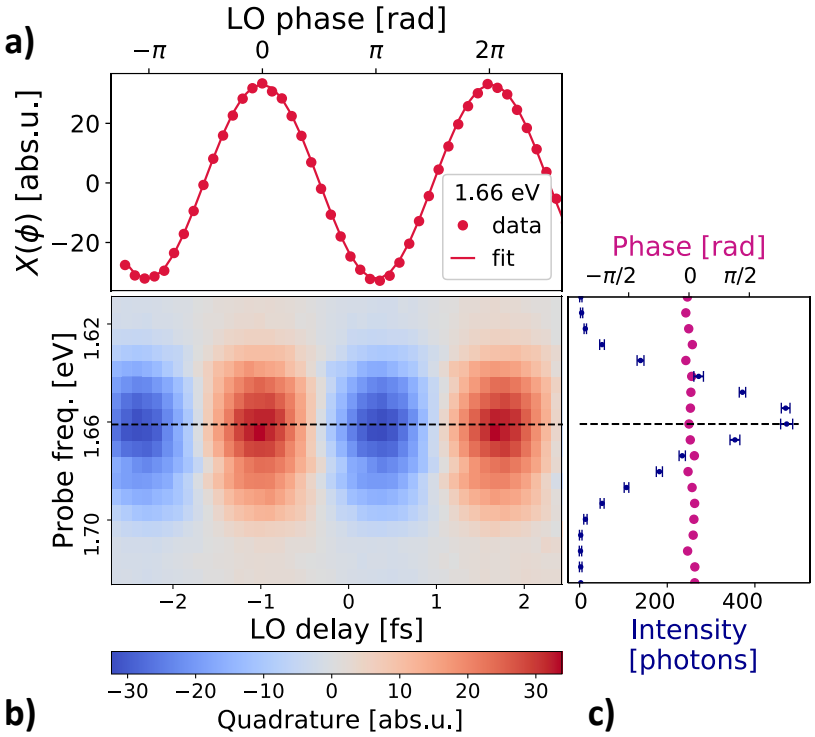

FIGURE 7.4: Equilibrium probe quadrature with low-noise detection in the quantum regime. a) Single-mode quadrature data and fit. b) Spectral quadrature map. c) Spectral phase and intensity retrieved from fit parameters.

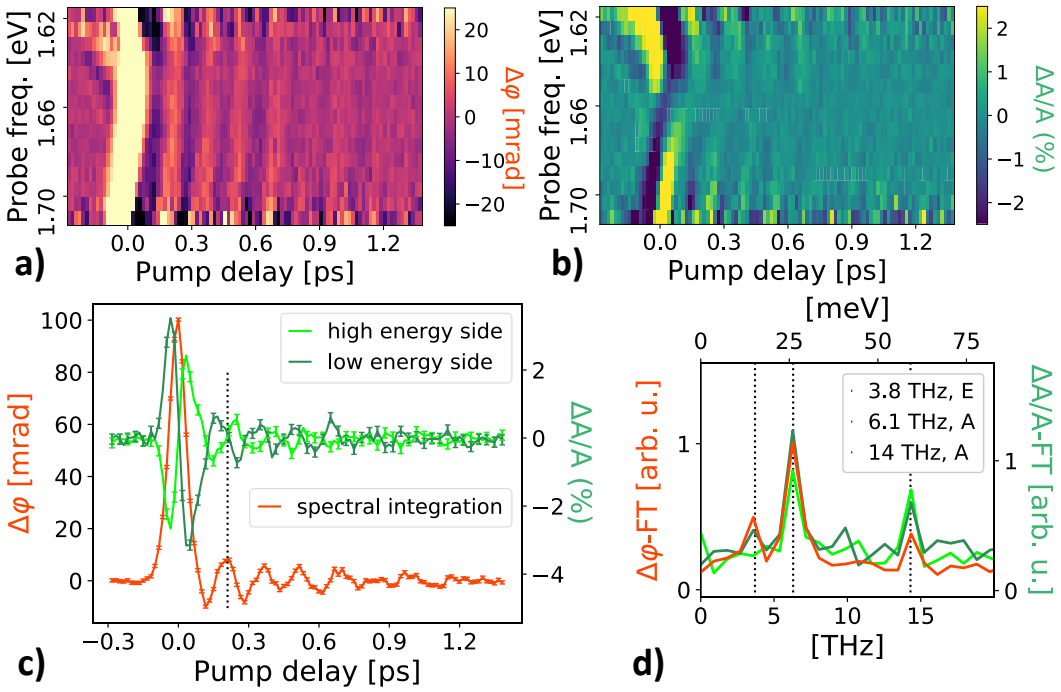

FIGURE 7.5: Pump&probe field dynamics with quantum probe [14]. a) Frequency-resolved pump&probe phase map. b) Spectral amplitude map. c) Details of the measured phonon oscillations and corresponding Fourier spectrum of the relative modes (d).

more suitable observable compared with amplitude or intensity dynamics.

7.2 Symmetry dependent studies

In the measurements reported so far, we detected different phonon modes specific of the quartz sample. Remarkably, these vibrational states also belong to different symmetry classes and, as a consequence of this, they present peculiar properties which rule the light-matter interaction.
In detail, we discuss the case of α-quartz excited along its c-axis [22]. In this setting, three different symmetry classes for the phonon modes come into play. Their different contributions can be selected by a proper combination of the pump-probe polarizations [23]. These three classes correspond to a specific structure of the nonlinear susceptibility tensor. In particular, for the classes called A (totalsymmetric), and the two degenerate E_L (longitudinal) and E_T (transverse), the $(\chi_n^{(1)})_{\lambda\lambda'}$ have the form

$$A = \begin{pmatrix} a & 0 \\ 0 & a \end{pmatrix}, \; E^L = \begin{pmatrix} c_L & 0 \\ 0 & -c_L \end{pmatrix}, \; E^T = \begin{pmatrix} 0 & -c_T \\ -c_T & 0 \end{pmatrix}. \tag{7.1}$$

We can perform a selective detection of the different symmetry classes by varying the angle between the pump and the probe polarization. We consider a reference frame such that the probe is initially polarized along the x axis (as in eq.(7.2)) while the pump is oriented at an angle θ with respect to it

$$\begin{pmatrix} \langle a_{xj}^{pump} \rangle \\ \langle a_{yj}^{pump} \rangle \end{pmatrix} = \begin{pmatrix} |\alpha_j^{pump}| \cos\theta \\ |\alpha_j^{pump}| \sin\theta \end{pmatrix}. \tag{7.2}$$

The effects on the probe after the action of the pump depend on the phase space phonon operators p and q, which in turn are ruled by the radial parameter R introduced in (6.27). In particular, we can explicit the dependence on the pump orientation as

$$\begin{aligned} R_A &= a\eta_{\Omega_A}^{pump}, \\ R_{E^L} &= c_L \cos(2\theta)\, \eta_{\Omega_E}^{pump}, \\ R_{E^T} &= -\, c_T \sin(2\theta)\, \eta_{\Omega_E}^{pump}, \end{aligned} \tag{7.3}$$

where the parameter η_Ω^{pump} has been defined as follows

$$\eta_\Omega^{pump} = \frac{\tau}{2V} \sum_j \omega_j |\alpha_j^{pump}| |\alpha_{j+\frac{\Omega}{\delta}}^{pump}|. \tag{7.4}$$

The results indicate the total-symmetric character of the A modes, while the E have a 4-fold structure.
The contributions of the different vibrational states excited in this framework can be distinguished in the detection. We observed in equations (6.33) and (6.34) that diagonal or out-of-diagonal susceptibility terms are responsible of distinct probe effects. The latter can be separated exploiting the pump orientation dependence. We summarize in Fig. 7.6 the suitable geometry configurations to discriminate the various symmetries.

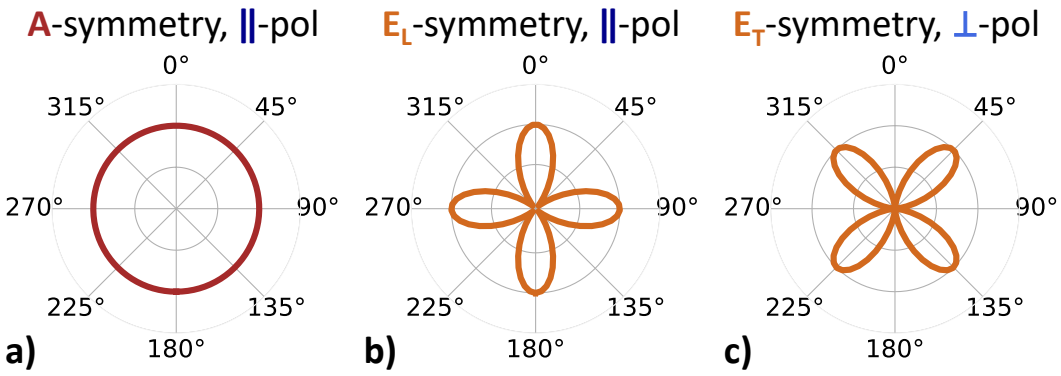

FIGURE 7.6: Phonon symmetries associated to the different detection geometries. Polar plots of the mode visibility for a selected probe component as a function of the pump-probe relative orientation. a) Total symmetric A mode in the main polarization, b) Longitudinal E_L mode in the main polarization, c) Transverse E_T mode in the orthogonal polarization.

In the previous section we reported the effects proper of the diagonal susceptibility terms. In the following we isolate the contribution of the transverse E_T mode responsible of polarization mixing.

7.2.1 E-symmetry selection

The measurement of the orthogonal probe component, described by eq. (6.34), involves the out-of-diagonal susceptibility and predicts a different output with respect to the parallel component one. In particular, the only symmetry class with contributing non-diagonal susceptibility is the E_T. We analyze the associated interaction by selecting it with the suitable geometry. On the basis of Fig. 7.6c, we set the

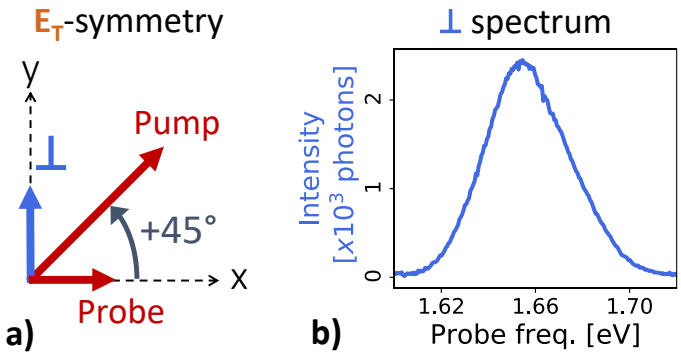

FIGURE 7.7: Transverse E-mode selection. a) Polarization geometry. b) Equilibrium spectrum of probe orthogonal polarization component.

configuration in Fig. 7.7a, where we detect the orthogonal component and orient the pump at 45° with respect to the probe. Moreover, since we have in eq. (7.3) that

$$R_{E^T} = -c_T \sin(2\theta)\, \eta_{\Omega_E}^{pump}, \tag{7.5}$$

we expect the response to be maximized for $|\theta| = 45°$ and having an opposite phonon phase with $\theta = \pm 45°$. Otherwise, the E_T signal disappears continuously

if the pump is parallel or orthogonal to the probe.
In Fig. 7.8 we report the measurement performed with the $+45°$ pump orientation.

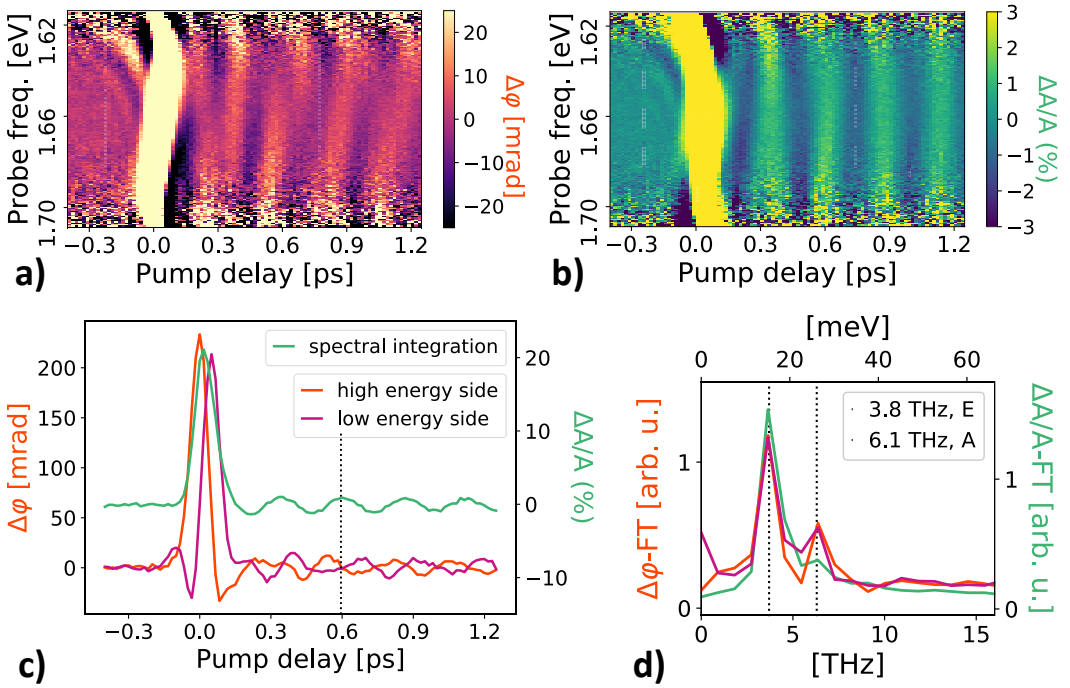

FIGURE 7.8: E-symmetry transverse field dynamics with pump oriented at $\theta = +45°$. a) Frequency-resolved phase modulation. b) Frequency-resolved amplitude modulation. c) Coherent oscillations averaged over selected spectral ranges and relative Fourier-Transform spectra (d). The polarization geometry is sensitive to the 3.8 THz E_T mode, which presents spectral dependent phase dynamics and uniform amplitude response.

We note that the spectral dependence is reversed with respect to the main polarization results in Fig. 7.3. This time, the amplitude modulation is spectrally uniform, while the phase presents a different structure on the two sides of the spectrum. This agrees with the model prediction and it is due to the $\pi/2$ phase shift between the orthogonal components of the elliptical polarization. Indeed, the phonon momentum dependent redistribution of photons is most effective in shifting the quadrature phase, while the amplitude is modulated by the position dependent refractive modulation. From the physical point of view, the phonon is regulating the mixing between the polarization components, which results in a modification of the probe polarization state. For instance, an increasing in the orthogonal amplitude signals a more elliptical character, while a decreasing represents a linearization.
The Fourier analysis of the detected oscillations reveals the selection of the E 4 THz mode with respect to the A one. A residual A-component is still present owing to the higher order effects not expressed in model equation (6.34). In particular, it is the result of the diagonal susceptibility terms interaction on the orthogonal probe component.
We also verify the pump polarization dependence considered in eq. (7.5) presenting the measurement with $\theta = -45°$ in Fig. 7.9. Comparing the amplitude oscillations we observe that the modulation in the two pump orientations have opposite phase as expected.

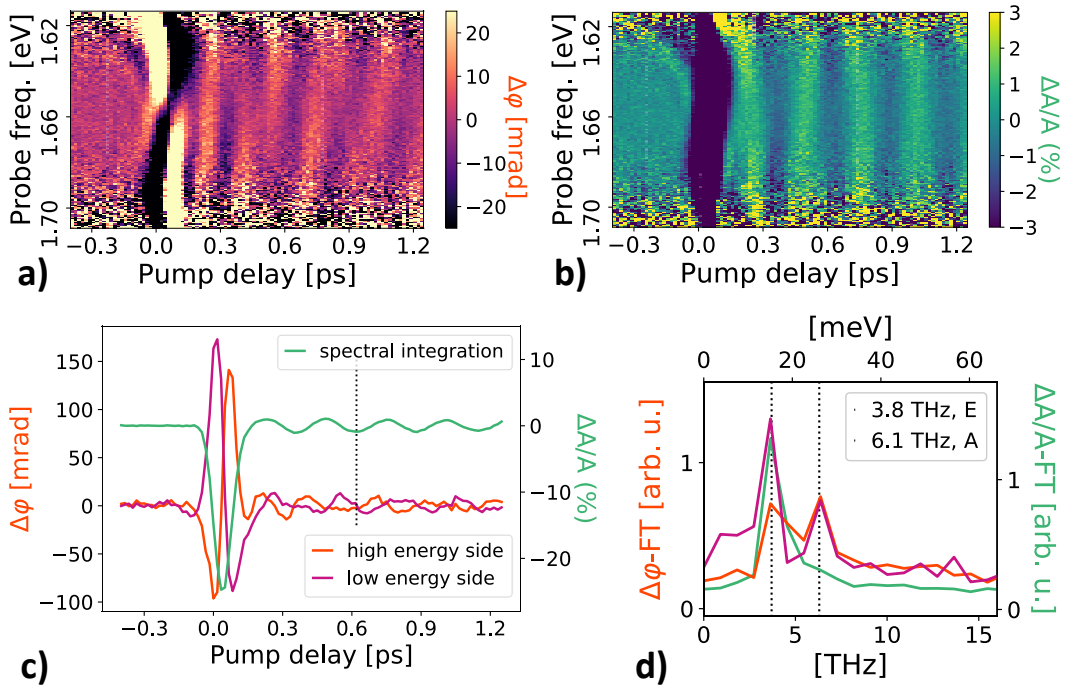

FIGURE 7.9: E-symmetry transverse field dynamics with pump oriented at $\theta = -45°$. a) Frequency-resolved phase modulation. b) Frequency-resolved amplitude modulation. c) Coherent oscillations averaged over selected spectral ranges and relative Fourier-Transform spectra (d). The phase of the oscillations are π-shifted with respect to the case with pump at $\theta = +45°$ (Fig. 7.8).

7.3 Coherent control experiments

In the previous sections, we observed that the result of the probe-sample interaction are dependent on the phonon time-evolution. Importantly, this is not only very useful to monitor the non-equilibrium vibrational excitation, but also a suitable tool to control it on the ultrafast scale. Indeed, Impulsive Stimulated Raman Scattering is able to regulate the energy exchange between the radiation and the elastic field in analogy with a forced/damped harmonic oscillator configuration, as we introduced in Fig. 6.2.
In order to implement the coherent control scheme, we build a double-pump experiment. This kind of pump&probe scheme relies on the tuning of two temporal delays: the coherent control is ruled by the relative delay between the two pumps, while the measurement of the produced state is obtained scanning the probe delay with respect to the pumps.
In the following, we report the probed field dynamics of coherently controlled vibrational states. We perform measurements in the different configurations representative of the phonon mode symmetry.

A-symmetry

Firstly, we investigate the vibrational control in the totalsymmetric condition. The effect of the control pulse is defined by the delay with respect to the first pump, in particular by the momentum of the excited phonon. If we act to force it at the instant of maximum momentum, we sum the intensity of the two pumps. Otherwise,

we subtract them if we maximally dump the phonon excitation at the minimum momentum. A peculiar case is the one in which we can perfectly cancel the vibrational excitation.
In Fig. 7.10 we present the phonon quench experiment. We tune the relative delay to the minimum momentum instant of the totalsymmetric A mode. We also regulate the control pump intensity with an attenuator. We obtain the optimal cancellation of the phonon response with a second pump weaker than the first one. The latter condition occurs because part of the vibrational energy is spontaneously lost due to dissipation during the interval between the pumps. We can observe that setting these conditions the measured non-equilibrium dynamics doesn't show a coherent oscillation after the second pump. There is only a residual signal owing to the non perfect tuning of the pump parameters and to the presence of other phonon modes with different frequencies.

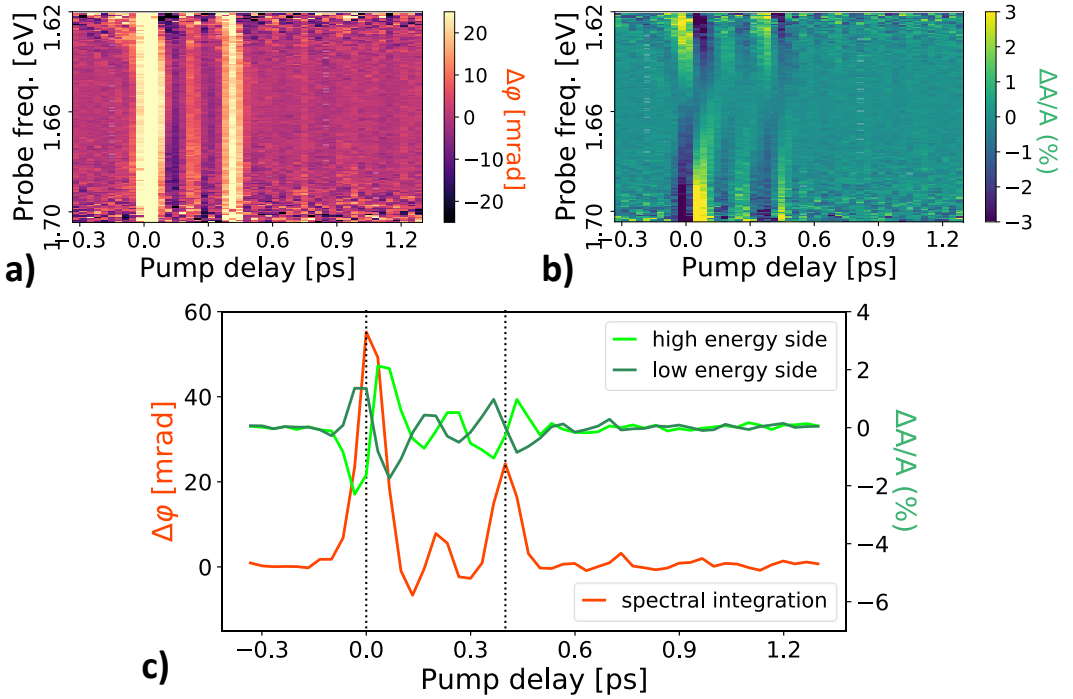

FIGURE 7.10: Example of vibrational coherent control in a double-pump experiment. The A-mode 6 THz phonon excited by the first pump is subsequently quenched by the second pump pulse. The second pump is imparted when the phonon momentum is minimum; the intensity of the second pump is lower than the first in order to account for the phonon dissipation between the two interactions. a) Frequency-resolved phase dynamics. b) Frequency-resolved amplitude dynamics. c) Oscillating profile of selected spectral ranges.

E-symmetry

Previously (Fig. 7.8,7.9), we highlighted that the E_T mode presents a characteristic dynamics in the probe orthogonal polarization due to the associated polarization mixing process. Remarkably, the features of this symmetry class are regulated by the experimental geometry. In particular, we can exploit the polarization dependence for control purposes.

As expressed in eq. (7.5), dealing with the E-symmetry we can change the pump effect orienting its polarization. Therefore, we have another degree of freedom available in the coherent control machinery, in addition to the relative delay between the two pumps.
We consider a coherent control experiment with the two pump of equal intensity but with different polarization orientations: one at $\theta = +45°$ and the other at $\theta = -45°$ with respect to the probe. In this setting, each pump imparts an opposite displacement to the state of the transverse E_T phonon.
The temporal delay between the two pumps is still a crucial parameter in determining the vibrational evolution. Nevertheless, the polarization dependence requires to correct the general interpretation in terms of the phonon momentum. Indeed, the opposite effect of the pumps implies that the oscillation is now quenched with positive momentum and forced with negative one.
In Fig. 7.11 we study the case in which the two pump are separated in time by half of the phonon period (π-shift, minimum momentum) and we report the coherent amplification of the vibrational excitation at 4 THz.

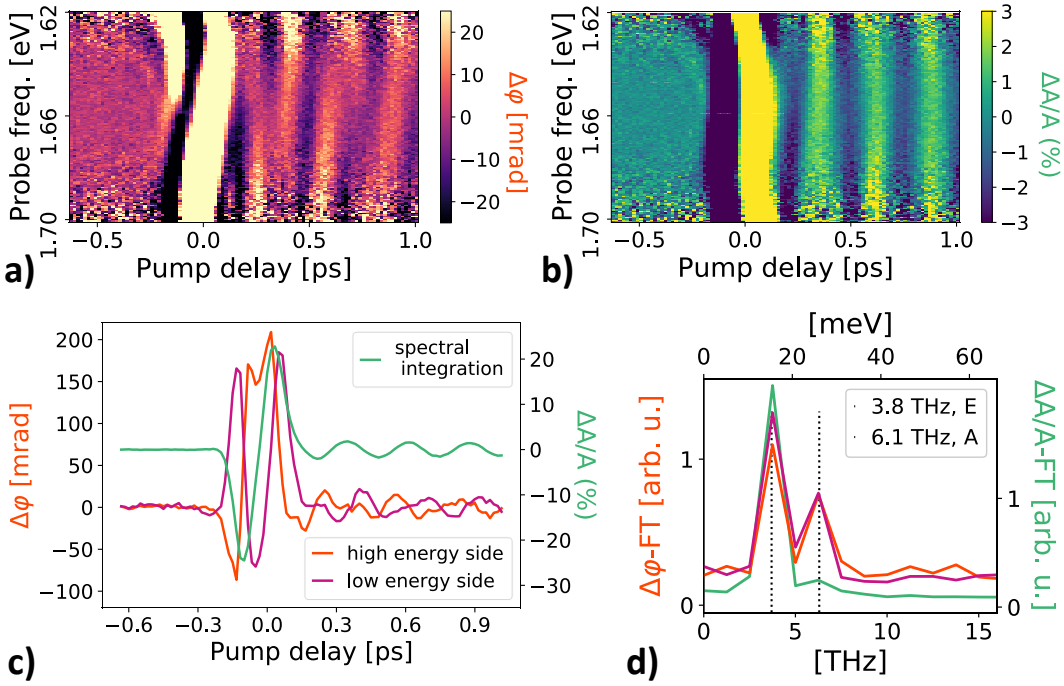

FIGURE 7.11: Double-pump with opposite polarization ($\theta = \pm 45°$) delayed by half phonon period resulting in the amplification of the 4 THz mode. The phonon is forced at the minimum momentum because of the negative displacement induced by the polarization geometry. The response is analyzed in the probe orthogonal component. a) Frequency-resolved phase dynamics. b) Frequency-resolved amplitude dynamics. c) Oscillation profile of selected spectral ranges. d) Fourier-Transform spectra. The main contribution is the geometry selected E_T mode, but also a residual totalsymmetric signal is detected.

Another representative condition is the one involving the quench of the excitation. While in the totalsymmetric analysis in Fig. 7.10 we exploit the control with a subsequent pulse to damp the phonon, thanks to the E-symmetry polarization dependence we can even prevent the excitation to occur.

We show this setting in Fig. 7.12. The two pump pulses with opposite polarization are acting simultaneously on the sample. While the two pump can separately trigger the 4 THz mode, the total result is null. We can observe from the Fourier Spectrum of the non-equilibrium dynamics (Fig. 7.12d) that the 4 THz E-mode signal is absent and the detected dynamics is relative to the 6 THz A component. Indeed, we also distinguish in the maps that the phase dynamics is spectrally uniform and the amplitude one is wiggling, as expected for the totalsymmetric contribution.

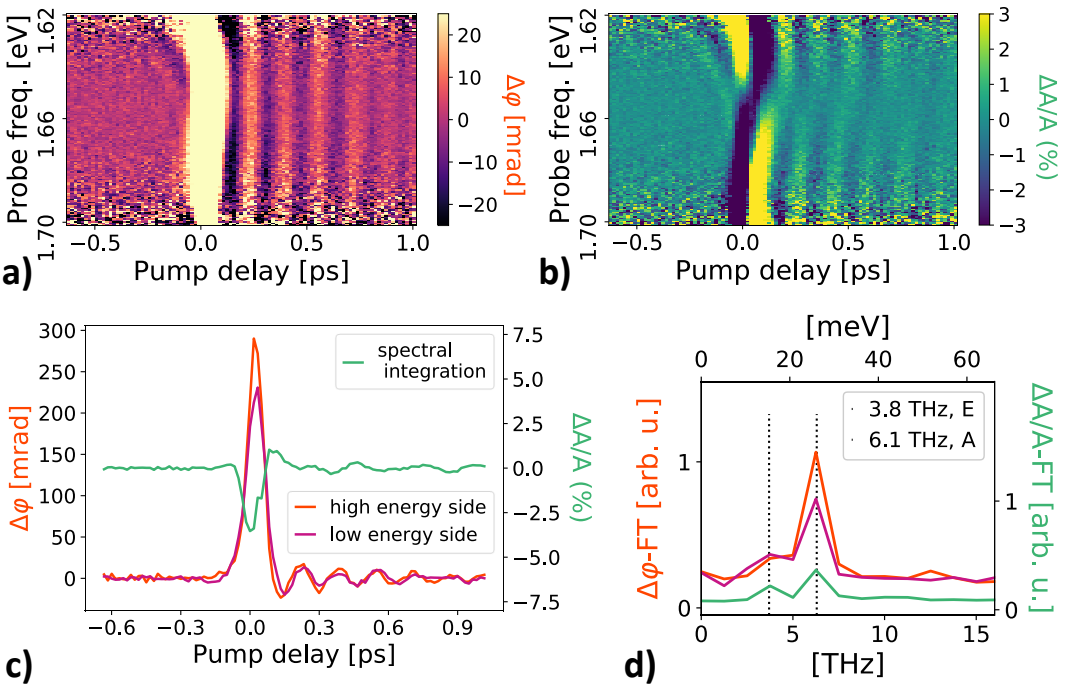

FIGURE 7.12: Double-pump with opposite polarization ($\theta = \pm 45°$) temporally superimposed resulting in the quench of the 4 THz mode. The opposite effect on the E_T mode of the two pumps is canceled if they act together and only the residual totalsymmetric dynamics takes place. The response is analyzed in the probe orthogonal component. a) Frequency-resolved phase dynamics. b) Frequency-resolved amplitude dynamics. c) Oscillation profile of selected spectral ranges. d) Fourier-Transform spectra. The E_T contribution is quenched and the residual A mode is dominating the response.

In conclusion, we demonstrated the capability to control the coherent phonon vibration on the ultrafast scale and to monitor its evolution both on the probe amplitude and phase, where specific responses are distinguishable.
In perspective, we underline that the last examples of coherent quench are interesting to study not only the control of the vibrational excitation, but also a more general superposition of different oscillators. Despite the final state has a zero average response, it represents a non-equilibrium condition which can show a statistics in principle very different from the initial ground state. In quartz these effects are not evident, because the system is well described by a single-oscillator approximation considering the high degree of temporal and spatial coherence of the phonon excitation. Nevertheless, we expect these considerations to be particularly relevant in systems affected by incoherence and inhomogeneity, where the non-equilibrium response is the result of many localized excitations.

Chapter 8

Analysis of ISRS statistical features

The capability to resolve each single-pulse acquisition in our ultrafast experiments allows us to explore the full statistics of the pulses repetitions, which represents a further degree of freedom where information regarding the light-matter interaction can be stored. Moreover, the frequency-resolved measurement of the multimode probe allows us to investigate the presence of statistical correlations between different spectral components.
The typical probe pulse is in a multimode coherent state, where the various frequencies are independent from each other. Interestingly, non-linear interactions can though modify the coherent state and introduce a correlation between different components. For instance, parametric processes as up/down-conversion or four-wave mixing [24, 25] are employed to study the mode entanglement in quantum optics experiments.
In this chapter we highlight that also the Raman interaction, as the one involved in the examined ISRS process, can create spectral correlations between components. In particular, the result is a pair entanglement of the modes whose energy difference matches the phonon frequency, as a consequence of their interaction mediated by the vibrational field.

8.1 Raman mediated multimode correlations

The Raman scattering involves the inelastic interaction between two optical fields together with the emission/annihilation of a low energy excitation (i.e. a phonon) in a Stokes/Anti-Stokes process. This action is well-described by the Raman hamiltonian obtained in (6.13)

$$H_{Ram} = -\frac{\sqrt{V_S}}{2V\sqrt{2m\Omega}} \sum_{\lambda\lambda',j} \omega_j \chi^{(1)}_{\lambda\lambda'} \left[\left(a^\dagger_{\lambda j} a_{\lambda' j+\frac{\Omega}{\delta}} \right) b^\dagger + \left(a_{\lambda j} a^\dagger_{\lambda' j+\frac{\Omega}{\delta}} \right) b \right]. \tag{8.1}$$

The structure of this hamiltonian implies a mixing between the frequencies which mediate the exchange of phonon quanta. In order to express the entanglement between interacting optical modes we proceed to the calculation of the covariance between the spectral quadratures

$$\mathrm{Cov}[X_j, X_{j'}] = \langle X_j X_{j'} \rangle - \langle X_j \rangle \langle X_{j'} \rangle . \tag{8.2}$$

We will explicit the latter considering the Raman modified quadrature in eq. (6.24). In detail, for the sake of simplicity we neglect the polarization dependence and assume a diagonal susceptibility to rewrite the evolved quadrature as

$$X_j(\tau,\phi) = \frac{1}{\sqrt{2}}\Big(a_j + i\frac{\tau\sqrt{V_S}\omega_j}{2V\sqrt{2m\Omega}}\chi^{(1)}(a_{j+\frac{\Omega}{\delta}}b^\dagger + a^\dagger_{j-\frac{\Omega}{\delta}}b)\Big)e^{-i(\omega_j t+\phi)} + c.c. \quad . \tag{8.3}$$

We define the initial input state as an uncorrelated probe (i.e. multimode coherent state), which has the following properties

$$\begin{cases} \mathrm{Cov}[a_j, a_{j'}] = \delta_{j,j'}\sigma^2_{a_j}, \\ \mathrm{Cov}[a_j^\dagger, a_{j'}^\dagger] = \delta_{j,j'}\sigma^2_{a_j^\dagger}, \\ \mathrm{Cov}[a_j^\dagger, a_{j'}] = \delta_{j,j'}\,\mathrm{Cov}[a_j^\dagger, a_j], \\ \mathrm{Cov}[a_j, a_j^\dagger] = \mathrm{Cov}[a_j^\dagger, a_j] + [a_j, a_j^\dagger] = \mathrm{Cov}[a_j^\dagger, a_j] + 1 \quad . \end{cases} \tag{8.4}$$

Taking the latter relations into account, the predicted covariance, up to first order in the Raman interaction parameters τ and $\chi^{(1)}$, results in a quite elaborated expression

$$\begin{aligned} &\mathrm{Cov}[X_j, X_{j'}] = \qquad\qquad (8.5)\\ \text{(a)}\quad &+\delta_{j,j'}\frac{1}{2}\Big(\sigma^2_{a_j}e^{-2i(\omega_j t+\phi)} + \sigma^2_{a_j^\dagger}e^{2i(\omega_j t+\phi)} + 2\mathrm{Cov}[a_j^\dagger, a_j] + 1\Big) \\ \text{(b)}\quad &+\delta_{j,j'-\frac{\Omega}{\delta}}\, i\frac{\tau\sqrt{V_S}\omega_j}{4V\sqrt{2m\Omega}}\chi^{(1)}\Big(\sigma^2_{a_j^\dagger}b - \sigma^2_{a_j}b^\dagger + \mathrm{Cov}[a_j^\dagger, a_j](be^{-2i(\omega_j t+\phi)} - b^\dagger e^{2i(\omega_j t+\phi)}) \\ &\quad +\sigma^2_{a_{j+\frac{\Omega}{\delta}}}b^\dagger e^{-2i((\omega_j+\Omega)t+\phi)} - \sigma^2_{a^\dagger_{j+\frac{\Omega}{\delta}}}b^\dagger e^{2i((\omega_j+\Omega)t+\phi)} + \mathrm{Cov}[a^\dagger_{j+\frac{\Omega}{\delta}}, a_{j+\frac{\Omega}{\delta}}](b^\dagger - b) \\ &\quad +be^{-2i(\omega_j t+\phi)} + b^\dagger\Big) \\ \text{(c)}\quad &+\delta_{j,j'+\frac{\Omega}{\delta}}\, i\frac{\tau\sqrt{V_S}\omega_j}{4V\sqrt{2m\Omega}}\chi^{(1)}\Big(\sigma^2_{a_j}b^\dagger e^{-2i(\omega_j t+\phi)} - \sigma^2_{a_j^\dagger}b^\dagger e^{2i(\omega_j t+\phi)} + \mathrm{Cov}[a_j^\dagger, a_j](b^\dagger - b) \\ &\quad +\sigma^2_{a^\dagger_{j-\frac{\Omega}{\delta}}}b - \sigma^2_{a_{j-\frac{\Omega}{\delta}}}b^\dagger + \mathrm{Cov}[a^\dagger_{j-\frac{\Omega}{\delta}}, a_{j-\frac{\Omega}{\delta}}](be^{-2i((\omega_j-\Omega)t+\phi)} - b^\dagger e^{2i((\omega_j-\Omega)t+\phi)}) \\ &\quad -b^\dagger e^{2i((\omega_j-\Omega)t+\phi)} - b\Big) \quad . \end{aligned}$$

Despite the many terms involved in the previous equation, we can isolate the fundamental elements. We have three non-vanishing contributions (lines a,b,c) ruled by the Kroenecker deltas, which define the entangled pairs. Firstly, we report in line (a) the trivial correlation of each mode with itself ($\delta_{j,j'}$), which is equivalent to the single-mode quadrature variance. The other contributing terms are remarkably the one relative to the modes differing by the phonon energy ($\delta_{j,j'-\frac{\Omega}{\delta}}$ in (b), $\delta_{j,j'+\frac{\Omega}{\delta}}$ in (c)), whose intensity depend on the phonon operators and on the coupling factor of the ISRS interaction.
Importantly, the calculated covariances are also dependent on the statistical properties of the input optical field ($\sigma^2_a, \sigma^2_{a^\dagger}, \mathrm{Cov}[a^\dagger, a]$). Therefore, we can study the expected results as a function of the probe noise. We start by analyzing the quantum limited fluctuations in the case of the coherent states and then generalize to other sources.

8.2 Quantum regime

The quantum fluctuations implied by the Heisenberg uncertainty principle are an intrinsic property of quantum optical fields. In this section, we analyze how this typology of noise can be relevant in determining the statistical correlation features when dealing with a Raman interaction.
The typical probe employed in our experiments is in a coherent state. It is characterized by a symmetrical statistical distribution of the minimal uncertainty in the optical phase space, which quantitatively implies $\sigma_a^2 = \sigma_{a^\dagger}^2 = \mathrm{Cov}[a^\dagger, a] = 0$. If we express the predicted covariance in eq. (8.5) taking into account the previous relations we obtain

$$\begin{aligned} \mathrm{Cov}[X_j, X_{j'}] \quad = \quad & +\delta_{j,j'}\frac{1}{2} \\ & +\delta_{j,j'-\frac{\Omega}{\delta}}\, i\frac{\tau\sqrt{V_S}\omega_j}{4V\sqrt{2m\Omega}}\chi^{(1)}\Big(+ be^{-2i(\omega_j t+\phi)} + b^\dagger\Big) \\ & +\delta_{j,j'+\frac{\Omega}{\delta}}\, i\frac{\tau\sqrt{V_S}\omega_j}{4V\sqrt{2m\Omega}}\chi^{(1)}\Big(- b^\dagger e^{2i((\omega_j+\Omega)t+\phi)} - b\Big), \end{aligned} \tag{8.6}$$

which describes that the correlations are only detectable thanks to the minimal noise resulting from the commutation relation between the operators $a, a^\dagger$.
In order to estimate the magnitude of the phonon induced correlations, we consider the ratio between the vacuum quadrature variance ($\mathrm{Cov}[X_j, X_j] = 1/2$) and the Raman interaction dependent terms. We can derive this value in comparison with the mean value results for the quadrature amplitude modulation, in particular we analyze the model prediction in eq. (6.33) and the measurement in Fig. 7.3. From the analytical expression we read that the relative amplitude modulation ($\Delta A/A$) has the same order of magnitude of the out-of-diagonal/diagonal covariance contributions in eq. (8.6). Experimentally, we measure that the considered phonon induced amplitude modulations are on the order of 1%. Recalling the characterization of the probe covariance map in Fig. 4.9b, we report that the noise level of the measured covariance map is quantified in 2% of the probe vacuum variance, which means that the expected phonon correlation signal is not resolvable out of the employed experimental sensitivity. In order to reveal the features predicted in eq. (8.6) we should thus improve the performance of the detection system. A possible technical upgrade would require to increase the repetition rate of the acquisition in order to collect a larger statistics in the same experimental time. In the present configuration the detection rate is limited to 1 kHz, while the laser source is designed to work up to 200 kHz. An hundred times larger statistics should improve the signal-to-noise ratio of a factor 10 and thus discriminate the expected covariance modulations.
On the other hand, keeping in mind the dependence on the probe statistics in eq.(8.5), we can instead operate on the properties of the optical input. Actually, we can follow a stochastic resonance approach [26], which consists in properly adding white noise in the measurement in order to favour the detection of the desired output.
In our specific case the strategy is to increase the quantities $\sigma_a^2, \sigma_{a^\dagger}^2, \mathrm{Cov}[a^\dagger, a]$, which means to modify the coherent state condition. We discuss two possible approaches. In the next paragraph, we propose the hypothesis to change the statistics while preserving the quantum fluctuation limit, i.e. employing squeezed light. Otherwise, we can add noise above the Heisenberg limit, for example introducing fluctuations of classical nature, as we experimentally verify in the following section.

Squeezed light

Squeezed states of light are purely quantum objects in which the Heisenberg uncertainty is conserved, but interestingly is not equally distributed between the number and phase statistics. Formally, they can be described with the action of the squeezing operator

$$S(re^{i\vartheta}) = \exp\left(\frac{1}{2}r(e^{-i\vartheta}a^2 + e^{i\vartheta}a^{\dagger 2})\right) \tag{8.7}$$

which is ruled by the amplitude r and the phase ϑ of the squeezing factor.
If we calculate the new statistical quantities calculated on the squeezed coherent state they read

$$\begin{cases} \sigma_a^2 = \frac{\sinh 2r}{2} e^{i\vartheta}, \\ \sigma_{a^\dagger}^2 = \frac{\sinh 2r}{2} e^{-i\vartheta}, \\ \mathrm{Cov}[a_j^\dagger, a_{j'}] = \sinh^2 r \quad . \end{cases} \tag{8.8}$$

We see that, in comparison to symmetric coherent states which have $\sigma_a^2 = \sigma_{a^\dagger}^2 = \mathrm{Cov}[a^\dagger, a] = 0$, many contributions in eq. (8.5) are not vanishing anymore. Therefore, the visibility of many terms in eq. (8.5) can be controlled as a function of the amplitude of the squeezing factor, revealing the Raman multimode correlations. Nonetheless, the ideas discussed in this paragraph are just a perspective and a more detailed analysis should be performed to evaluate the experimental feasibility. In particular, while the correlation signal can be expected to improve on the order of the squeezing factor, it should be verified that the covariance uncertainty does not increase and the spectral noise remains uncorrelated.

8.3 Classical fluctuations

While the quantum regime is intrinsically characterized by the Heisenberg fluctuations, we can exploit the statistical features also in the classical one by modifying the coherent state approximation. In particular, randomization or chaotic generation processes can be exploited to increase the involved noise.
Regarding the correlation statistics, in the recent years many covariance based experiments using stochastic light have been implemented [15, 27, 28, 29]. Hereby we report the results of a project I contributed to and whose results are relevant in the discussion of the Raman induced multimode correlation [15].
The adopted technique is dubbed Femtosecond Covariance Spectroscopy and involves the measurement of the frequency-resolved intensity statistics of the probe pulse transmitted through the quartz sample, as depicted in Fig. 8.1. The key element of the experiment is the use of a noisy probe, whose statistical distribution is randomized pulse by pulse by means of a programmable pulse shaper. The noise can be introduced acting both on the amplitude or the phase of each spectral component. Importantly, the fluctuations are required to be spectrally uncorrelated. The result are intensity profiles which vary independently for each pulse repetition and frequency component, as shown in Fig. 8.2a.
The observable adopted to measure the entanglement between the probe modes is the Pearson correlation coefficient map defined as

$$\rho(I_j, I_{j'}) = \frac{\mathrm{Cov}[I_j, I_{j'}]}{\sigma_{I_j}\sigma_{I_{j'}}} \tag{8.9}$$

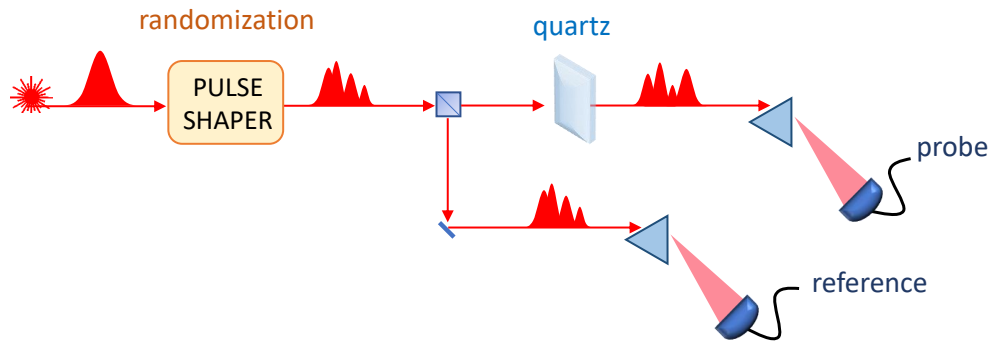

FIGURE 8.1: Femtosecond Covariance Spectroscopy setup. The spectrum of the probe light is randomized by means of pulse-shaping. The stochastic light is employed in a transmission experiment and the output pulse statistics is analyzed with a frequency-resolved detection with photodiode arrays.

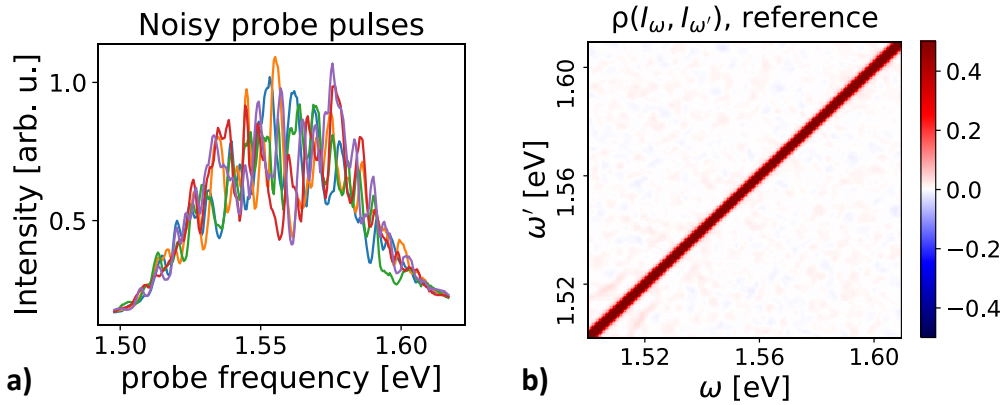

FIGURE 8.2: Probe pulse employed in Femtosecond Covariance Spectroscopy experiment. a) Example of the noisy probe intensity spectra for few pulse repetitions. b) Correlation coefficient map of the input probe.

which is calculated on the spectra acquired for many single-pulse repetitions (in this case 50k acquired at 5 kHz). In Fig. 8.2b we report the reference correlation map for the randomized input probe. We verify that the introduced fluctuations are highly uncorrelated and the map shows only the trivial diagonal correlation. The diagonal width is determined by the spectral correlation length of the fluctuations and sets the frequency resolution of the experiment.
The uncorrelated map of the input probe represents a white sheet where we can write the response induced by the interaction with the sample. In particular, we expect to reveal the Raman signatures due to the phonon excitation.
In order to describe the result quantitatively, we should adapt eq. (8.5) to an intensity description. Nevertheless, the qualitative features of interest are already deducible from the quadrature covariance. Indeed, the Raman mediated entanglement is represented by lines in the correlation map which describe the link between modes differing by the involved phonon energies. We can distinguish these in the correlation map in Fig. 8.3a, calculated on the light transmitted through the quartz sample. The measurement is performed with 1 mJ/cm^2 of probe fluence on the sample.
In order to obtain the spectrum of the involved vibrational modes, we average the map along the diagonal in Fig. 8.3b. Hence, we can identify the signal relative to the phonon Raman modes already detected in the average pump&probe measurements (Fig. 7.5d).

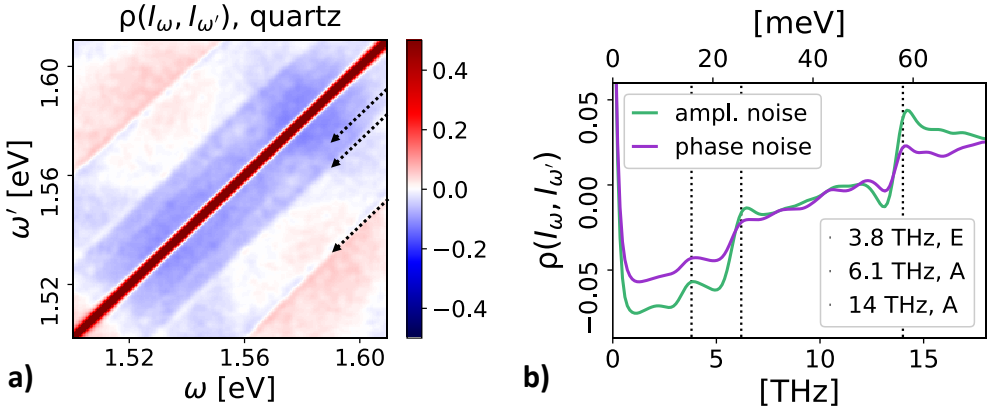

FIGURE 8.3: Multimode Raman induced correlations in classical stochastic intensity measurement [15]. a) Correlation coefficient map. The arrows highlight the phonon correlation lines imprinted by the Raman interaction. b) Phonon spectrum obtained averaging the map along the diagonal.

The correlation profile in Fig. 8.3b is reported for both configurations in which the noise is introduced on the probe amplitude or phase. We observe that there is a dependence on the shaping typology, which can be controlled to optimize the result. The analysis of the optimal shaping methods to use are considered in [15]. Moreover, the complete discussion together with the extension to non-equilibrium dynamics in pump&probe measurements are included in Giorgia Sparapassi's doctoral thesis [30].

References - part II

[1] M. Hase, K. Mizoguchi, H. Harima, S. Nakashima, M. Tani, K. Sakai, and M. Hangyo. "Optical control of coherent optical phonons in bismuth films". *Applied Physics Letters* 69.17 (1996).

[2] H. Sasaki, R. Tanaka, Y. Okano, F. Minami, Y. Kayanuma, Y. Shikano, and K. G. Nakamura. "Coherent control theory and experiment of optical phonons in diamond". *Scientific Reports* 8.1 (2018).

[3] T. Kampfrath, A. Sell, G. Klatt, A. Pashkin, S. Mährlein, T. Dekorsy, M. Wolf, M. Fiebig, A. Leitenstorfer, and R. Huber. "Coherent terahertz control of antiferromagnetic spin waves". *Nature Photonics* 5.1 (2010).

[4] D. M. Sagar, A. A. Tsvetkov, D. Fausti, S. van Smaalen, and P. H. M. van Loosdrecht. "Coherent amplitudon generation in blue bronze through ultrafast interband quasiparticle decay". *Journal of Physics: Condensed Matter* 19.34 (2007).

[5] D. Werdehausen, T. Takayama, M. Höppner, G. Albrecht, A. W. Rost, Y. Lu, D. Manske, H. Takagi, and S. Kaiser. "Coherent order parameter oscillations in the ground state of the excitonic insulator Ta2NiSe5". *Science Advances* 4.3 (2018).

[6] B. Mansart, J. Lorenzana, A. Mann, A. Odeh, M. Scarongella, M. Chergui, and F. Carbone. "Coupling of a high-energy excitation to superconducting quasiparticles in a cuprate from coherent charge fluctuation spectroscopy". *Proceedings of the National Academy of Sciences* 110.12 (2013).

[7] Y.-X. Yan, E. B. Gamble, and K. A. Nelson. "Impulsive stimulated scattering: General importance in femtosecond laser pulse interactions with matter, and spectroscopic applications". *The Journal of Chemical Physics* 83.11 (1985).

[8] R. Merlin. "Generating coherent THz phonons with light pulses". *Solid State Communications* 102.2-3 (1997).

[9] T. E. Stevens, J. Kuhl, and R. Merlin. "Coherent phonon generation and the two stimulated Raman tensors". *Physical Review B* 65.14 (2002).

[10] K. C. Lee, M. R. Sprague, B. J. Sussman, J. Nunn, N. K. Langford, X.-M. Jin, T. Champion, P. Michelberger, K. F. Reim, D. England, D. Jaksch, and I. A. Walmsley. "Entangling Macroscopic Diamonds at Room Temperature". *Science* 334.6060 (2011).

[11] D. G. England, K. A. Fisher, J.-P. W. MacLean, P. J. Bustard, R. Lausten, K. J. Resch, and B. J. Sussman. "Storage and Retrieval of THz-Bandwidth Single Photons Using a Room-Temperature Diamond Quantum Memory". *Physical Review Letters* 114.5 (2015).

[12] K. A. G. Fisher, D. G. England, J.-P. W. MacLean, P. J. Bustard, K. J. Resch, and B. J. Sussman. "Frequency and bandwidth conversion of single photons in a room-temperature diamond quantum memory". *Nature Communications* 7.1 (2016).

[13] F. Glerean, S. Marcantoni, G. Sparapassi, A. Blason, M. Esposito, F. Benatti, and D. Fausti. "Quantum model for impulsive stimulated Raman scattering". *Journal of Physics B: Atomic, Molecular and Optical Physics* 52.14 (2019).

[14] F. Glerean, G. Jarc, A. Marciniak, F. Giusti, G. Sparapassi, A. Montanaro, E. M. Rigoni, J. O. Tollerud, and D. Fausti. "Time-resolved multimode heterodyne detection for dissecting coherent states of matter". *Opt. Lett.* 45.13 (2020).

[15] J. O. Tollerud, G. Sparapassi, A. Montanaro, S. Asban, F. Glerean, F. Giusti, A. Marciniak, G. Kourousias, F. Billè, F. Cilento, S. Mukamel, and D. Fausti. "Femtosecond covariance spectroscopy". *Proceedings of the National Academy of Sciences* 116.12 (2019).

[16] E. O. Potma and S. Mukamel. "Theory of Coherent Raman Scattering". *Coherent Raman Scattering Microscopy*. Ed. by J.-X. Cheng and X. S. Xie. CRC Press, 2016.

[17] R. W. Boyd. "Chapter 1 - The Nonlinear Optical Susceptibility". *Nonlinear Optics (Fourth Edition)*. Ed. by R. W. Boyd. Fourth Edition. Academic Press, 2020.

[18] R. W. Boyd. "Chapter 3 - Quantum-Mechanical Theory of the Nonlinear Optical Susceptibility". *Nonlinear Optics (Fourth Edition)*. Ed. by R. W. Boyd. Fourth Edition. Academic Press, 2020.

[19] U. Weiss. *Quantum Dissipative Systems*. 3rd. World Scientific, 2008.

[20] K. G. Nakamura, K. Ohya, H. Takahashi, T. Tsuruta, H. Sasaki, S.-i. Uozumi, K. Norimatsu, M. Kitajima, Y. Shikano, and Y. Kayanuma. "Spectrally resolved detection in transient-reflectivity measurements of coherent optical phonons in diamond". *Phys. Rev. B* 94 (2016).

[21] J. F. Scott and S. P. S. Porto. "Longitudinal and Transverse Optical Lattice Vibrations in Quartz". *Phys. Rev.* 161 (1967).

[22] M. M. Wefers, H. Kawashima, and K. A. Nelson. "Optical control over two-dimensional lattice vibrational trajectories in crystalline quartz". *The Journal of Chemical Physics* 108.24 (1998).

[23] A. Rundquist, J. Broman, D. Underwood, and D. Blank. "Polarization-dependent detection of impulsive stimulated Raman scattering in α-quartz". *Journal of Modern Optics* 52.17 (2005).

[24] R. Medeiros de Araújo, J. Roslund, Y. Cai, G. Ferrini, C. Fabre, and N. Treps. "Full characterization of a highly multimode entangled state embedded in an optical frequency comb using pulse shaping". *Phys. Rev. A* 89 (2014).

[25] J. Erskine, D. England, C. Kupchak, and B. Sussman. "Real-time spectral characterization of a photon pair source using a chirped supercontinuum seed". *Opt. Lett.* 43.4 (2018).

[26] L. Gammaitoni, P. Hänggi, P. Jung, and F. Marchesoni. "Stochastic resonance". *Rev. Mod. Phys.* 70 (1998).

[27] X. G. Xu, S. O. Konorov, J. W. Hepburn, and V. Milner. "Noise autocorrelation spectroscopy with coherent Raman scattering". *Nature Physics* 4 (2008).

[28] L. J. Frasinski, K. Codling, and P. A. Hatherly. "Covariance Mapping: A Correlation Method Applied to Multiphoton Multiple Ionization". *Science* 246.4933 (1989).

[29] M. I. Suresh, P. S. Russell, and F. Tani. "Covariance spectroscopy of molecular gases using fs pulse bursts created by modulational instability in gas-filled hollow-core fiber". *Opt. Express* 28.23 (2020).

[30] G. Sparapassi. "Femtosecond Covariance Spectroscopy". PhD thesis. University of Trieste, 2020.

Part III

Application to Complex Quantum Materials

The description of materials at the fundamental level relies on the quantum mechanical interactions between the matter constituents. While in many situations their macroscopic realization can be approximated with a classical formalism, though in other fascinating systems, defined quantum materials, purely quantum effects survive over a wide range of energy and length scales [1]. The concept of quantum materials is representative of an increasingly larger research field encompassing condensed matter, cold atoms and quantum computing [2], which studies the intriguing effects emerging owing to the complex interactions involved. In particular, a lot of interest is raising in understanding and controlling them in order to achieve new functionalities and quantum-based devices [3].
The traditional definition of quantum materials developed from the study of correlated electron systems, which have a large number and variety of examples among transition metal oxides [4, 5]. The complexity in these systems is a consequence of the interplay between the various electronic, orbital, spin and lattice degrees of freedom [6, 7] which leads to materials with striking and attractive properties, such as magnetic phases [8, 9] and superconductivity [10, 11].
From the spectroscopist perspective, the advent of femtosecond laser sources opened up the possibility to manipulate and examine these materials at the typical timescale of the fundamental interactions, triggering a plethora of ultrafast studies [12, 13, 14]. The present thesis aims to help in moving a step forward in this direction, by enriching the amount of information inferable from ultrafast optical experiments in quantum materials.

In this last part of the dissertation, we explore the potentialities of the developed time-resolved multimode heterodyne detection technique as a tool for the investigation of complex quantum materials.
We consider two examples of different transition metal oxides. We study the insulating antiferromagnet Titanium Oxy-Chloride (TiOCl) and the high-temperature cuprate superconductor Yttrium Barium Copper Oxide (YBCO).
The ultrafast pump&probe response of TiOCl is reported in Chapter 9. Focus is set on the orbital degree of freedom of the valence $3d$ electron by adopting pump and probe resonant to optical dd transitions. A dependence on orbital excitation is revealed together with a vibrational response, signaling a orbital-phonon coupling.
In Chapter 10 we study the non-equilibrium dynamics in the YBCO sample. The coherent phonon response is measured at room temperature. The quadrature dynamics is then investigated as a function of the sample temperature and an anomalous response in the optical phase is observed at low-temperature.

Chapter 9

Ultrafast orbital dynamics in the 1D quantum magnet TiOCl

Strongly correlated electron materials show striking properties which are the outcome of the complex interplay between their various fundamental attributes, such as the crystalline and electronic structure, the magnetic spin properties and lattice excitations.
A key role is set by the orbital degree of freedom [6], which defines the electronic distribution ruling for instance the structure geometry or the Coulomb repulsion. In particular, the anisotropic shape of the valence $3d$ levels in transition metal oxides orients the interaction along preferential directions, leading for example to materials with low-dimensional character.
The orbital structure is crucial also in determining the magnetic properties, since the spin interaction is correlated to the electronic distribution. Titanium-Oxy-Chloride (TiOCl) is an interesting 1D-like quantum antiferromagnet where we can observe the orbital-spin interaction at play. Remarkably, at low temperature the system shows a magnetic transition to the exotic Spin-Peierls phase [15, 16].

In this context, ultrafast optical studies are useful not only in order to understand the sample properties, but also to control it and drive new out-of-equilibrium states. Considering its fundamental role, it would be relevant to manipulate the electronic structure in a controlled way, for instance with the aim of governing the exchange interaction.
In TiOCl, the state of the Ti single valence electron determines the exchange interaction. Therefore, intraband dd transitions represent a direct way to modify the orbital configuration, and an indirect way to modify the spin [17, 18] and other coupled degrees of freedom, such as the lattice phonons [19, 20].
Orbital d-band transitions have been already studied in optical and inelastic x-ray scattering experiments to probe the equilibrium properties [21, 22]. Hereby, we explore the possibility to exploit the dd optical transitions both to stimulate and test the non-equilibrium response of the material. We measure in the room temperature antiferromagnetic phase. We reveal different dd dependent absorption mechanisms and get some insights on the structural modifications using the dd as Crystal Field indicators.
Firstly, we characterize the sample response with intensity pump&probe measurements employing a broadband White-light probe. We finally apply the time-resolved multimode heterodyne detection in this framework to study the intraband interaction with a narrowband ultrashort pulse. We disentangle the spectral amplitude and phase and the multimode dynamics reveals signatures of an orbital-phonon coupling.

9.1 Titanium Oxy-Chloride (TiOCl)

TiOCl is a transition metal oxide insulator presenting low-dimensional attributes which are crucial in determining its peculiar magnetic properties.
The material is formed by layers of Ti and O, separated by the Cl atoms, which are stacked along the c-axis (Fig. 9.1). The unit cell is orthorhombic belonging to the $Pmmn$ crystallographic group. The unit vectors at room temperature are a = 3.79 Å, b = 3.37 Å and c = 8.06 Å [23]. The fundamental coordination unit is a Cl_2O_4 octahedron surrounding the Ti atom.

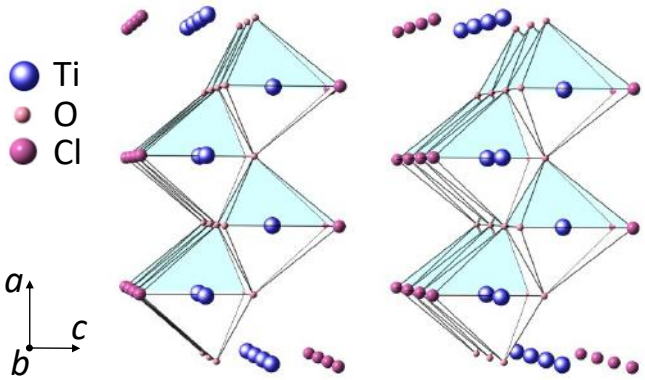

FIGURE 9.1: TiOCl crystalline structure. The fundamental coordination unit is an O-Cl octahedron enclosing a Ti atom. They are arranged in bi-dimensional layers stacked along the c-axis, which are characterized by 1-D atomic chains along the b-axis. [24].

In this environment, the titanium transfers 3 electrons to the O and Cl atoms such that the electronic configuration results $Ti^{3+}O^{2-}Cl^{-}$, with Ti in a $3d^1$ state. Moreover, as we will discuss in the following, the single Ti electron ground state is the $d_{y^2-z^2}$ orbital oriented in the b-c plane[1].
Another important structural feature to note is the existence of 1D atomic chains along the b-axis. Indeed, this low dimensional attribute together with the orbital ground state are key elements in defining the magnetic properties.

9.1.1 Magnetic properties

TiOCl presents a rich phase diagram involving transitions between states with different structural and magnetic attributes. At high temperature, the system is an antiferromagnetic 1D Heisenberg chain, along which the Ti ions dimerize below T_{C1} = 67 K in the so-called spin-Peierls transition, observed so far only in titanium oxy-halides and $CuGeO_3$ among inorganic compounds [15, 16]. The phase diagram of TiOCl is further enriched by the presence of an intermediate phase at temperatures above T_{C1} and below T_{C2} = 91 K.
The electronic distribution owing to the orbital ground state defines the magnetic exchange interaction along the b-axis. The interaction between the $S = \frac{1}{2}$ spins of the electrons on the different Ti sites is ruled by the hamiltonian

$$H = J \sum_{i,j} \mathbf{S}_i \cdot \mathbf{S}_j \tag{9.1}$$

[1]We assume the orbital reference frame x, y, z matching to the crystallographic axes a, b, c.

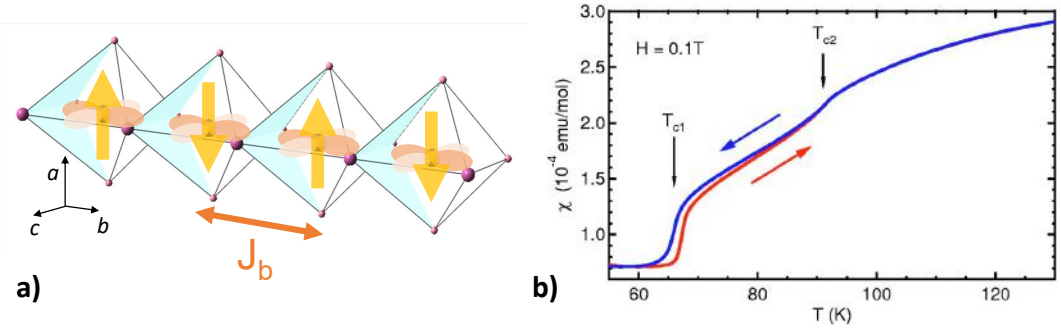

FIGURE 9.2: The magnetic properties of TiOCl are set by the ground state $3d_{y^2-z^2}$ orbitals along the 1D Ti-chain. a) Antiferromagnetic spin orientation due to exchange interaction along the b-axis. b) Magnetic phase transitions. The magnetic susceptibility from [25] highlights two critical temperatures, accounting for the transitions to the incommensurate and the Spin-Peierls phases.

where J is the exchange parameter and i, j label the lattice site.
The exchange interaction has a strong anisotropic character and can be quantified along the different directions as $J_b = 660$ K, $J_a = -10.5$ K, $J_c = -16.7$ K [26, 27]. It follows that the leading contribution sets an antiferromagnetic ordering along the b chain (Fig. 9.2a), while the a and c ferromagnetic terms are weak and are involved in magnetic frustration between the 1D chains.
The interplay of the orbital-spin interaction with the lattice excitations triggers then the temperature dependent phase transitions [28]. The balance between exchange and vibrational energy is crucial and at low temperature the Spin-Peierls phase appears. Neighboring spins dimerize leading to pairs with $S = 0$, which set that the magnetic susceptibility in Fig. 9.2b is null below T_{C1}. The existence of the intermediate phase is more complex to address and it has been described accounting for the interchain frustrated exchange interactions in addition to the phonon contribution [29, 30, 31].

9.1.2 *dd*-orbital transitions

As we already introduced, the orbital state of the $3d$ valence electrons in transition metals is a fundamental attribute in determining the material properties. We now discuss the orbital splitting and the $d_{y^2-z^2}$ ground state in TiOCl on the basis of its crystalline structure. Moreover, we consider the possible intraband excitations between the different d-orbital states. The d-energy levels of the Ti atom are five-fold degenerate in an isotropic setting. However, when placed in the crystalline environment the symmetry is broken and the degeneracy is removed. Precisely, the anisotropic Coulomb repulsion with the electronic clouds of the surrounding atoms energetically favors orbital states with a minimized overlap between the electronic wavefunctions.
This approach is described by the Crystal Field theory. In the TiOCl case we have the Ti atom inside an octahedral environment. In Fig. 9.3 we describe the corresponding d-band Crystal Field splitting. In an ideal octahedral symmetry the result is the separation in two states, respectively two- and three-fold degenerate. Then, considering the distorsion induced by the different effects of Cl with respect to O atoms, the degeneracy is completely removed. The reported energy distribution of the d-levels is based on the results of theoretical and experimental studies [21, 22, 23, 32].

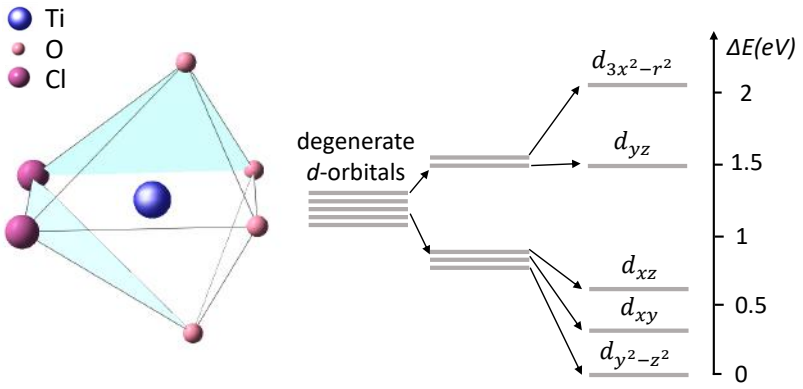

FIGURE 9.3: Crystal Field splitting of the 3d orbital levels due to distorted octahedral enviroment surrounding the single electron ($3d^1$) Ti atom.

In the TiOCl ground state, the single electron in the Ti^{3+} atom occupies the lowest $d_{y^2-z^2}$ orbital. Possible orbital excitations can occur as the result of transitions to higher energy levels. In particular, we consider the capability of stimulating them optically.
Optical intraband ($\Delta L = 0$) transitions are usually forbidden in centrosymmetric systems because the momentum conservation rule ($\Delta L = \pm 1$) is not fulfilled. Nevertheless, inversion symmetry is broken in TiOCl by the strong octahedral distorsion and optical *dd* transitions are allowed.

Equilibrium absorption measurements

The optically active orbital transition lying in the insulator gap can be referenced with absorption measurements. In detail, TiOCl presents a Mott gap involving the electron transfer between adjacent Ti atoms above 2 eV [33]. Hence, the *dd* transitions below gap can be distinguished. In particular, we can exploit our laser source to explore the visible and near-infrared range.

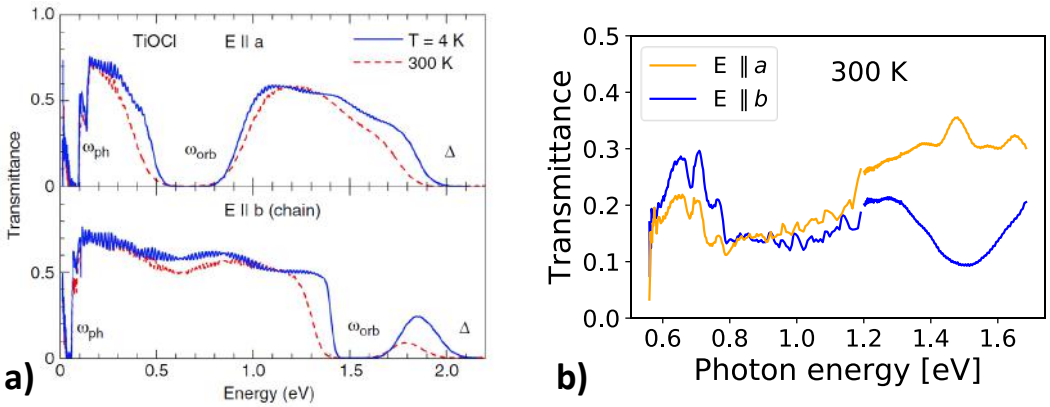

FIGURE 9.4: Transmittance spectrum due to optical orbital *dd* transitions as a function of the polarization orientation. a) optical absorption from literature [21]. b) optical absorption measured.

The optical transitions have a strong polarization dependence following the symmetry selection rules. In Fig. 9.4 we show the polarization dependent transmittance

spectrum from literature (a) [21] and tested experimentally on our sample (b). A thin TiOCl sample is prepared by exfoliating along the c-axis and we analyze the transmission in this direction. We observe the polarization dependence generating a different spectrum with respect to the transitions to the d_{xz} and d_{yz} states. The absolute value of the transmittance between literature and experiment is due to different sample thickness. Fringes effects are a consequence of interference between multiple reflections in the $\sim 10\mu$m thick sample.
In the following, we exploit the optical properties of the analyzed dd transitions in ultrafast pump&probe experiments. Precisely, we target intraband transitions both to stimulate and test the orbital dependent non-equilibrium dynamics. We pump the near-infrared transition and probe in the visible range.

9.2 Ultrafast investigation of orbital dynamics

Femtosecond lasers can represent the tool to obtain the control of magnetism at the fastest timescale. Pump&probe experiments are employed to explore and control photoinduced ultrafast phenomena like fast demagnetization, recovery of the magnetic order or the onset of metastable states [34]. Since microscopically the spin ordering is governed by the exchange interaction, studies are focusing on its possible ultrafast manipulation [17, 18, 35].
On a fundamental level, exchange interactions emerge from the repulsive Coulomb interactions between electrons and are most sensitive to electronic perturbations. We discussed in particular how the magnetic properties in TiOCl are strongly defined by the orbital ground state. Following this line of reasoning, we thus employ the considered orbital dd excitations as a route to manipulate the electronic distribution and in turn modify the magnetic exchange interaction. Though dd transitions were frequently overlooked in magnetic studies due to their optical condition $\Delta S = 0$, their correlation with the exchange interaction has recently been highlighted [17, 18].

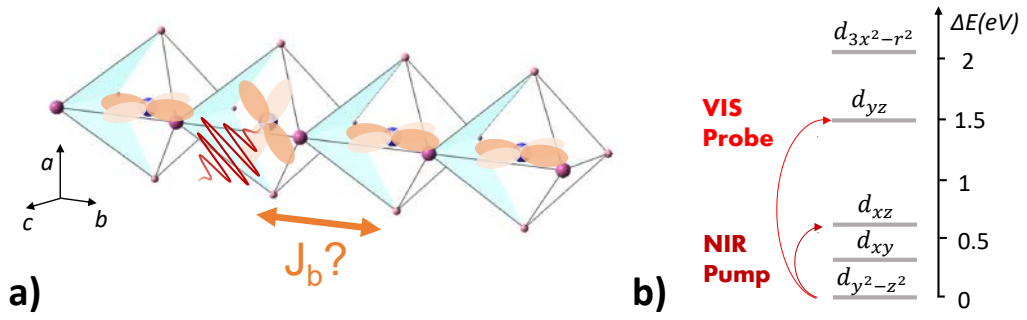

FIGURE 9.5: Pump&probe approach in TiOCl. a) The pump pulse modifies the orbital ground state by means of a resonant dd excitation, perturbing the equilibrium exchange interaction. b) Orbital transition targeted by the optical pump and probe pulses employed.

In the TiOCl insulator, the localized single electron system permits a rather simple interpretation of the orbital effects of the photoinduced excitation. In Fig. 9.5a we represent the effect of an optical induced orbital transition. In particular, we consider a near-infrared pulse at ~ 0.7 eV exciting the valence electron from the ground state to the d_{xz} orbital.

We expect this perturbation of the electronic distribution along the chain to modify the equilibrium exchange interaction of the room temperature antiferromagnetic phase. In order to investigate the resulting non-equilibrium state we setup a pump& probe experiment. We employ a near infrared pump resonant to the d_{xz} transition. On the other hand we probe in the visible range, with focus on the effects relative to the d_{yz} absorption.

9.2.1 Time-resolved white-light continuum spectroscopy

In this section, we perform ultrafast intensity studies probing on the entire visible range exploiting a broadband white-light pulse. The experiment is setup employing the Near-Infrared (NIR) idler beam produced by the OPA system. We split it in two (Fig. 9.6a). Part of it is used directly to pump the sample, while the other portion generates a White-Light (WL) continuum through non-linear interaction in a YAG crystal. The pump fundamental is then filtered out of the WL beam with a dichroic mirror. The WL pulse is thus transmitted through the sample and it is frequency-resolved and detected in a photodiode array. In Fig. 9.6b we report the intensity spectrum of the employed probe. In the presented experiments we use a fluence of 10 mJ/cm^2 for the pump and 30 μJ/cm^2 for the probe. By studying the WL spectrum as a function of the tunable pump delay, we build the dynamical map in Fig. 9.6c, which presents the non-equilibrium intensity differential.

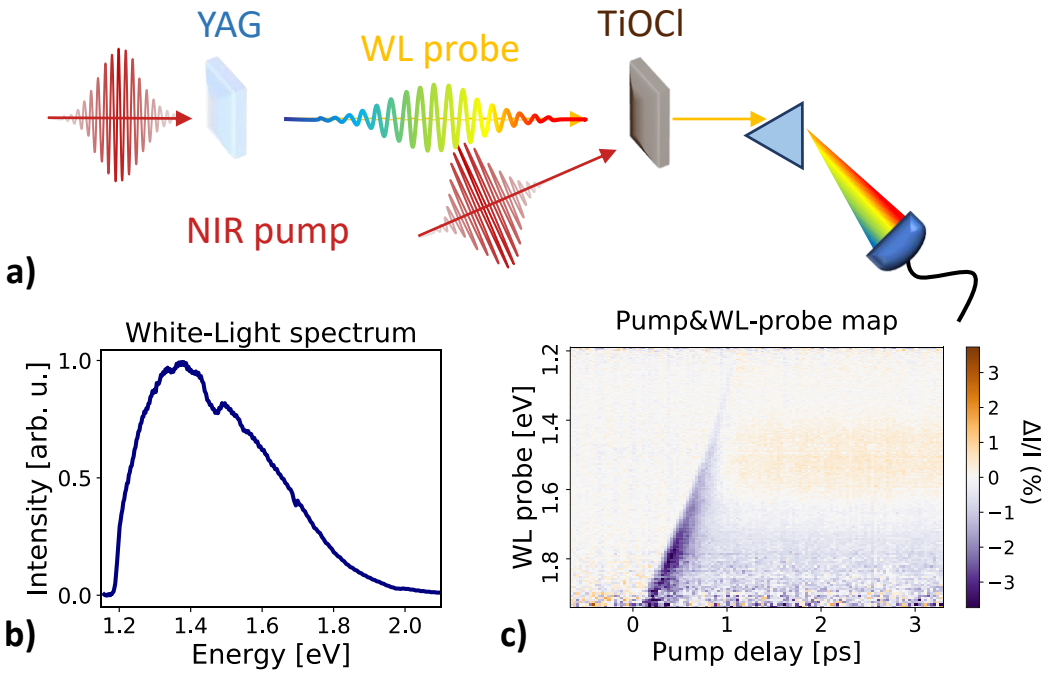

FIGURE 9.6: Pump& White-Light Probe experiment. a) Measurement setup: The NIR laser beam is split in two to generate a white-light (WL) probe in the YAG non-linear crystal and to pump the TiOCl sample. The frequency-resolved intensity spectrum of the WL pulse is detected with a photodiode array and reported in (b). c) Example of Pump&WL-probe map: the non-equilibrium differential is plot as a function of WL frequency and pump delay.

The example map reported in Fig. 9.6c is relative to the case where both pump and probe are maximally absorbed by the relative *dd* transitions. As reported in Fig. 9.4,

the pump is maximally absorbed if polarized along the a-axis, while the probe along the b-axis. This triggers a spectral dependent dynamics which we analyze in more detail in Fig. 9.7. The overlap signal has a sickle shape due to the chirped temporal distribution of the WL components. We do also correct for this effect in in Fig. 9.7a.

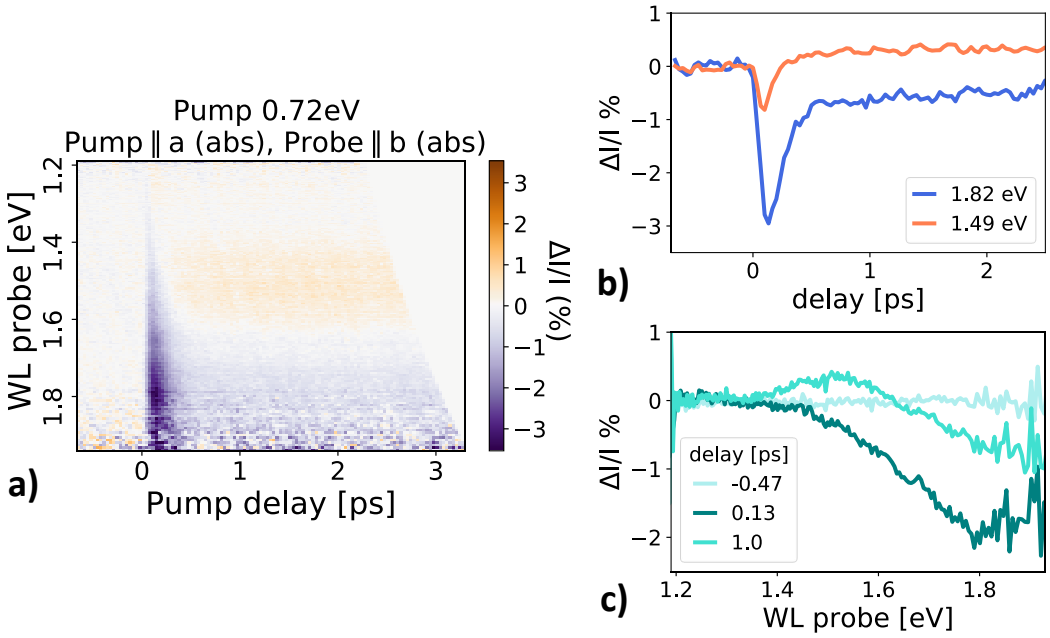

FIGURE 9.7: Pump& White-Light Probe measurement of ultrafast orbital response. Pump and probe are polarized in order to be absorbed in the involved dd transitions. The pump is absorbed along the a-axis, while the probe along the b-axis (Fig. 9.4). a) Frequency-delay map corrected in time for the probe chirp. We can distinguish two spectral regions with different responses at the positive times. b) The selected cuts at a fixed probe frequency exemplify the different dynamics observed. c) Spectral dependence at fixed pump delay.

We can distinguish three contributions in the ultrafast dynamics: a negative overlap signal and two different regions in the positive times. We observe a positive transmittivity modulation around 1.5 eV and a negative differential at the higher energy components. In Fig. 9.7b we show the time dependence for selected frequencies in each of the two different regions. In Fig. 9.7c we highlight the spectral response at three different time-delays (negative time, overlap, positive time).

In the following, we exploit polarization and energy tuning in order to change the orbital absorption condition. This allows us to discriminate the different non-equilibrium effects which are taking place.

9.2.2 Pump-orbital response

We start by isolating the effects of the pump absorption only. In order to do this we orient the probe along the a-axis so it is minimally absorbed. Then, in Fig. 9.8 we compare the effects of the polarization dependent absorption of a pump resonant to the d_{xz} transition. We observe that only when the pump is absorbed (a-polarization, Fig. 9.8a) a negative change in the transmittivity is present at positive time, while the response is null when the pump is not absorbed (b-polarization, Fig. 9.8b). We confront the time-dependence in the two cases at the selected probe frequency of

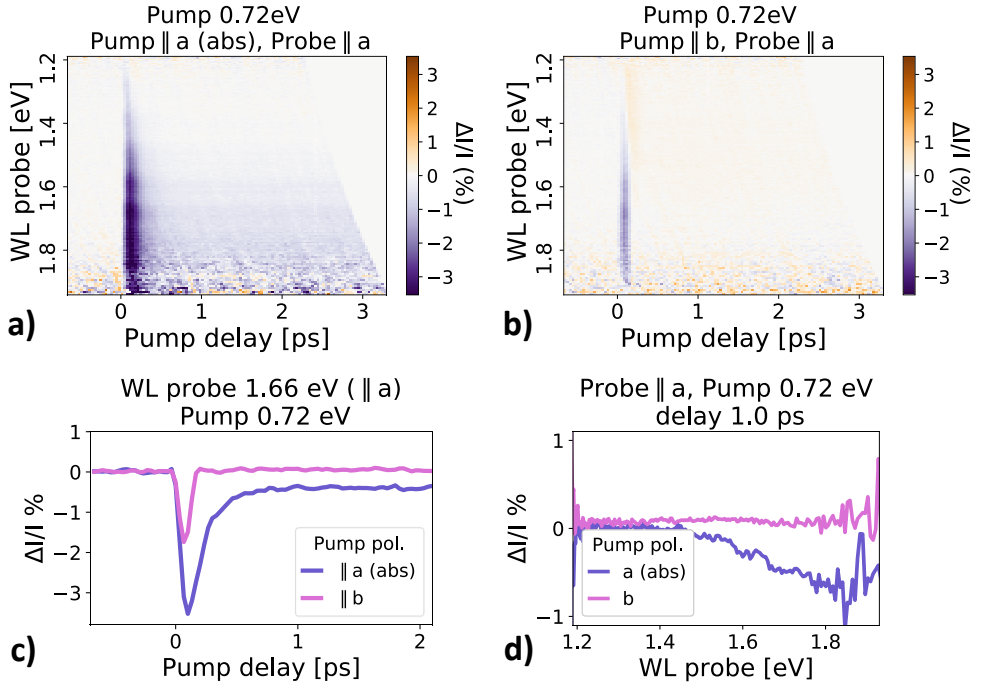

FIGURE 9.8: Effects of resonant pump absorption. a) Negative transient transmittivity induced by a-polarized pump absorbed in the dd. b) Absence of positive time response with b-polarized not-absorbed pump. c) Comparison of dynamical profiles for selected probe frequency. d) The spectral dependence at positive times highlights that the effect is more relevant at high probe energies.

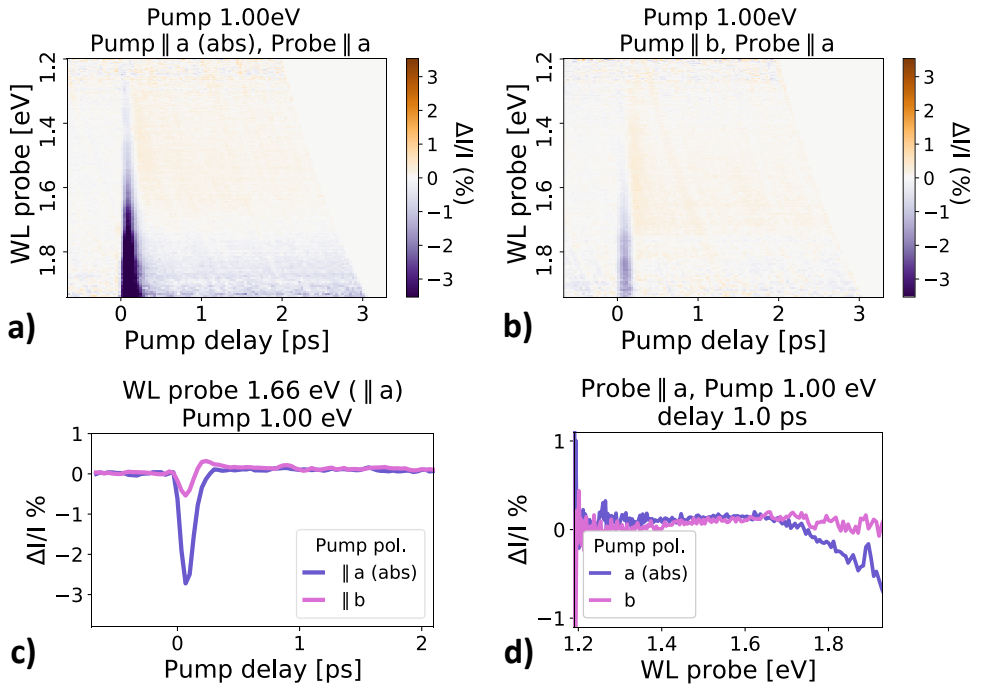

FIGURE 9.9: Effects of non-resonant pump absorption. The pump energy (1 eV) is not in the optimal dd absorption range. a) Weak negative transient transmittivity induced at high frequency with the pump absorption. b) Reference map without orbital absorption. c) Selected frequency profile. d) Spectral response at positive times.

1.66 eV in Fig. 9.8c. When the pump is not absorbed there is no signal other than the coherent overlap, while a negative differential is triggered when the pump is absorbed. In Fig. 9.8d we compare the spectral response at the positive times and reveal that the effect is maximized at higher energies.
Another useful parameter to reference the orbital absorption is the pump energy. Indeed, in Fig. 9.9 we detune the *dd* resonance using a 1.0 eV pump. In comparison with the resonant pump absorption (Fig. 9.8a), the result in Fig. 9.9a is a reduction of the negative non-equilibrium response at positive times, which we conclude to be owing to the d_{xz} orbital absorption. The outcome with *b*-polarized not absorbed pump in Fig. 9.9b is not affected by the change in pump energy and does not present a response in the positive times. In Fig. 9.9c, without pump absorption we distinguish a fast ($\sim$ 100 fs) positive peak, which we interpret as ground state bleach. We compare the spectral features in the slow timescale between the two orientations of the non-resonant pump in Fig. 9.9d and appreciate only a residual response whit the pump *a*-polarized.

9.2.3 Probe-orbital response

We now repeat the measurements in the previous different pump configurations with a probe polarized along the *b*-axis and sensitive to the orbital absorption in the visible to the d_{yz} level.
In Fig. 9.10 we report the data obtained with pump energy in resonance with the NIR *dd* (which targets the d_{xz} orbital). In Fig. 9.10a (as already presented in Fig. 9.7a) we observe that on top of the negative transmittivity, which is due to the absorbed pump, we reveal a wide region of the map with positive signal. Therefore, the probe is recording an increasing of the transient transmittivity which is revealed only if the probe is maximally absorbed by the visible *dd* transition.
If we inhibit the pump absorption setting the polarization orientation along the *b*-axis (Fig. 9.10b) we note that the increased transmittivity effect in the picosecond timescale is still present. Hence, the positive response is a non-equilibrium effect not directly linked to the orbital excitation induced by the pump pulse. In addition, avoiding the pump absorption isolates the positive contribution from the negative response.
As we show in Fig. 9.10c, the probe dependent effect is a positive dynamics. The fast peak is likely due to ground state bleach, while the picosecond response is probably a thermal increase of the sample transparency. From the spectral analysis in Fig. 9.10d, we observe that the maxima of the differential response are found around 1.5-1.6 eV, suggesting a correlation with the energy of the d_{yz} transition (Fig. 9.4). Moreover, we note that the spectral dependence is more peaked when the pump is absorbed.
The increased transmittivity is confirmed also when detuning the pump energy out of the transition resonance in Fig. 9.11. If this is non-resonant, both with pump absorbed (Fig. 9.11a) or not (Fig. 9.11b) the result is similar. We can appreciate this comparing the details of the dynamical (Fig. 9.11c) and of the spectral (Fig. 9.11d) response. The positive time response is a positive change of the differential intensity. However, in comparison with Fig. 9.10d, in Fig. 9.11d we have that the spectral response is peaked to slightly higher energies (1.6-1.7 eV).

We summarize in Fig. 9.12 the spectral dependence of the observed positive time dynamics (at 1 ps of pump delay) in the different configuration analyzed. We collect

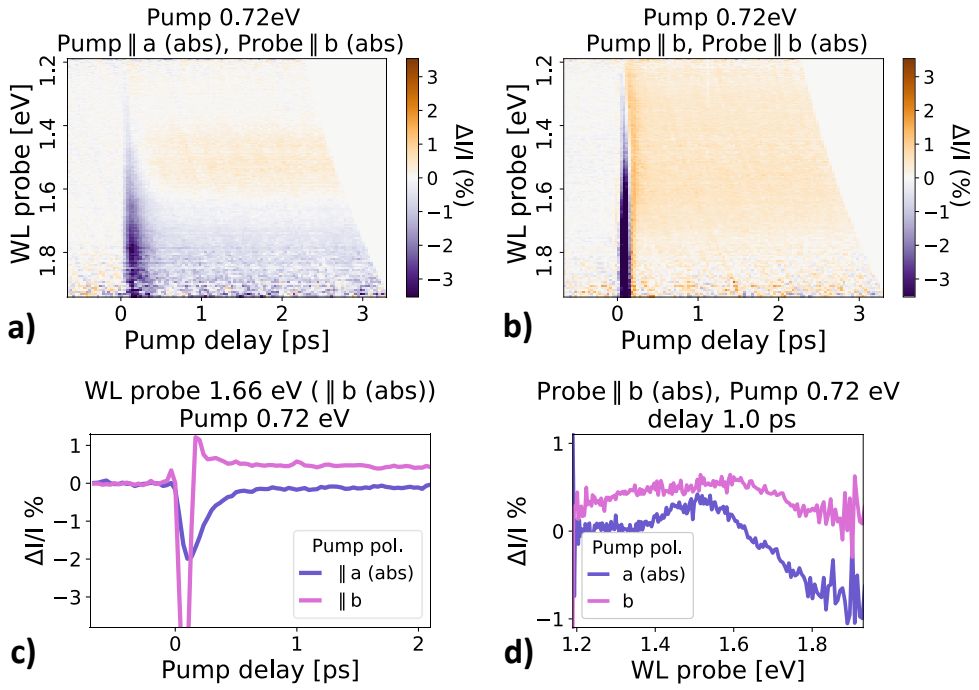

FIGURE 9.10: Effects of orbital probe absorption with resonant pump. The b-polarized probe is sensitive to dynamical induced transparency revealed by positive transient transmittivity. a) Map with combined pump and probe absorption responses. b) Positive transmittivity without orbital pump excitation. c) Profiles at selected frequency. d) Spectral dependence at positive time (1.0 ps).

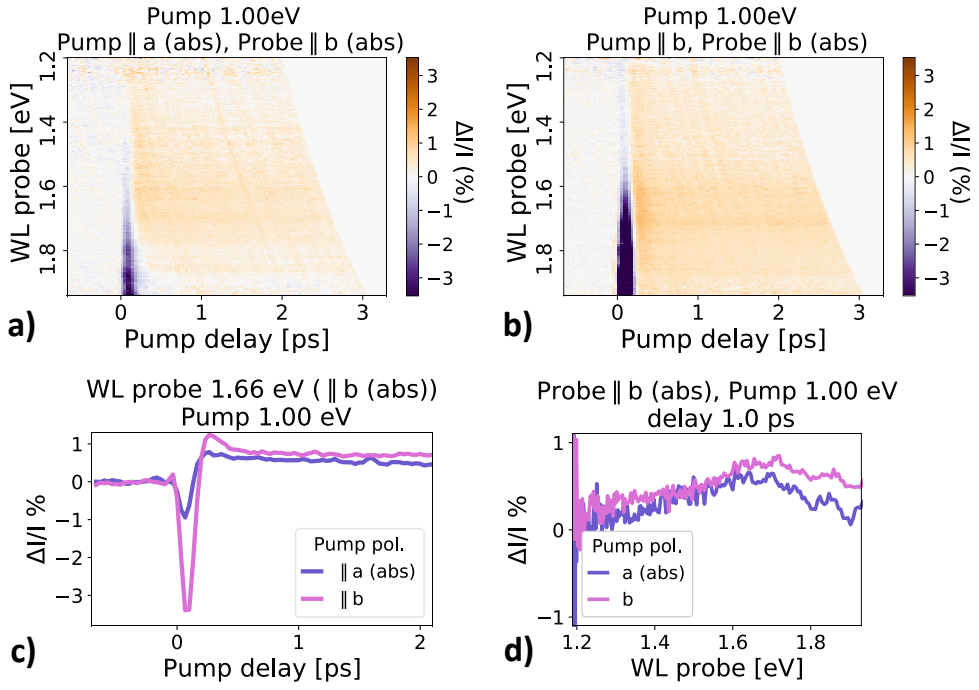

FIGURE 9.11: Effects of orbital probe absorption with non-resonant pump. Negative transmittivity effect due to pump absorption is no more revealed. a) a-polarized pump map. b) b-polarized pump map. c) Profiles at selected frequency. d) Spectral dependence at positive time (1.0 ps).

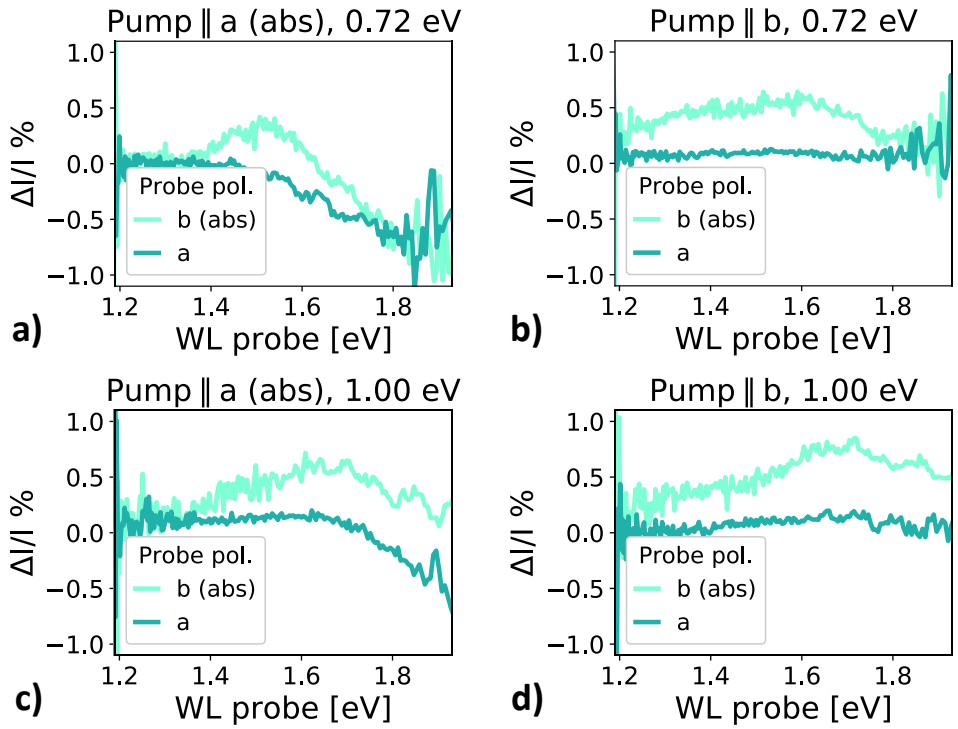

FIGURE 9.12: Summary of orbital absorption effects at positive times (1 ps). a) Resonant pump, absorbed. b) Resonant pump, not absorbed. c) Non-resonant pump, absorbed. d) Non-resonant pump, not absorbed. The comparison between probe orientations reveals an increased transmittivity when the probe is maximally absorbed. Orbital pump absorption implies instead a negative transmittivity response at high energy (a,c).

together the signals relative to the different probe polarizations in order to compare them directly in the different pump configurations (resonant/non-resonant, a/b-polarization). We distinguish two main phenomena.
On one hand we have a negative transmittivity modulation when the pump is absorbed in the d_{xz} orbital transition, namely with pump a-polarized as in Fig. 9.12a,c. The signal is maximized for the high energy components of the probe pulse, which are close to the onset of the Mott-gap.
On the other hand, we report a generalized increased transmittivity in the visible range on the slow picosecond timescale when the probe is sensitive to the d_{yz} orbital absorption. The b-polarized probe has always a positive differential. Nevertheless, peak and shape of the spectral response are slightly varying among the different cases.

In short, with this first experimental survey we highlighted the role of dd excitations in both stimulating and probing an ultrafast equilibrium response. In the next section we improve the discussion adopting the multimode heterodyne detection approach developed in this thesis.

9.3 Probe field dynamics via heterodyne detection

After the exploration of the ultrafast response on the broad visible range with white-light intensity measurements, we investigate the spectral dynamics of the probe electric field by means of time-resolved multimode heterodyne detection. This experiment employs an ultrafast probe with quasi monochromatic bandwidth. Pump and probe beams are generated in our setup as idler and signal outputs of an OPA, which implies that the photon energies of the two are co-dependent (their energy sum is fixed). We tune them in such a way that both pulses are close to the involved *dd* transitions. We use a 0.75 eV pump and 1.66 eV probe. The fluences are respectively 6 mJ/cm^2 and 150 pJ/cm^2. We perform the experiment with both pulses oriented in their optimal absorption polarization (pump$\|a$, probe$\|b$). The time- and frequency-resolved heterodyne maps for the field amplitude and phase are presented in Fig. 9.13a,b.

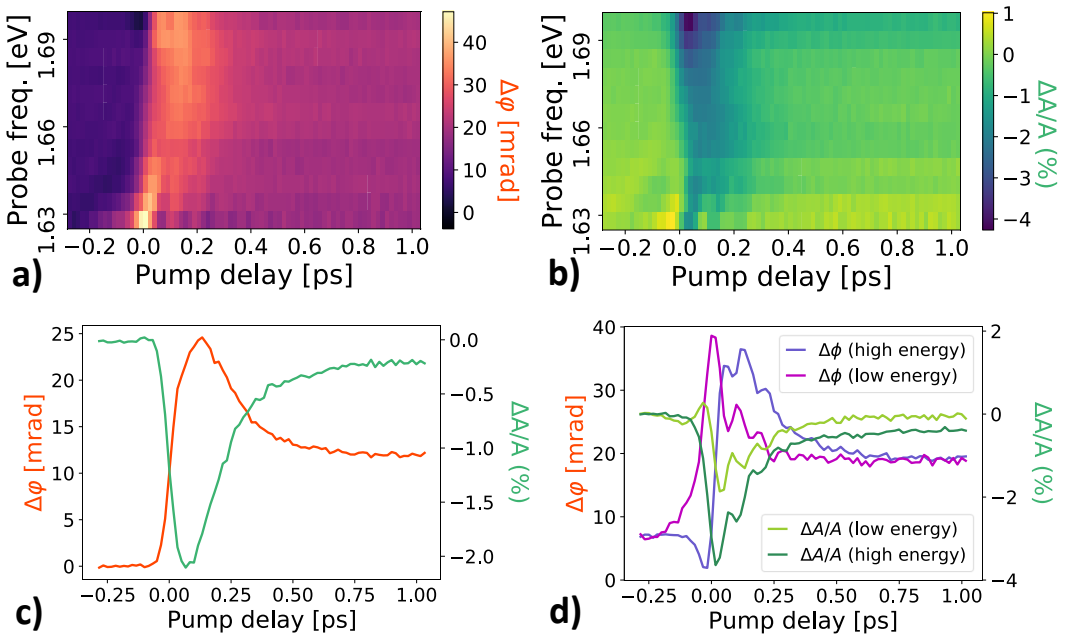

FIGURE 9.13: Orbital dependent time-resolved heterodyne trace in TiOCl. Pump and probe pulses are both close to resonance to a different orbital transition. a) Frequency-resolved phase dynamics. b) Frequency-resolved amplitude dynamics. c) Dynamical trace averaged along the probe spectrum. d) The non-equilibrium response on the tails of the probe spectrum reveals coherent oscillations.

We note that phase and amplitude time dependence of the probe spectral components are distinct. In Fig. 9.13c, we plot the non-equilibrium response integrated along the probe spectrum. We see that phase and amplitude pump induced changes have an opposite sign and they also decay differently. The fast and slow timescales contributions have different weight, which likely indicates that amplitude and phase are sensitive to distinct effects.
Furthermore, if we analyze the spectral dependence in the frequency-resolved maps (Fig. 9.13a,b), we see that remarkable information is present on the spectral tails. We show in Fig. 9.13d the fast decaying oscillations thereby visible. We state that they

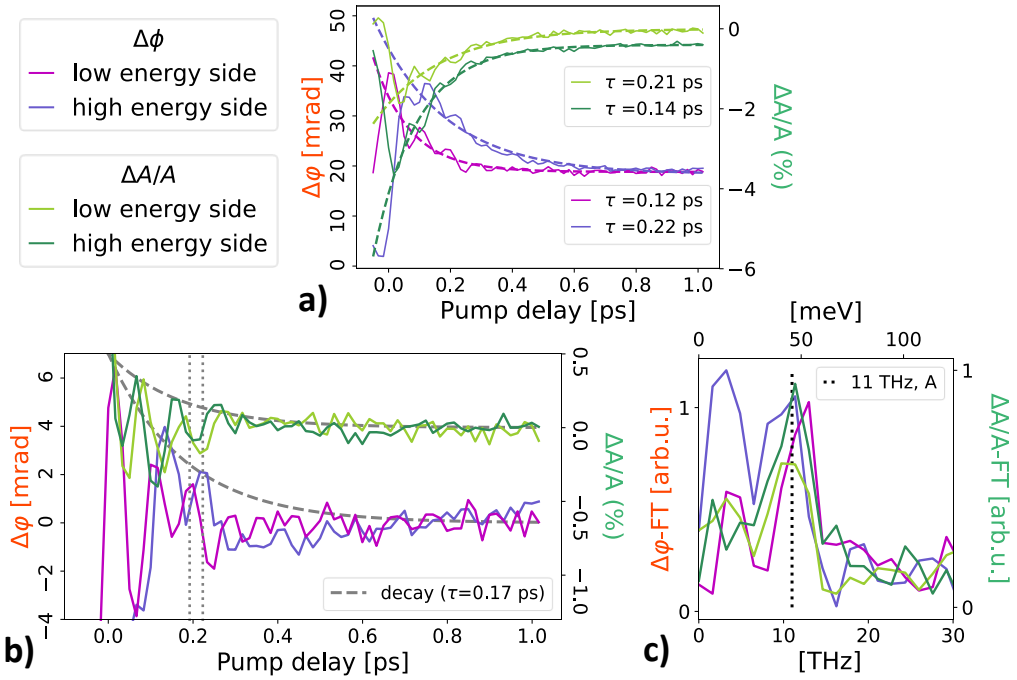

FIGURE 9.14: Analysis of coherent phonon oscillations in TiOCl. a) Fit of the exponential decay at positive time. b) Oscillations after the subtraction of the exponential fit. The damping time (approximated by the dashed line) is comparable with the average one of the underlying exponentials. The dotted lines highlight the phase shift between phase and amplitude oscillations. c) The Fourier Transform spectrum of the oscillations identifies the 11 THz totalsymmetric phonon mode.

are a signature of Impulsive Stimulated Raman Scattering owing to an excited coherent vibrational response which eludes spectrally integrated measurements.
We analyze the details of the observed oscillations in Fig. 9.14. In order to separate the oscillations from the underlying dynamics we fit the exponential decay at positive times (Fig. 9.14a). The obtained decays vary slightly for each trace, but in order to get a gross common estimation we calculate the average decay time of 0.17 ps. In Fig. 9.14b we plot the positive dynamics subtracted of the fitted exponential trends. We observe that the oscillations are decaying in few hundreds of femtoseconds. In order to confront the decay timescales for both amplitude and phase oscillations, we trace as guides to the eye the exponential trends with the estimated average decay time of 0.17 ps. We note that the oscillations and the approximation of the underlying dynamics are damped in a comparable timescale. This suggests a correlation between the underlying and oscillating dynamical features.
In order to address the coherent oscillations to a vibrational ISRS process we return to the phase relation between amplitude and phase dynamics pointed out in the quartz experiments (Chapter 7). With the help of the dotted reference lines, we can verify that the amplitude oscillations of each spectral component are $\pi/2$ shifted with respect to the corresponding phase one. Precisely, the two sides of the spectrum present an opposite ($\pm\pi/2$) shift, as expected for the ISRS interaction. However, since the equilibrium spectral phase is slightly chirped, especially on the low energy tail, it is not easy to discriminate if the process is imparting a spectrally uniform modulation on the amplitude or on the phase dynamics. Nevertheless, a

strong evidence of the phonon character of the observed oscillations is retrieved by the Fourier Transform analysis in Fig. 9.14c. Indeed, we distinguish a component at 11 THz which is identified with a totalsymmetric vibrational mode of the TiOCl sample [36, 37, 38].

9.4 Discussion

The performed experiments on TiOCl show intense ultrafast signals with a strong dependence on the optical energies and polarizations analyzed, which are a consequence of the complex interplay between different degrees of freedom involved in the material. From the white-light intensity measurements we discriminate two main effects relying respectively on the pump and probe orbital absorption. Furthermore, the examination of the orbital non-equilibrium dynamics with Multimode Heterodyne detection reveals a phonon signature associated to the ISRS Raman interaction inside the probe bandwidth.
In the next paragraphs we briefly discuss the possible physical interpretation of the experimental observations.

9.4.1 Effects of resonant orbital pumping

Selective optical absorption of the NIR d_{xz} orbital transition is associated to the excitation of the electrons in the Ti sites. Therefore, an amount of energy is transferred to the material by these excitation processes, which then relaxes through the non-equilibrium dynamics.

Transient transmittivity modulation

When the pump is absorbed in the orbital transition, in particular if the probe absorption effects are not present, we probe a negative transient transmittivity. In detail, thanks to white-light measurements, we can appreciate that the orbital response is increased in the probe high energy range. This spectral dependence can be described as a modification of the Mott gap. Indeed, considering the temperature

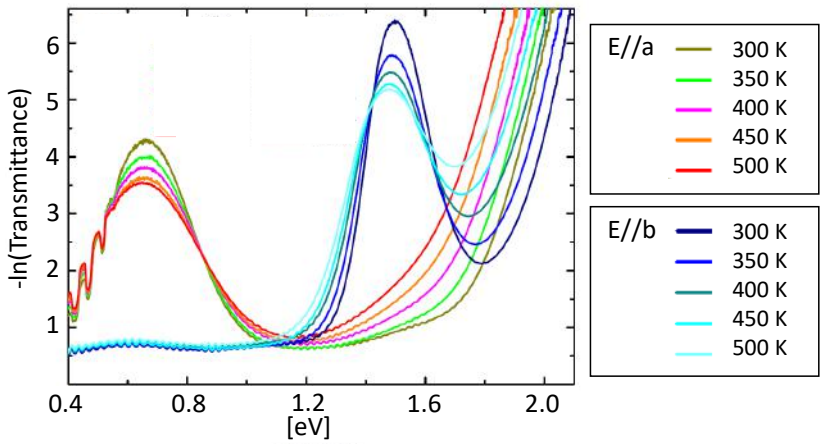

FIGURE 9.15: Temperature dependent equilibrium optical transmittance from [39]. Increasing the temperature shifts the high energy gap towards lower energies and reduces the orbital absorption.

dependence from [39], we see in Fig. 9.15 that the non-equilibrium modulation is

compatible with a thermal rise which lowers the energy of the gap absorption profile.
The analogy with the thermal response suggests the involvement of a similar Mott gap shift, but it does not clarify the interactions responsible for the observed effect. Indeed, any of the orbital, spin and lattice degrees of freedom could have a role in setting the properties of the anisotropic Mott gap [40]. Hence, further studies would be required to define the specific contributions.
In particular, we would be interested in understanding if the direct optical orbital excitation is effective in modifying the anisotropy of the magnetic exchange interaction [41]. In support of this possible research direction, we report that ultrafast responses involving the magnetic degrees of freedom as a consequence of resonant *dd* excitation has been observed in other orbital systems such as iron oxides [17], chromium oxides [18] and manganites [42].

Orbital-phonon coupling

The frequency-resolved detection of the developed Multimode Heterodyne technique is crucial to reveal the excitation of a totalsymmetric coherent phonon mode. The presence of the oscillations is linked to the pump orbital absorption. The electronic perturbation modifies the crystalline potential and drives a displacive excitation mechanism of the vibrational mode [43].
Another remarkable result obtained is the agreement between the damping time of the coherent oscillations and the decay time of the underlying dynamics (Fig. 9.14). Since the oscillations are a phonon signature and the positive time dynamics is related to the orbital excitation, a orbital-phonon coupling is suggested. We recently contributed to a work which demonstrated the orbital effects induced driving a vibrational mode in another Spin-Peierls material [20]. Interestingly, in the present framework we analyze the orbital-phonon coupling the other way around, stimulating the orbital excitation and experiencing a phonon response.

9.4.2 Photo-induced orbital transparency

The other qualitative effect we deduce from the white-light measurements is the positive non-equilibrium response distinguishable when the probe is *b*-polarized and thus absorbed. We can interpret this as an induced transparency in the d_{yz} orbital transition targeted by the probe. The effect is weakly dependent on the pump orbital excitation.
In Fig. 9.15 we see that the transition intensity decreases with temperature because the thermal fluctuations in the lattice tend to re-establish an isotropic environment. This weakens the inversion symmetry breaking, which is instead the condition allowing the optical excitation. If the pump is not strongly absorbed, the framework is similar to that of a transparent material, where we can observe the ISRS excitation of phonons. Even if we don't notice coherent oscillations in this condition, the induced transparency is an indirect evidence of the presence of weak or incoherent lattice excitations which perturb the crystalline structure, adding disorder which re-establishes the not optically active inversion symmetry.

dd transition shift

When the thermal increase is higher because of the orbital absorption, we measure that the probe-orbital effect has a slightly different spectral dependence, which peaks at lower energies (Fig. 9.12a). This is interpreted as an energy shift of the dd transition towards lower energy, which is also experienced in temperature dependent measurements [39, 44]. This results indicates a modification of the crystal field environment which reflects in the d-level splitting.

In conclusion, we observed that orbital and lattice have a key role in determining the ultrafast response in TiOCl. In particular, we highlighted their interplay both in the excitation and probing process.
The direct optical control in TiOCl stimulates an intriguing way to control the magnetic exchange interaction. However, discrimination of the evolution of the spin degrees of freedom would require more dedicated studies. In order to distinguish the magnetic response it would be useful, for example, to measure the optical rotation properties or to follow the temperature dependence in the different magnetic phases.

Chapter 10

Ultrafast dynamics in the high-T_c superconductor YBCO

The superconducting materials with the highest critical temperature at ambient pressure currently belong to the family of cuprates. Despite the efforts in the last decades, the mechanism involved in the emergence of superconductivity in this strongly correlated cooper oxides has not been completely understood yet.
In order to solve the puzzle, spectroscopy experiments have a relevant role. Indeed, the optical properties are strongly modified when entering the superconducting phase. In the traditional superconductors well-described by the BCS theory, the onset of superconductivity is associated to the opening of a gap in the energy conductivity. In standard BCS systems, the changes in the optical properties occur only at energy scales comparable to the superconducting gap. On the contrary, one of the anomalies of high-T_c materials, which is likely associated to the mechanism driving superconductivity in those systems, is the fact that the onset of superconductivity is associated to changes in the optical conductivity up to energies which are 100 times larger than the superconducting gap. In detail, cuprates show modifications of the optical conductivity in the visible range upon entering the superconducting phase [45, 46], which are indicative of a correlation with low-energy physics in the Infrared regime proper of the superconducting gap.
Ultrafast techniques are very useful in this context [14] both to follow the evolution of this indicators at the typical timescale of the fundamental processes involved and to photo-induce non-equilibrium phases. For instance, ultrafast stimulation can be employed to even induce superconductivity [47, 48] by properly coupling to low-energy collective excitations or quenching competing phenomena.

In this chapter, we explore the capabilities which Time-resolved Multimode Heterodyne Detection could bring in order to improve the ultrafast investigation of cuprate superconductors. In particular, we test as an example the widely studied Yttriium Barium Copper Oxide (YBCO).
Firstly, we employ Multimode Heterodyne to reference the pump&probe response at room temperature, observing the coherent phonon dynamics. Afterwards, we study the non-equilibrium dynamics at low temperature, performing measurements across the pseudogap phase down to the superconducting transition. The analysis of phase and amplitude modulations at low temperature, reveals a sample- and phase-specific behavior, which we discuss could be related to charge density order in the pseudogap phase.

10.1 Yttrium Barium Copper Oxide (YBCO)

The first material discovered to be a superconductor above liquid nitrogen boiling point is Yttrium Barium Copper Oxide (YBCO) [49], which in the optimal doping condition has a critical temperature of 92 K.
The general crystalline structure of cuprates is characterized by the presence of copper-oxygen layers. In Fig. 10.1 we represent the $YBa_2Cu_3O_7$ unit cell, where the Cu-O planes are stacked along the c-axis and the inter-layer spaces are occupied by the Y and Ba ions. The electronic correlations between the orbitals of the Cu-O plaquette and the charge from the heavy atoms, together with their interplay with lattice and spin degrees of freedom are allegedly responsible for the intriguing effects occurring in the sample, including superconductivity. Yet an exhausting description of the onset of superconductivity at high critical temperature remains elusive.

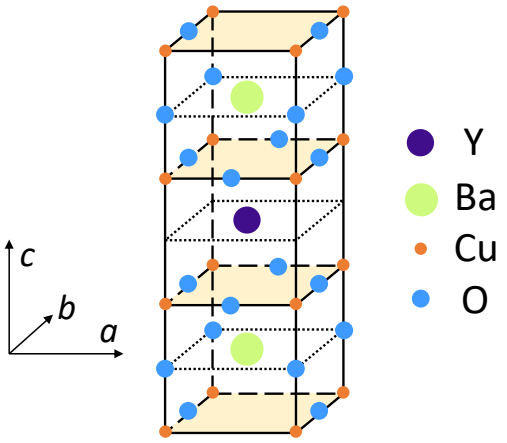

FIGURE 10.1: YBCO crystalline structure. The sample is formed by Cu-O planes stacked along the c-axis. The space between layers is occupied by Y and Ba atoms.

10.1.1 Superconductivity and pseudogap

The rich phenomenology of a cuprate superconductor is usually described in terms of a phase diagram as a function of temperature and doping, as the one sketched in Fig. 10.2a. A comprehensive description of cuprates physics is beyond the scope of this thesis and we introduce here a brief survey of the typical features.
The superconducting character emerges at low-temperature and reaches the highest critical temperature for an optimal value of the oxygen content in the sample, which can be expressed as the doping parameter δ in $YBa_2Cu_3O_{7-\delta}$. In the case of an undoped cuprate, superconductivity does not take place and the compound is an antiferromagnetic insulator. Well above the critical temperature the material is in the so-called 'bad metal' state which presents many anomalies with respect to standard metallic samples. In between the strange metal and superconducting regimes lies the pseudogap phase, which is probably the most mysterious and debated region of the diagram [51].
Whether the pseudogap is a precursor or competing state of superconductivity is still debated. Anyhow, experiments discovered in the pseudogap phase the onset

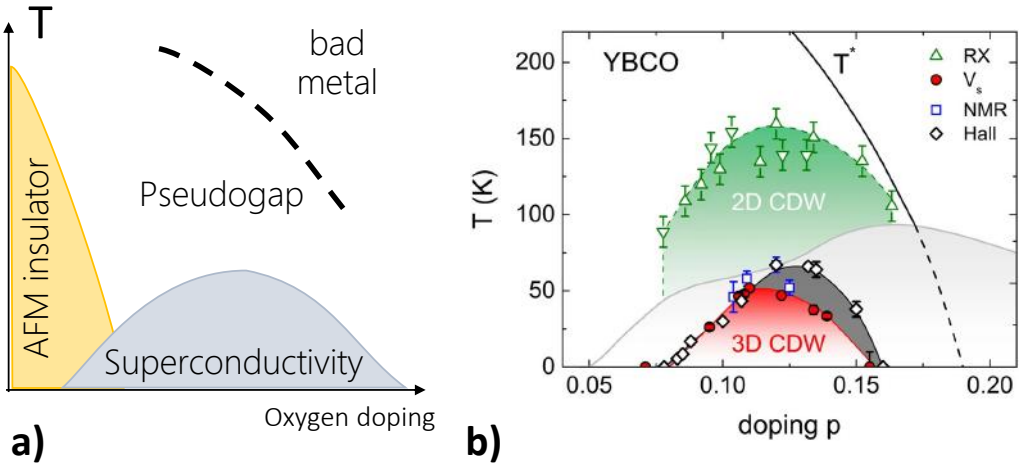

FIGURE 10.2: YBCO phase diagram as a function of temperature and doping. a) Typical phase diagram of a cuprate superconductor. b) Quantitative parameters of YBCO superconducting (light gray dome) and pseudo-gap (below T^* line) phases and associated charge density effects identified with different experimental techniques (from [50]/CC BY).

of charge density order [52, 53]. As reported in Fig. 10.2b [50], charge density effects appear in the most crucial regions of the phase diagram and are likely to be a fundamental ingredient in the comprehension of the cuprates physics.

In the following we assess the possible contributions to the discussion that can result exploring the degrees of freedom accessible with Multimode Heterodyne Detection.

10.2 Ultrafast room temperature dynamics

We start our experimental investigation by measuring the room temperature ultrafast response of YBCO. We collect the transmitted probe pulse. In our studies we employ an optimally doped, 70 nm tick YBCO sample, which has about 60 unit cells grown in the c-direction on a lanthanum aluminate (LAO) substrate (which we reference in appendix A). We perform the pump&probe measurements pumping in the near-infrared (0.75 eV) and probing in the visible range (1.66 eV). The probe has a fluence of about 1 μJ/cm^2. In Fig. 10.3 we test the non-equilibrium modulation of the spectrally integrated intensity for different pump fluences in the 1-10 mJ/cm^2 range.

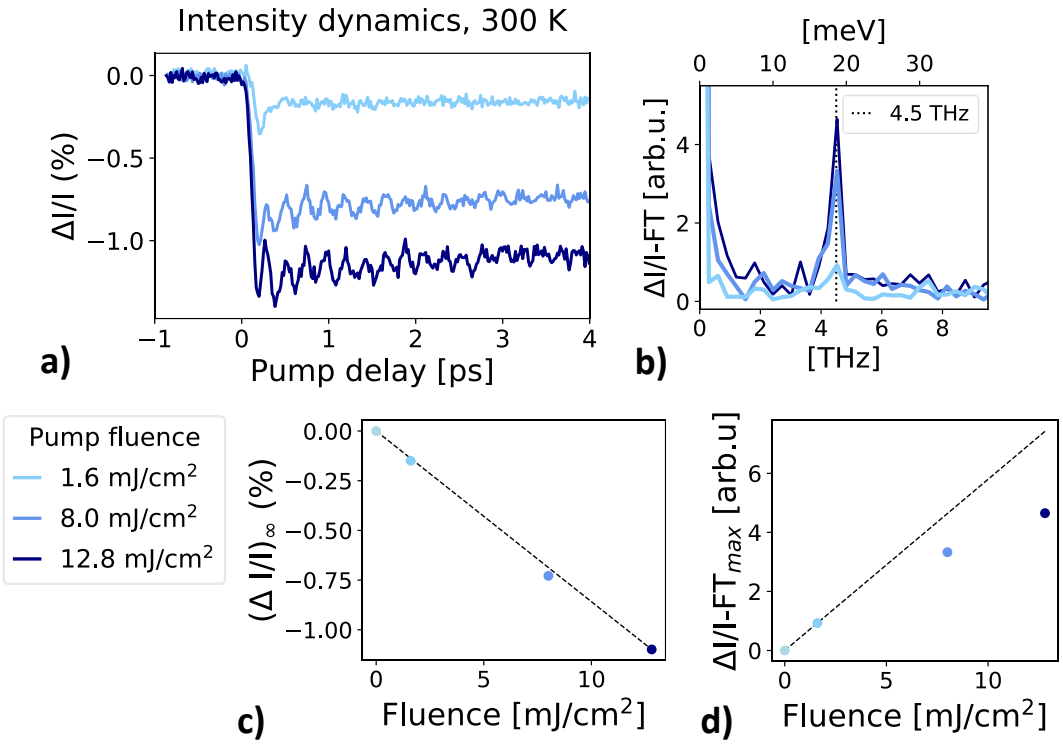

FIGURE 10.3: Room temperature integrated intensity pump&probe studied as a function of the pump fluence. a) Non-equilibrium intensity modulation reveals coherent oscillations in time. b) Fourier Transform analysis of the oscillations identifies a 4.5 THz vibrational mode. c) The negative step of the slow-timescale dynamics depends linearly on the pump fluence. d) The phonon amplitude tends to saturate at high-pump fluences in agreement with [54].

The observed ultrafast dynamics consists of a step-like decrease of the transmittivity, which decays on a very long timescale with respect to the picosecond range analyzed. On top of it, with high pump fluence we can distinguish coherent oscillations. In Fig. 10.3 we perform the Fourier analysis of the modulation and associate it to a 4.5 THz A-symmetry vibrational mode, which involves the displacement of Cu ions along the c-axis [54, 55, 56]. Analyzing the pump fluence dependence, we see that the slow response is linear (Fig. 10.3c), while the amplitude of the phonon oscillation tends to saturate with a strong perturbation (Fig. 10.3d). The trend of the vibrational feature, as suggested in [54], indicates that the excitations are localized at the lattice sites and not representative of a coherent de-localized mode. The present

situation is therefore different with respect to the one studied regarding the coherent phonon in quartz (Chapters 6-7). In the next section, we verify how the dynamics of the optical probe field behaves in this case.

10.2.1 Probe field dynamics via heterodyne detection

We apply Multimode Heterodyne Detection in order to frequency resolve the probe bandwidth and disentangle amplitude and phase effects. The relative spectral maps are shown in Fig. 10.4.

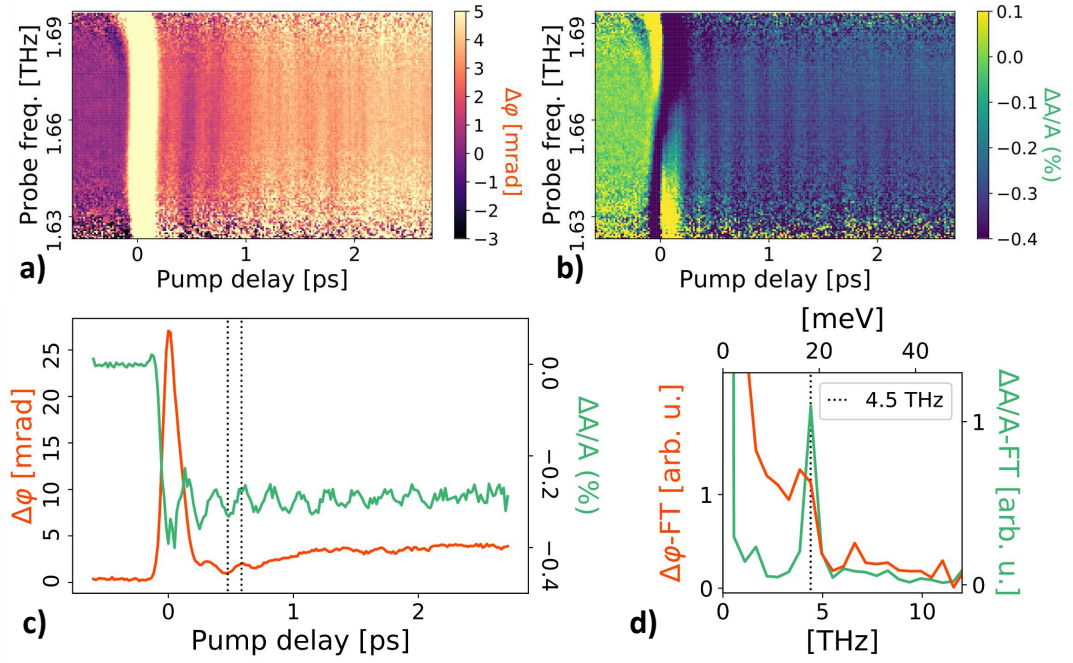

FIGURE 10.4: Room temperature pump&probe heterodyne. a) Frequency-resolved phase dynamics. b) Frequency-resolved amplitude dynamics. c) Spectrally averaged phase and amplitude profiles have qualitatively different responses. The dotted lines underline that phase and amplitude oscillations are in phase. d) Fourier spectrum highlighting the presence of the phonon mode.

We note that amplitude and phase have a different dynamics also in this setting. However, they are both spectrally uniform in the positive times and hence we consider the average spectral response (Fig. 10.4c). The amplitude response reflects the intensity dynamics, while the phase follows a different evolution. For few hundreds of femtoseconds we can distinguish the phonon oscillations also in the phase trace, which we note are in phase with the amplitude ones. On the slower picosecond timescale we observe instead a positive shift of the phase signal.
The spectrally uniform and in-phase amplitude and phase oscillations indicate that the probe is experiencing a modulation of the refractive properties of the sample which does not involve the spectral redistribution typical of Impulsive Stimulated Raman Scattering (ISRS), as discussed for the quartz sample in Chapters 6-7. The ISRS mechanism dominates the interaction in the transparency regime, while other effects associated to the dissipation of absorbed energy are relevant in absorptive systems like YBCO. In this framework, the phonon excitation is generally retained

owing to the displacive mechanism [43] generated by the perturbation of the electronic landscape after the optical absorption. In this connection, the slow incoherent contribution is likely a thermal response due to the absorption in the material.

10.2.2 Coherent control of vibrational excitation

We noted in the previous experiments the localized nature of the phonon excitation and its displacive origin. In order to discriminate the coherent and incoherent dynamics in this setting we perform coherent control measurements. We setup a double-pump experiment and tune the temporal separation between the two similar optical perturbations.

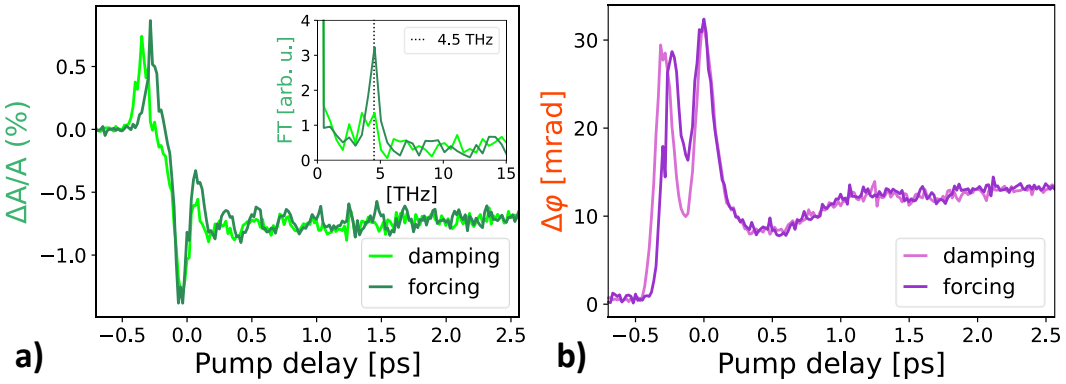

FIGURE 10.5: Coherent control of the vibrational mode. We study the heterodyne response tuning the two-pumps delay in both phonon damping and forcing condition. In this example we select respectively a separation of 1.5 and 1 phonon periods. a) Spectrally averaged amplitude profile. FT-spectrum in insert. The amplitude of the phonon oscillations is modulated by the coherent control, while the slow step dynamics is not affected and due to incoherent processes. b) The average phase profile is weakly sensitive to phonon oscillations. The positive time response is representative of an incoherent dynamics and not perturbed by the coherent control.

We can exert a coherent control of the vibrational oscillation modifying the delay of the first pump. In Fig. 10.5 we report the measurement performed in both damping and forcing condition of the single-pump signal. We adjust the arrival time of the first pump. In the damping condition the delay between the two pumps is 0.33 ps (1.5 phonon periods), corresponding to an half-integer cycle of the phonon oscillation (π phase shift). The forcing is achieved with 0.22 ps delay (1 phonon cycle), when the pump separation is an integer multiple of the phonon period (2π-shift). The modulation of the phonon oscillation dependent on the coherent control is evident in the amplitude response (Fig. 10.5a). The resulting phase signal (Fig. 10.5b) instead is not sensitive to the temporal separation between the two pumps. This indicates that the slow timescale dynamics is likely an incoherent superposition of the effects of the two pumps. As a consequence of this, we understand that in a complex absorptive system, even if the coherent oscillation can be quenched, coherent control is not able to restore the equilibrium state and dissipative and decoherence processes have a relevant role.

10.3 Temperature dependent studies

After having referenced the room temperature response, we are ready to explore the more interesting regions of the YBCO phase diagram. We exploit a nitrogen cooled cryostat to measure the optimally doped YBCO sample at the temperatures typical of the pseudogap and superconducting phase.

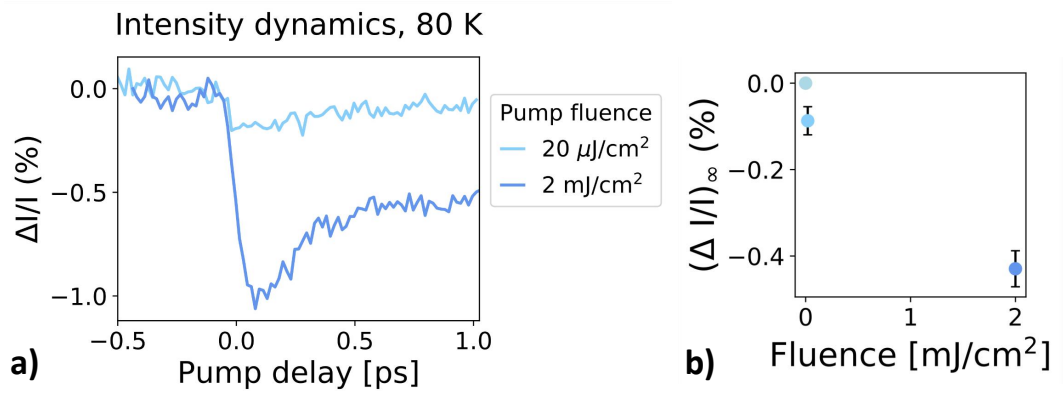

FIGURE 10.6: Low temperature (80 K) integrated intensity dynamics as a function of the pump fluence. a) Non-equilibrium modulation. b) Fluence dependence of the step signal at positive times indicates a strong non-linear behaviour.

At first we study the dynamics of the probe integrated intensity. In Fig. 10.6 we report the non-equilibrium response at 80 K as a function of the pump fluence. We employ a lower fluence range in order to reduce the perturbative effects and avoid, for instance, thermal melting of the superconducting phase.
The non-equilibrium response at low temperature is still a negative modulation of the transmitted intensity, but the fluence dependence is not linear (Fig. 10.6b), suggesting a critical behavior.
In order to verify if the non-equilibrium response is sensitive to the different phases

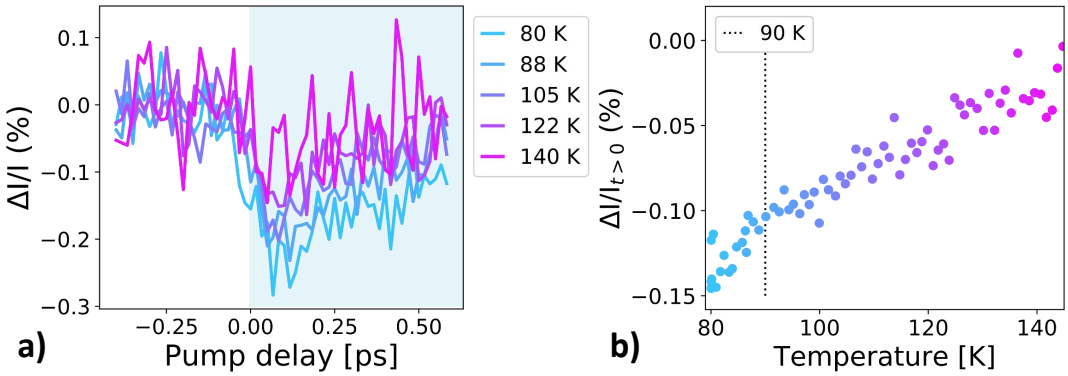

FIGURE 10.7: Temperature integrated intensity pump&probe. a) Non-equilibrium response as a function of temperature. The modulation signal vanishes with increasing temperature. b) Temperature trend of the average positive time response (highlighted in (a)). The dotted line suggest the presence of a kink around 90 K, whereby we expect to find T_c for an optimally doped sample.

of the system, we test the temperature dependence in the less perturbative pump regime. We explore the range corresponding to the pseudogap phase and the critical temperature of the superconducting transition. The results are presented in Fig. 10.7. The negative modulation is enhanced with decreasing temperature. Also a change in the relaxation time is expected [57]. The present measurements have a low signal-to-noise ratio which does not allow for precise analysis of the decay profile. Nevertheless, we account for the relative effects considering the average on the positive times interval (highlighted in Fig. 10.7a). The temperature dependence of the latter observable (Fig. 10.7a) reports that the non-equilibrium modulation vanishes heating the sample. Moreover, we observe the hint of a kink around 90 K, compatible with the expected superconducting critical temperature for optimally doped YBCO.

These preliminary measurements showed that the ultrafast dynamics is sensitive to the different phases ruled by the temperature. In the following, we deepen the investigation focusing on the phase observable accessible with heterodyne detection, which reveals a non trivial behavior.

10.3.1 Anomalous low-temperature field dynamics

We examine the optical field response with the aim of disentangling amplitude and phase dynamics and revealing features specific of the low-temperature phases. We perform Multimode Heterodyne pump&probe measurements with two pump fluences and report the resulting spectral maps in Fig. 10.8.
We detect also in this case spectrally uniform modulations. The amplitude as usual reflects the intensity response. The phase dynamics measures instead a peculiar negative shift of the spectral phase. This reveals a reduction in the probe propagation time as a consequence of the pump photo-excitation. The measurement at higher fluence underlines also that the signal is composite. We distinguish a positive and fast contribution, likely due to the optical overlap between pump and probe, together with a slower and negative modulation.

In order to correlate the observed dynamics to the system phase, we analyze the temperature dependence with the low 20 μJcm^2 pump fluence. We display the data for three different temperatures in Fig. 10.9.
The observed field dynamics is reduced increasing the temperature. Precisely, the fast positive shift in the phase response is rising, but it could be an effect of a reduced contribution from the negative component. Importantly, we record that the negative phase shift is not disappearing over the critical temperature and still present in the pseudogap phase. Further studies would be required in order to define the onset temperature of the considered effect.

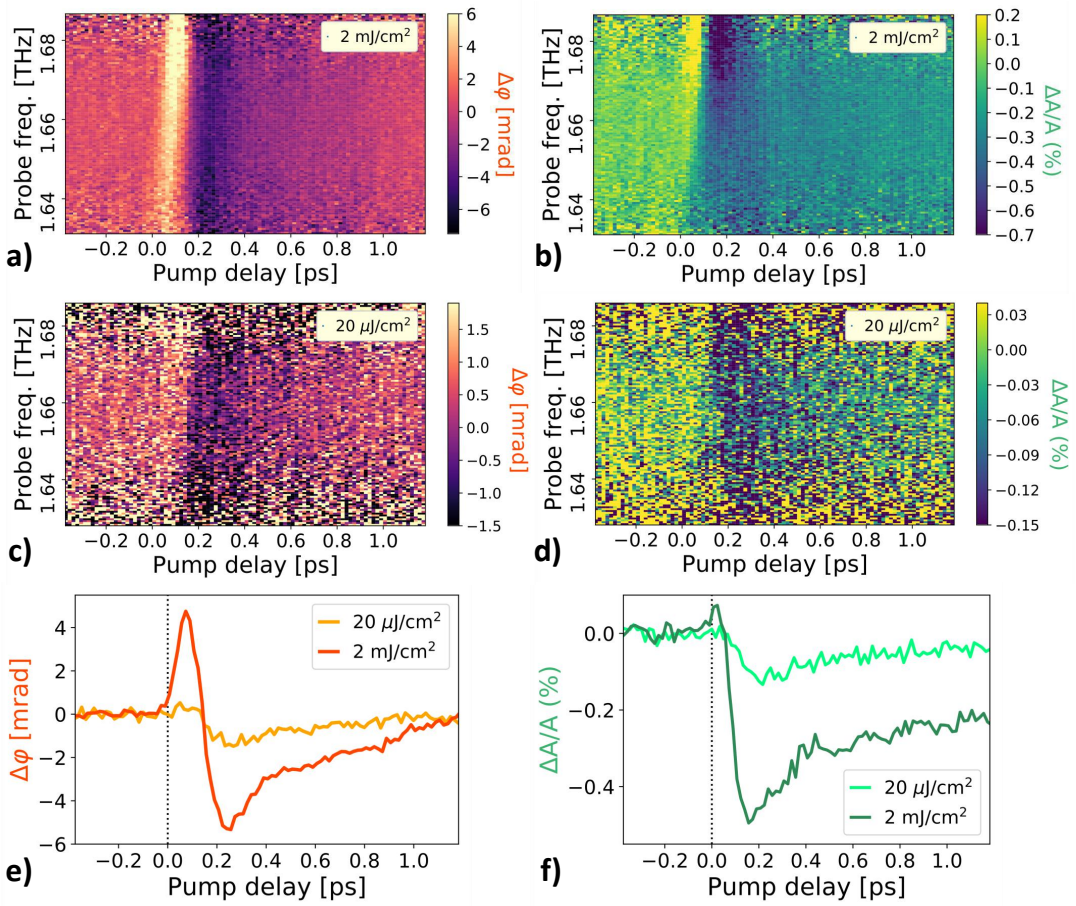

FIGURE 10.8: Low temperature pump&probe heterodyne. We study the response with two different pump fluences. The amplitude modulation agrees with the intensity one. Regarding the phase we reveal a peculiar negative phase modulation. a),b) Frequency-resolved phase and amplitude dynamics for high pump fluence. c),d) Low fluence. e) Comparison of spectrally averaged phase profiles for different fluences. f) Same for amplitude profiles.

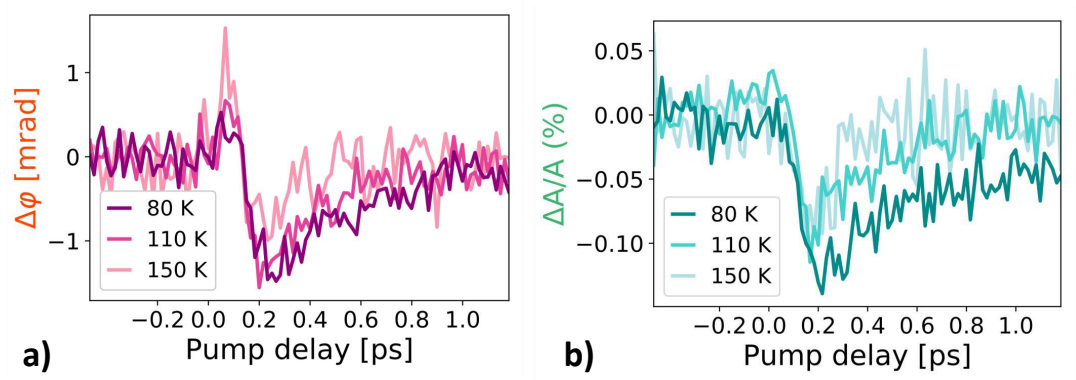

FIGURE 10.9: Temperature dependent pump&probe heterodyne. We study the low-pump response across a temperature interval corresponding to the superconducting transition and the pseudogap phase. The observed negative modulations vanish with increasing temperature. a) Average spectral phase profile. b) Average spectral amplitude profile.

10.3.2 Discussion

We highlight the anomalous negative phase shift as result peculiar of the cuprates. In all the other samples and configurations studied in this thesis we observe that the pump photoexcitation is associated to a positive probe phase shift. In detail, we always measured a positive response in the overlap signals and in the slow timescale thermal steps. We reported another negative phase signal only in the case of quartz, whereby the phonon causes a phase oscillation around zero. This suggests the possibility that also the low-temperature effect in YBCO has a coherent nature.
This photo-induced reduction of the probe propagation time can be described assuming either a decreasing of the sample refractive index or length, which is not common. The optical pump absorption can often result in an increase of the thermal energy, which would induce a sample dilation and slow-down the propagation velocity. Moreover, this is usually associated to a slow dynamics lasting many picoseconds. The latter framework is likely the one observed in TiOCl and room temperature YBCO.
The low-temperature field effects must have instead a different origin. Nevertheless, it is interesting to consider the temperature dependent expansion also in this discussion. Indeed, there exist many examples of materials which in certain conditions contract their dimensions with increasing temperature, like water for instance, and this attribute is dubbed anomalous expansion coefficient. Remarkably, this property is reported to be present in the superconducting phase of many cuprate and non-cuprate samples [58, 59, 60, 61]. YBCO shows as well the anomalous expansion coefficient in the superconducting phase [62] and we hypothesize a link between the ultrafast negative phase shift and the peculiar dilation effect.
Interestingly, the negative expansion coefficient in high-temperature superconductors has been associated by A. I. Golovashkin and A. P. Rusakov [63] to the presence of charge density waves. This element represents a very intriguing factor taking into account the correlation between charge density order and the critical regions of the YBCO phase diagram (Fig. 10.2b). We propose that the observed anomalous phase dynamics could be a signature of charge density waves in the superconducting and pseudogap phase.

In conclusion, we applied Time-resolved Multimode Heterodyne Detection in the study of the low-temperature complex phases in YBCO and revealed that accessing the phase degree of freedom of the optical probe field allows us to discriminate information which eludes amplitude and intensity response. Interestingly, we discuss the possible connection of the observed effect with the presence of charge density order, which is a key ingredient to address in order to understand the mechanisms ruling the high-temperature superconductors. Further studies will be necessary to give fundament to this interesting scenario.

References - part III

[1] B. Keimer and J. E. Moore. "The physics of quantum materials". *Nature Physics* 13 (2017).

[2] F. Giustino, M. Bibes, J. H. Lee, F. Trier, R. Valentí, S. M. Winter, Y.-W. Son, L. Taillefer, C. Heil, A. I. Figueroa, B. Plaçais, Q. Wu, O. V. Yazyev, E. P. A. M. Bakkers, J. Nygård, P. Forn-Díaz, S. de Franceschi, L. E. F. F. Torres, J. McIver, A. Kumar, T. Low, R. Galceran, S. O. Valenzuela, M. V. Costache, A. Manchon, E.-A. Kim, G. R. Schleder, A. Fazzio, and S. Roche. "The 2020 Quantum Materials Roadmap". *Journal of Physics: Materials* (2020).

[3] D. Basov, R. Averitt, and D. Hsieh. "Towards properties on demand in quantum materials". *Nature Mater* 16 (2017).

[4] Y. Tokura. "Correlated-Electron Physics in Transition-Metal Oxides". *Physics Today* 56 (2003).

[5] D. N. Basov, R. D. Averitt, D. van der Marel, M. Dressel, and K. Haule. "Electrodynamics of correlated electron materials". *Rev. Mod. Phys.* 83 (2011).

[6] Y. Tokura and N. Nagaosa. "Orbital Physics in Transition-Metal Oxides". *Science* 288.5465 (2000).

[7] A. M. Oleś. "Fingerprints of spin–orbital entanglement in transition metal oxides". *Journal of Physics: Condensed Matter* 24.31 (2012).

[8] H. Capellmann. "The magnetism of iron and other 3-d transition metals". *Journal of Magnetism and Magnetic Materials* 28.3 (1982).

[9] A. Vasiliev, O. Volkova, E. Zvereva, and M. Markina. "Milestones of low-D quantum magnetism". *npj Quantum Materials* 3 (2018).

[10] E. Dagotto. "Correlated electrons in high-temperature superconductors". *Rev. Mod. Phys.* 66 (1994).

[11] K. M. Shen and J. S. Davis. "Cuprate high-Tc superconductors". *Materials Today* 11.9 (2008).

[12] J. Orenstein. "Ultrafast spectroscopy of quantum materials". *Physics Today* 65 (2012).

[13] J. Zhang and R. Averitt. "Dynamics and Control in Complex Transition Metal Oxides". *Annual Review of Materials Research* 44.1 (2014).

[14] C. Giannetti, M. Capone, D. Fausti, M. Fabrizio, F. Parmigiani, and D. Mihailovic. "Ultrafast optical spectroscopy of strongly correlated materials and high-temperature superconductors: a non-equilibrium approach". *Advances in Physics* 65.2 (2016).

[15] M. Hase, I. Terasaki, and K. Uchinokura. "Observation of the spin-Peierls transition in linear Cu^{2+} (spin-1/2) chains in an inorganic compound $CuGeO_3$". *Phys. Rev. Lett.* 70 (1993).

[16] M. Shaz, S. van Smaalen, L. Palatinus, M. Hoinkis, M. Klemm, S. Horn, and R. Claessen. "Spin-Peierls transition in TiOCl". *Phys. Rev. B* 71 (2005).

[17] R. V. Mikhaylovskiy, T. J. Huisman, V. A. Gavrichkov, S. I. Polukeev, S. G. Ovchinnikov, D. Afanasiev, R. V. Pisarev, T. Rasing, and A. V. Kimel. "Resonant Pumping of $d-d$ Crystal Field Electronic Transitions as a Mechanism of Ultrafast Optical Control of the Exchange Interactions in Iron Oxides". *Phys. Rev. Lett.* 125 (2020).

[18] V. G. Sala, S. Dal Conte, T. A. Miller, D. Viola, E. Luppi, V. Véniard, G. Cerullo, and S. Wall. "Resonant optical control of the structural distortions that drive ultrafast demagnetization in Cr_2O_3". *Phys. Rev. B* 94 (2016).

[19] J. van den Brink. "Orbital Excitations in $LaMnO_3$". *Phys. Rev. Lett.* 87 (2001).

[20] A. Marciniak, S. Marcantoni, F. Giusti, F. Glerean, G. Sparapassi, T. Nova, A. Cartella, S. Latini, F. Valiera, A. Rubio, J. van den Brink, F. Benatti, and D. Fausti. "Vibrational coherent control of localized d–d electronic excitation". *Nature Physics* (2021).

[21] R. Rückamp, E. Benckiser, M. W. Haverkort, H. Roth, T. Lorenz, A. Freimuth, L. Jongen, A. Möller, G. Meyer, P. Reutler, B. Büchner, A. Revcolevschi, S.-W. Cheong, C. Sekar, G. Krabbes, and M. Grüninger. "Optical study of orbital excitations in transition-metal oxides". *New Journal of Physics* 7 (2005).

[22] S. Glawion, J. Heidler, M. W. Haverkort, L. C. Duda, T. Schmitt, V. N. Strocov, C. Monney, K. J. Zhou, A. Ruff, M. Sing, and R. Claessen. "Two-Spinon and Orbital Excitations of the Spin-Peierls System TiOCl". *Phys. Rev. Lett.* 107 (2011).

[23] V. Kataev, J. Baier, A. Möller, L. Jongen, G. Meyer, and A. Freimuth. "Orbital order in the low-dimensional quantum spin system TiOCl probed by ESR". *Phys. Rev. B* 68 (2003).

[24] T. C. Ozawa and S. J. Kang. "*Balls*&*Sticks*: easy-to-use structure visualization and animation program". *Journal of Applied Crystallography* 37.4 (2004).

[25] M. Hoinkis, M. Sing, J. Schäfer, M. Klemm, S. Horn, H. Benthien, E. Jeckelmann, T. Saha-Dasgupta, L. Pisani, R. Valentí, and R. Claessen. "Electronic structure of the spin-$\frac{1}{2}$ quantum magnet TiOCl". *Phys. Rev. B* 72 (2005).

[26] A. Seidel, C. A. Marianetti, F. C. Chou, G. Ceder, and P. A. Lee. "$S = \frac{1}{2}$ chains and spin-Peierls transition in TiOCl". *Phys. Rev. B* 67 (2003).

[27] Y.-Z. Zhang, H. O. Jeschke, and R. Valentí. "Microscopic model for transitions from Mott to spin-Peierls insulator in TiOCl". *Phys. Rev. B* 78 (2008).

[28] D. Mastrogiuseppe and A. Dobry. "Microscopic theory for the incommensurate transition in TiOCl". *Phys. Rev. B* 79 (2009).

[29] A. Schönleber, S. van Smaalen, and L. Palatinus. "Structure of the incommensurate phase of the quantum magnet TiOCl". *Phys. Rev. B* 73 (2006).

[30] P. Lemmens, K. Y. Choi, G. Caimi, L. Degiorgi, N. N. Kovaleva, A. Seidel, and F. C. Chou. "Giant phonon softening in the pseudogap phase of the quantum spin system TiOCl". *Phys. Rev. B* 70 (2004).

[31] R. Macovez, J. Luzon, J. Schiessling, A. Sadoc, L. Kjeldgaard, S. van Smaalen, D. Fausti, P. H. M. van Loosdrecht, R. Broer, and P. Rudolf. "Hybridization, superexchange, and competing magnetoelastic interactions in TiOBr". *Phys. Rev. B* 76 (2007).

[32] N. A. Bogdanov, J. van den Brink, and L. Hozoi. "Ab initio computation of *d-d* excitation energies in low-dimensional Ti and V oxychlorides". *Phys. Rev. B* 84 (2011).

[33] R. Kraus, B. Büchner, M. Knupfer, S. Glawion, M. Sing, and R. Claessen. "Anisotropic crystal field, Mott gap, and interband excitations in TiOCl: An electron energy-loss study". *Phys. Rev. B* 81 (2010).

[34] S. Ishihara. "Photoinduced Ultrafast Phenomena in Correlated Electron Magnets". *Journal of the Physical Society of Japan* 88.7 (2019).

[35] J. H. Mentink. "Manipulating magnetism by ultrafast control of the exchange interaction". *Journal of Physics: Condensed Matter* 29.45 (2017).

[36] D. Fausti, T. T. A. Lummen, C. Angelescu, R. Macovez, J. Luzon, R. Broer, P. Rudolf, P. H. M. van Loosdrecht, N. Tristan, B. Büchner, S. van Smaalen, A. Möller, G. Meyer, and T. Taetz. "Symmetry disquisition on the TiOX phase diagram ($X = \mathrm{Br}, \mathrm{Cl}$)". *Phys. Rev. B* 75 (2007).

[37] L. Pisani and R. Valentí. "Ab initio phonon calculations for the layered compound TiOCl". *Phys. Rev. B* 71 (2005).

[38] L. Pisani, R. Valentí, B. Montanari, and N. M. Harrison. "Density functional study of the electronic and vibrational properties of TiOCl". *Phys. Rev. B* 76 (2007).

[39] R. Rückamp. "Orbital excitations of transition-metal oxides in optical spectroscopy". PhD thesis. Universität zu Köln, 2006.

[40] S. Miyasaka, Y. Okimoto, and Y. Tokura. "Anisotropy of Mott–Hubbard Gap Transitions due to Spin and Orbital Ordering in LaVO3 and YVO3". *Journal of the Physical Society of Japan* 71.9 (2002).

[41] D. V. Zakharov, J. Deisenhofer, H.-A. Krug von Nidda, P. Lunkenheimer, J. Hemberger, M. Hoinkis, M. Klemm, M. Sing, R. Claessen, M. V. Eremin, S. Horn, and A. Loidl. "Spin dynamics in the low-dimensional magnet TiOCl". *Phys. Rev. B* 73 (2006).

[42] Z. Jin, H. Ma, G. Li, Y. Xu, G. Ma, and Z. Cheng. "Ultrafast dynamics of the Mn^{3+} d-d transition and spin-lattice interaction in $YMnO_3$ film". *Applied Physics Letters* 100.2 (2012).

[43] H. J. Zeiger, J. Vidal, T. K. Cheng, E. P. Ippen, G. Dresselhaus, and M. S. Dresselhaus. "Theory for displacive excitation of coherent phonons". *Phys. Rev. B* 45 (1992).

[44] C. A. Kuntscher, A. Pashkin, H. Hoffmann, S. Frank, M. Klemm, S. Horn, A. Schönleber, S. van Smaalen, M. Hanfland, S. Glawion, M. Sing, and R. Claessen. "Mott-Hubbard gap closure and structural phase transition in the oxyhalides TiOBr and TiOCl under pressure". *Phys. Rev. B* 78 (2008).

[45] H. J. A. Molegraaf, C. Presura, D. van der Marel, P. H. Kes, and M. Li. "Superconductivity-Induced Transfer of In-Plane Spectral Weight in $Bi_2Sr_2CaCu_2O_{8+\delta}$". *Science* 295.5563 (2002).

[46] S. L. Cooper, D. Reznik, A. Kotz, M. A. Karlow, R. Liu, M. V. Klein, W. C. Lee, J. Giapintzakis, D. M. Ginsberg, B. W. Veal, and A. P. Paulikas. "Optical studies of the a-, b-, and c-axis charge dynamics in $YBa_2Cu_3O_{6+x}$". *Phys. Rev. B* 47 (1993).

[47] D. Fausti, R. I. Tobey, N. Dean, S. Kaiser, A. Dienst, M. C. Hoffmann, S. Pyon, T. Takayama, H. Takagi, and A. Cavalleri. "Light-Induced Superconductivity in a Stripe-Ordered Cuprate". *Science* 331.6014 (2011).

[48] S. Kaiser. "Light-induced superconductivity in high-T_c cuprates". *Physica Scripta* 92.10 (2017).

[49] M. K. Wu, J. R. Ashburn, C. J. Torng, P. H. Hor, R. L. Meng, L. Gao, Z. J. Huang, Y. Q. Wang, and C. W. Chu. "Superconductivity at 93 K in a new mixed-phase Y-Ba-Cu-O compound system at ambient pressure". *Phys. Rev. Lett.* 58 (1987).

[50] F. Laliberté, M. Frachet, S. Benhabib, B. Borgnic, T. Loew, J. Porras, M. Le Tacon, B. Keimer, S. Wiedmann, C. Proust, and D. LeBoeuf. "High field charge order across the phase diagram of $YBa_2Cu_3O_y$". *npj Quantum Materials* 3 (2018).

[51] E. Fradkin and S. A. Kivelson. "Ineluctable complexity". *Nature Physics* 8.12 (2012).

[52] G. Ghiringhelli, M. Le Tacon, M. Minola, S. Blanco-Canosa, C. Mazzoli, N. B. Brookes, G. M. De Luca, A. Frano, D. G. Hawthorn, F. He, T. Loew, M. M. Sala, D. C. Peets, M. Salluzzo, E. Schierle, R. Sutarto, G. A. Sawatzky, E. Weschke, B. Keimer, and L. Braicovich. "Long-Range Incommensurate Charge Fluctuations in $(Y,Nd)Ba_2Cu_3O_{6+x}$". *Science* 337.6096 (2012).

[53] J. Chang, E. Blackburn, A. T. Holmes, N. B. Christensen, J. Larsen, J. Mesot, R. Liang, D. A. Bonn, W. N. Hardy, A. Watenphul, M. v. Zimmermann, E. M. Forgan, and S. M. Hayden. "Direct observation of competition between superconductivity and charge density wave order in $YBa_2Cu_3O_{6.67}$". *Nature Physics* 8 (2012).

[54] F. Novelli, G. Giovannetti, A. Avella, F. Cilento, L. Patthey, M. Radovic, M. Capone, F. Parmigiani, and D. Fausti. "Localized vibrations in superconducting $YBa_2Cu_3O_7$ revealed by ultrafast optical coherent spectroscopy". *Phys. Rev. B* 95 (2017).

[55] C. Thomsen and G. Kaczmarczyk. "Vibrational Raman Spectroscopy of High-temperature Superconductors". *Handbook of Vibrational Spectroscopy*. American Cancer Society, 2006. ISBN: 9780470027325.

[56] A. Ramos-Alvarez, N. Fleischmann, L. Vidas, A. Fernandez-Rodriguez, A. Palau, and S. Wall. "Probing the lattice anharmonicity of superconducting $YBa_2Cu_3O_{7-\delta}$ via phonon harmonics". *Phys. Rev. B* 100 (2019).

[57] R. D. Averitt, G. Rodriguez, A. I. Lobad, J. L. W. Siders, S. A. Trugman, and A. J. Taylor. "Nonequilibrium superconductivity and quasiparticle dynamics in $YBa_2Cu_3O_{7-\delta}$". *Phys. Rev. B* 63 (2001).

[58] A. Golovashkin, N. Anshukova, L. Ivanova, I. Krinetskii, and A. Rusakov. "Strong influence of magnetic field on the thermal expansion anomaly in $La_{8-x}Sr_xCuO_4$ and $Ba_{1-x}K_xBiO_3$ systems". *Physica C: Superconductivity* 341-348 (2000).

[59] N. V. Anshukova, A. I. Golovashkin, L. I. Ivanova, I. B. Krynetskiĭ, and A. P. Rusakov. "Anomalous thermal expansion of high-temperature superconductors $Bi_2Sr_{2-x}La_xCuO_6$ at low temperatures". *Physics of the Solid State* 48 (2006).

[60] B. M. Anshukova N. V.and Bulychev, A. I. Golovashkin, L. I. Ivanova, I. B. Krynetskii, A. A. Minakov, and A. P. Rusakov. "Anomalous low-temperature behavior of the thermal characteristics of MgB_2". *Journal of Experimental and Theoretical Physics* 97 (2003).

[61] J. J. Neumeier, T. Tomita, M. Debessai, J. S. Schilling, P. W. Barnes, D. G. Hinks, and J. D. Jorgensen. "Negative thermal expansion of MgB_2 in the superconducting state and anomalous behavior of the bulk Grüneisen function". *Phys. Rev. B* 72 (2005).

[62] H. You, U. Welp, and Y. Fang. "Slope discontinuity and fluctuation of lattice expansion near T_c in untwinned $YBa_2Cu_3O_{7-\delta}$ single crystals". *Phys. Rev. B* 43 (1991).

[63] A. I. Golovashkin and A. P. Rusakov. "Anomalous thermal expansion of high-temperature superconductors at low temperatures". *Physics of the Solid State* 49 (2007).

Chapter 11

Conclusion

The intriguing and puzzling features of complex quantum materials are investigated at their fundamental timescales by means of ultrafast spectroscopy techniques. These rely on ultrashort laser pulses which provide a time-resolution on the femtosecond scale. The common approach is the pump&probe one, in which a first intense pump pulse triggers a non-equilibrium excitation while the not perturbative probe is measured as a function of the delay between the two pulses to monitor the de-excitation. The insights about the material are then deduced analyzing the signatures of the light-matter interaction in the probe pulse.
In order to reveal the most possible amount of the information written in the optical pulse, we propose Time-resolved Multimode Heterodyne Detection. Our goal is to go beyond the standard detection of the probe mean value intensity and reconstruct the full quantum state of the examined light. In this way, we access also the field phase and statistical fluctuations which are a consequence of the intimate wave and particle natures of light.

In this doctoral thesis we present the Time-resolved Multimode Heterodyne Detection method and analyze its potentialities studying the non-equilibrium response in three different typologies of materials.
The core of the thesis studies the details of prototypical light-phonon interaction in transparent materials, such as quartz, while in the last part we explore the potentialities to discover new effects in complex materials. In particular, we investigate the magnetic insulator TiOCl and the high temperature superconductor YBCO.

The first part of the dissertation introduces the developed technique. We describe the theoretical formalism regarding the optical quantum state reconstruction method and the associated experimental implementation through balanced heterodyne detection. Since we are dealing with ultrashort pulses with a wide spectral content, we take into particular account the multimode treatment.
We characterize the spectral quadratures of the employed coherent probe pulses and verify that we are sensitive to the quantum limited fluctuations. Importantly, we compare the noise levels achieved with a fast parallel multichannel detection and a low-noise single-channel acquisition. We underline that the use of a low-noise differential detector is crucial to achieve high quality performance (measuring the shot noise with uncertainty of few percent) and the adoption of pulse shaping of the Local Oscillator beam is key to achieve frequency resolution in this configuration.

Application of Time-resolved Multimode Heterodyne Detection to the ultrafast investigation of materials allows us to monitor the evolution of non-equilibrium femtosecond dynamics. We start studying the coherent vibrational excitations in transparent quartz. It is a benchmark material without other electronic responses,

which is suitable to examine the general attributes of coherent excitation of phonons. We model and measure the dynamics triggered by Impulsive Stimulated Raman Scattering (ISRS) processes. We develop a fully quantum description of the interaction which is consistent with our quantum detection. We highlight that amplitude and phase responses are different and they are indicative of momentum and position dependent interactions. The position sets the spectral independent modulation of the refractive properties, while the momentum rules the spectral dependent energy exchanges between matter and radiation. Moreover, we underline the non-linear character of the interaction between different frequency-modes, which imprints correlations in the multimode state owing to the Raman interaction. We reveal them in a classical intensity experiment and discuss the possible strategies to detect them in the quantum regime.

When we extend our approach to more complex materials we find other interesting insights in the phase degrees of freedom. We see that the typical phonon response discussed in quartz is retrieved, but other specific phase dynamics arise owing to the increased complexity of the considered samples.

In TiOCl we find a dynamics strongly dependent on the *dd* orbital absorption of the pump. Thanks to the measurement of the multimode field, we identify the ISRS signature in analogy with the quartz case. Therefore, we associate a phonon response to the orbital dependence, revealing coupling between orbital and vibrational degrees of freedom in the sample.

In YBCO we observe a striking dependence of the phase response as a function of temperature. In the room temperature experiment we report dynamical responses similar to what observed in the other samples. We see coherent oscillations and a slow-timescale positive shift of the phase, which is probably due to a thermal effect. Lowering the temperature to reach the intriguing pseudogap and superconducting phases, we see instead an anomalous negative transient in the phase response. This signals a photoinduced decreasing of the propagation time of light through the sample. We discuss this specific phase dynamics establishing a link with anomalous thermal dilation, which in turn is correlated to charge density wave physics. Thus, we open the possibility to reveal details of the ultrafast charge dynamics in high temperature superconductors by means of heterodyne spectroscopy.

To sum up, in the performed experiments we verified in different contexts the advantages of accessing the optical phase. In perspective we highlight that also the potentialities linked to the statistical degrees of freedom could represent a wide field to explore. Statistical properties like fluctuations and inhomogeneity have a relevant role in critical systems and we aim to map them in the photon distribution.
In this direction, in addition to the analysis with coherent states, we suggest the possible impact of performing experiments with probe light with peculiar statistical features. Among these, we remind for instance the phase-randomized states characterized in this thesis, which could be suitable to study the phase independent photon number statistics.

In conclusion, in this dissertation we propose an evolution of the standard ultrafast methodology and show that the new observables provided by Time-resolved Heterodyne Detection can be an insightful tool to access new information to be processed in the study of complex materials.

List of publications

- F. **Glerean**, G. Jarc, A. Marciniak, F. Giusti, G. Sparapassi, A. Montanaro, E. M. Rigoni, J. O. Tollerud, and D. Fausti. "Time-resolved multimode heterodyne detection for dissecting coherent states of matter". *Opt. Lett.* 45.13 (2020), pp. 3498–3501
- F. **Glerean**, S. Marcantoni, G. Sparapassi, A. Blason, M. Esposito, F. Benatti, and D. Fausti. "Quantum model for impulsive stimulated Raman scattering". *Journal of Physics B: Atomic, Molecular and Optical Physics* 52.14 (2019), p. 145502
- A. Marciniak, S. Marcantoni, F. Giusti, F. **Glerean**, G. Sparapassi, T. Nova, A. Cartella, S. Latini, F. Valiera, A. Rubio, J. van den Brink, F. Benatti, and D. Fausti. "Vibrational coherent control of localized d–d electronic excitation". *Nature Physics* (2021)
- A. Montanaro, F. Giusti, M. Colja, G. Brajnik, A. M. A. Marciniak, R. Sergo, D. De Angelis, F. **Glerean**, G. Sparapassi, G. Jarc, S. Carrato, G. Cautero, and D. Fausti. "Visible pump–mid infrared pump–broadband probe: Development and characterization of a three-pulse setup for single-shot ultrafast spectroscopy at 50 kHz". *Review of Scientific Instruments* 91.7 (2020), p. 073106
- J. O. Tollerud, G. Sparapassi, A. Montanaro, S. Asban, F. **Glerean**, F. Giusti, A. Marciniak, G. Kourousias, F. Billè, F. Cilento, S. Mukamel, and D. Fausti. "Femtosecond covariance spectroscopy". *Proceedings of the National Academy of Sciences* 116.12 (2019), pp. 5383–5386

Appendix A

Characterization of LAO substrate

We report the characterization of the bare $LaAlO_3$ (LAO) substrate employed in the YBCO measurements (Chapter 10). We perform acquisitions in the same conditions discussed for YBCO, in order to exclude that the observed features are relative to the transparent LAO support. We employ a 0.75 eV pump and a 1.66 eV probe. The probe fluence is 1 $\mu J/cm^2$, the pump is used with 20 $\mu J/cm^2$ or 2 mJ/cm^2 fluence.

Ultrafast intensity pump&probe

The data relative to the ultrafast dynamics of the integrated intensity are shown in Fig. A.1. The temperature dependence is very weak, and the fluence dependence scales linearly. The response consists of a fast overlap signal, and a slow modulation which is compatible with a low frequency coherent E-symmetry vibrational mode [1].

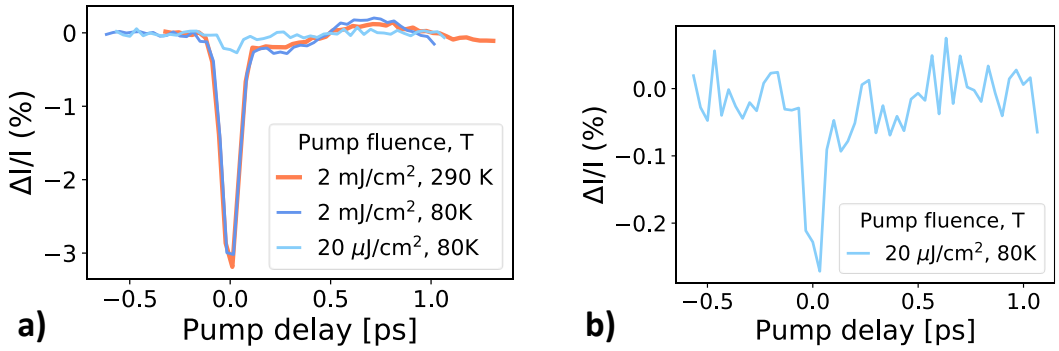

FIGURE A.1: Ultrafast integrated intensity dynamics. a) low-high fluence and temperature comparison. b) Detail of the low pump response.

Ultrafast heterodyne pump&probe

We test the Multimode Heterodyne approach at low temperature (80 K) and at the higher pump fluence in Fig. A.2.
The spectral maps describe an almost spectrally uniform response, which presents the fast optical overlap signal and the slow phonon oscillation. Importantly, the phase dynamics is mainly a positive shift. The anomalous negative behavior observed in YBCO is sample specific.

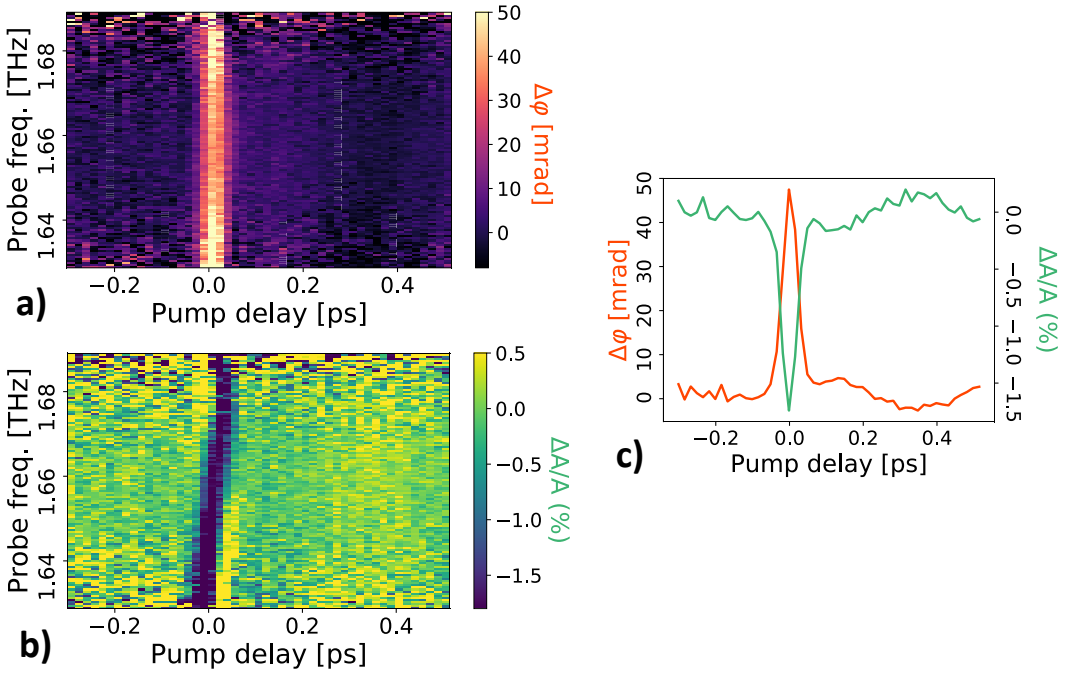

FIGURE A.2: Multimode heterodyne data at 80 K and high pump fluence. a) Spectral phase dynamics. b) Spectral amplitude dynamics. c) Average spectral profiles.

In Fig. A.3 we verify that with the lower pump the trend scales linearly with the pump fluence.

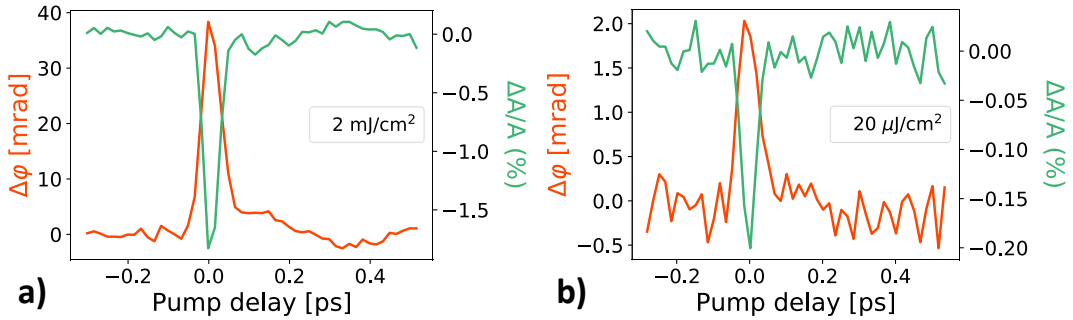

FIGURE A.3: Fluence dependent heterodyne at 80 K. a) High pump. b) Low pump.

References

[1] J. F. Scott. "Raman Study of Trigonal-Cubic Phase Transitions in Rare-Earth Aluminates". *Phys. Rev.* 183 (1969).

List of Figures